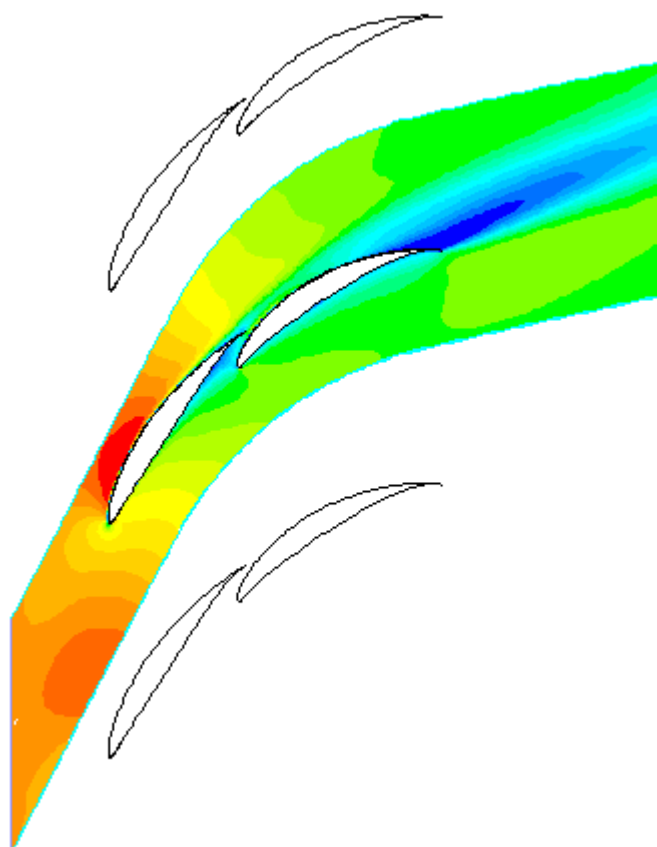


Numerical Investigation of the Flow in Tandem Compressor Cascades

by

Gustavo Cañon Falla



Vienna, 2004

TECHNISCHE UNIVERSITÄT WIEN
Institut für Thermische Energieanlagen

UNIVERSIDAD NACIONAL DE COLOMBIA
Departamento de Ingeniería Mecánica

Diploma thesis for mechanical engineering

**Numerical Investigation of the Flow in
Tandem Compressor Cascades**

written at
Institute of Thermal Powerplants
Vienna University of Technology

by

Gustavo Adolfo Canon Falla
Universidad Nacional de Colombia.
Departamento de Ingeniería Mecánica

under direction of
Ao. Univ. Prof. Dipl.-Ing. Dr. techn. R. WILLINGER
Vienna University of Technology
Institute of Thermal Powerplants

Vienna, July 2004

Abstract

Vienna University of Technology
Institute of Thermal Powerplants

Universidad Nacional de Colombia
Department of Mechanical Engineering

Gustavo Canon Falla

Numerical Investigation of the Flow in Tandem Compressor Cascades

Thesis for the degree of Mechanical Engineering

2004

Thesis Director: Professor Dr. Reinhard Willinger

Thesis Examiner: Engineer. Jorge Arango

72 pages, 61 figures, 13 tables and 3 appendixes

Keywords: tandem blade, axial compressor, cascade, pressure coefficient, loss coefficient, numerical method, gap nozzle effect, flow separation, deflection angle.

The development of practical axial compressors meant for higher loading limits and lowering the engine size and weight has been the goal of the designers. Since about 1970 the interest in tandem blades as a boundary layer control for maximizing the blade loading has emerged.

This thesis presents the numerical investigation of the steady, two-dimensional flow field in a tandem compressor cascade. The interaction mechanism between the two profiles that conform the tandem arrangement has been investigated varying the relative position between the blades. The study is made on the basis of the static pressure distribution along the blades and the total loss coefficient and deflection angle calculated far downstream. The k / ε model was used to account for the turbulent behavior of the flow and a finite volume method was employed to solve the flow governing equations. The computational results are compared with an experimental investigation reported in the open literature and some conclusions about the flow behavior in tandem blade rows are extracted.

Acknowledgements

The work in this thesis could not have been done without the support of my father Gustavo Canon, my mother Martha Falla and my sister Margarita Canon and the understanding and love of Στεφανία Καραμπα. I thank all of them for making it through these times.

I give special thanks to Professor Dr. Reinhard Willinger who took the time to teach me CFD and supervised this thesis.

I would like to express my gratitude to Professor Dr. Hermann Haselbacher for giving me the opportunity to develop this thesis at the Institute of Thermal Powerplants at Vienna University of Technology.

I am grateful to Ing. Gerhard Kanzler, Dipl.Ing. Klaus Hörzer, Dipl. Ing. Dr. Franz Wingelhofer, and Hr. Franz Trummer for their cordiality and support.

Finally to all my friends and especially to Jackub Polkowski, Felipe Rey Ladino and Diva Marcela Garcia.

Contents

Symbols	V
1 Introduction	1
2 Tandem blades: general theory and literature overview	3
2.1 Geometry description	3
2.2 Boundary layer control mechanism	5
2.3 Literature overview	5
2.3.1 Summary of works in tandem blades	6
2.3.2 Experimental investigation of the flow in a 2D tandem compressor cascade	6
2.3.3 Applications of tandem blade rows	9
3 Blade profile and data reduction	11
3.1 Type of blades used	11
3.1.1 NACA 65 profiles	11
3.1.2 NACA 65 cascade data	12
3.2 Data reduction	13
3.2.1 Pressure coefficient	13
3.2.2 Pressure loss coefficient	14
3.2.3 Diffusion factor	14
4 Theoretical bases and concepts	15
4.1 Conservation equations	15
4.2 Modelling turbulent flow	15
4.2.1 Reynolds averaged Navier Stokes equations	15
4.2.2 The two equation standard $k - \epsilon$ turbulence model	17
5 Numerical method	19
5.1 Definition of the control volumes	19
5.2 Integral form of the governing equations	20
5.3 Discretization	21
5.3.1 Discretization the convective terms	22
5.3.2 Discretization the diffusive terms	23
5.3.3 Discretization the source terms	23
5.3.4 Discretization the pressure term	23
5.4 Pressure – Velocity coupling	23
5.5 Linearization of the set of equations	24
5.6 Initial values and boundary conditions	24
5.6.1 Initial conditions	24
5.6.2 Boundary conditions	25
5.7 Normalization	29
5.8 Solution the governing equations	30
5.9 Numerical method summary	31
5.10 Convergence criteria	32
6 Validation: Flow simulation on a NACA65 compressor cascade	33

6.1	Cascade geometry	33
6.2	Inlet flow field and operating conditions	33
6.3	Numerical procedure	34
6.3.1	Numerical method	34
6.3.2	Finite volume mesh	35
6.4	Results and discussion.....	36
6.5	Validation summary	40
7	Tandem blades: influence of the relative position	41
7.1	Inlet conditions	41
7.2	Initial configuration.....	42
7.2.1	Finite volume mesh	42
7.2.2	Front blade results	44
7.2.3	Rear blade results	45
7.2.4	Tandem blade ($a = \infty$): results summary.....	46
7.3	Tandem blade simulations.....	47
7.3.1	Finite volume mesh	48
7.3.2	No gap nozzle effect between the blades	50
7.3.3	Gap nozzle effects	56
8	Conclusions	71
8.1	Profile selection.....	71
8.2	Second blade location: no gap nozzle effect	71
8.3	Second blade location: gap nozzle effect	72
8.4	Numerical model	72
	Appendix 1	73
	Appendix 2	76
	Appendix 3	78
	Bibliography.....	96
	List of Figures	98
	List of Tables.....	100

Symbols

Latin characters:

Symbol	Description
a	Axial displacement; type of mean line in a NACA 6 series blade
A	Area
b	Other terms
c	Chord length
C_p	Pressure coefficient
$C_\mu, C_1, C_2, \sigma_k, \sigma_\varepsilon$	Lauder's closure coefficients
D_{\max}	Separation criterion coefficient (Lieblein coefficient)
E	Empirical constant
f	Instantaneous variable; flow
f'	Fluctuating component
f_c	Convective flow
f_d	Diffusive flow
$F1$	Inlet gap distance
$F2$	Outlet gap distance
k	Turbulent kinetic energy
l_m	Mixing length
M	Mach number
n	Normal direction
p	Static pressure
p_t	Total pressure
P	Cell center; production of turbulent kinetic energy
R	Gas constant
Re	Reynolds number
s	Blade spacing
s_ϕ	Source of ϕ
t	Tangential displacement; time
T	Turbulence intensity; temperature
u, v, w	Velocity components in Cartesian coordinates
u^+	Dimensionless velocity (wall functions)
u_i	Velocity component in tensor form
u'_i	Turbulence velocity fluctuations

u_τ	Wall friction velocity
u^*	Dimensionless velocity (FLUENT)
$u_i u_j$	Reynolds stress tensor
V	Volume
w	Total relative flow velocity
W,E,N,S,T,B	West, east, north, south, top and bottom, respectively
x,y,z	Cartesian coordinate system
y^+	Non dimensional distance (wall functions)
y^*	Non dimensional distance (FLUENT)

Greek characters:

Symbol	Description
α	Absolute flow angle measured from the axial direction (Mellor diagrams); under-Relaxation factor
β	Relative flow angle measured from axial direction
γ	Stagger angle measured from axial direction
Γ_ϕ	Diffusion coefficient for ϕ
δ^{**}	Boundary layer momentum thickness
δ_{ij}	Kronecker tensor
Δ	Variation
ε	Turbulent energy dissipation rate
θ	Component in θ direction
κ	Von Karman constant; isentropic exponent
μ	Molecular viscosity
μ_t	Turbulent or eddy viscosity
ν	Kinematic viscosity
ρ	Fluid density
σ	Solidity (chord/spacing ratio)
$(\tau_{ij})_{comb}$	Combined viscous and turbulent stress tensor
$(\tau_{ij})_{lam}$	Viscous stress tensor
$(\tau_{ij})_{turb}$	Reynolds stress tensor
ϕ	Global variable
ω	Pressure loss coefficient
ϖ	Mass weighted loss coefficient

Subscript indices:

Symbol	Description
1	Related to the front profile; related to the inlet of a tandem blade; related to the inlet of a single blade (Mellor diagrams)

12	Related to the inlet of the second profile in a tandem blade
2	Related to the rear profile; related to the outlet of a tandem blade; related to the outlet of a single blade (Mellor diagrams)
d	Design value
inlet	Referring to the inlet plane
i, j, k	Indices; coordinate in tensor form
l	Index representative to the faces of the control volume
lam	Referring to laminar
local	Local value
max	Maximum value
min	Minimum value
new	New value
old	Old value
ref	Value of reference
t	Related to the overall tandem blade
turb	Referring to turbulent
w	Referring to the wall
x,y	Component in x and y directions, respectively
∞	Far downstream value

Superscript indices:

Symbol	Description
—	Time average value
*	Non dimensional representation

Abbreviations:

Symbol	Description
CDA	Controlled diffusion airfoil
CV	Control volume
DF	Diffusion factor
LE	Leading edge
NACA	National Advisory Committee of Aeronautics
NB	Neighbour cells
PS	Pressure surface
SS	Suction surface
TE	Trailing edge

1 Introduction

Multistage axial compressors are used in heavy-duty as well as in aero engine gas turbines. Modern gas turbines require to achieve improved efficiency and this can be accomplished by higher turbine inlet temperature accompanied by high total pressure ratio of the compressor.

The development of axial compressors capable to delivering high compression ratios without increasing the number of stages and without sacrificing the efficiency of the components leads to high loading blade rows.

Since the load per stage is restricted by some aerodynamic constraint, common airfoils used in compressors as NACA 65 series and even Controlled Diffusion Airfoils show their limitation due to the presence of flow separation when high turning angle is required.

One way to overcome this problem is to use an improved blade configuration so called tandem compressor cascades. With this arrangement, the whole blade is split into two subsequent blade rows and various interaction mechanisms between those blades prevent the separation tendency.

With advancement of turbulence modelling the interaction mechanisms between the two adjacent blade rows that conform a tandem compressor cascade are examined. The main area of focus is the internal flow around the blades in regards of flow turning angle and total losses.

The thesis involves the numerical computation of the steady, two-dimensional flow field in a tandem compressor cascade using the solver FLUENT 6.1. The geometry of the two profiles that conform the tandem blade is chosen from the open literature, which is supported by experimental results. Since the cascade geometry is rather complex the mesh for each configuration is generated using a parametric algorithm developed in GAMBIT.

A brief overview of the next chapters is given as follows:

Chapter 2 describes the main characteristics of tandem blades and summarises various investigations reported in the technical literature.

Chapter 3 states the criterion used for the blade selection and gives the main concepts for the data reduction.

Chapter 4 covers the aspects of the physical model used to define an incompressible turbulent fluid in two-dimensions.

Chapter 5 shows how the physical model in chap. 4 is transformed to be solved numerically using a finite volume method.

In order to gain confidence in the numeric results, an analysis of the flow along a NACA651510 blade row is performed in chap. 6, and the finite volume model is compared with experimental and numerical data.

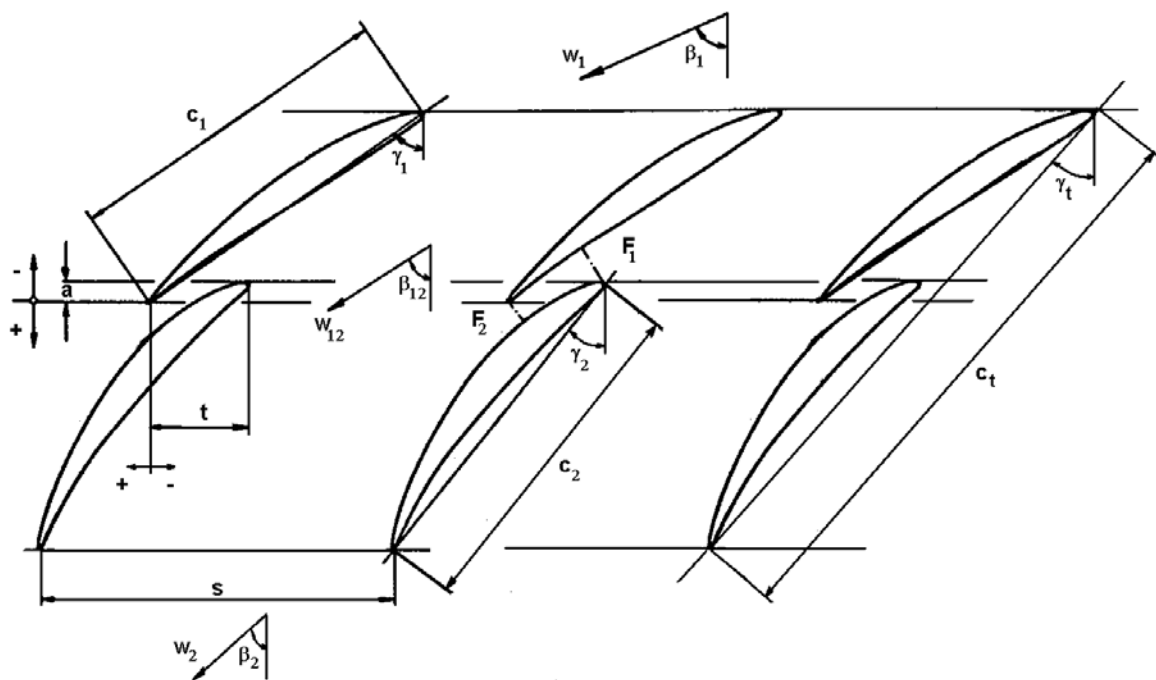
Chapter 7 shows the set of results obtained from the simulations of a tandem compressor cascade for various second blade locations.

The work concludes with a summary of conclusions.

2 Tandem blades: general theory and literature overview

2.1 Geometry description

The geometry and aerodynamic parameters for a tandem blade row are almost the same as those used for single airfoils, but two additional variables appear in the arrangement. These variables are the axial displacement and the tangential displacement. Figure 2-1 shows the geometry and standard nomenclature related to tandem airfoils in cascade.



a	Axial displacement	w_{12}	Inlet velocity at rear blade
F_1	Inlet gap distance	w_2	Outlet velocity
F_2	Outlet gap distance	β_1	Inlet flow angle
c_1	Chord length front blade	β_{12}	Inlet flow angle at rear blade
c_2	Chord length rear blade	β_2	Outlet flow angle
c_t	Overall chord length	γ_1	Stagger angle front blade
s	Blade spacing	γ_2	Stagger angle rear blade
t	Tangential displacement	γ_t	Overall stagger angle
w_1	Inlet velocity		

Figure 2-1: Tandem cascade nomenclature

The above figure indicates that the nomenclature of a tandem airfoil can be treated in two different ways:

- Single blade specification: The single blade parameters corresponding to the front and rear profiles of a tandem blade and a notation of the relative position between the blades (axial and tangential displacement) are used to characterize the tandem cascades when the focus of the study is the interaction between both profiles (this approach is followed along the thesis).
- Overall parameters: The overall tandem parameters, derived from the single blades quantities, represent the tandem blade as an equivalent single one. Therefore, they are used to compare a single cascade with a correspondent tandem blade row.

According to the axial and tangential displacements the interference area between the blades plays the role of a nozzle. The gap-nozzle is typically shaped to accelerate and guide the flow from the pressure surface of the front tandem onto the suction surface of the back tandem. The nozzle is characterized in this work by the inlet gap distance (F1) and the outlet gap distance (F2). Figure 2-2 illustrates the gap nozzle in a tandem cascade.

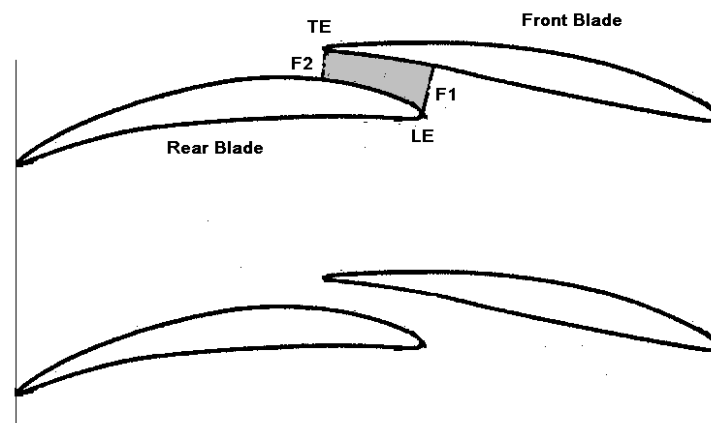


Figure 2-2: Gap-nozzle area in a tandem blade

When the nozzle area is not presented in the arrangement, the interaction between the blades is only evident when the second profile is positioned in the wake of the first blade. Figure 2-3 illustrates a tandem blade row with the rear blade positioned far downstream of the front profile. Some authors treat this kind of configurations as two isolated blades (specially for large positive axial displacements).

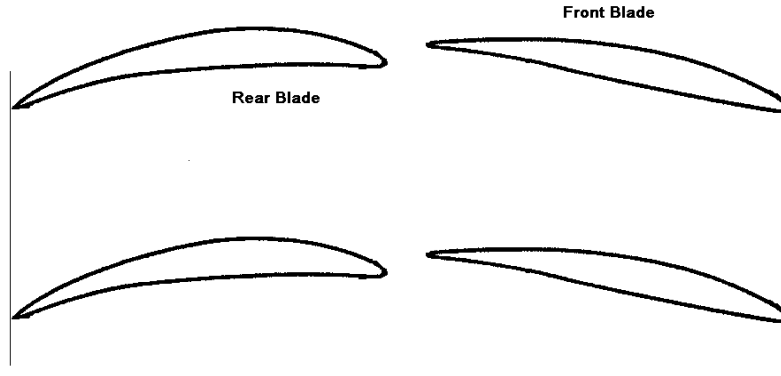


Figure 2-3: Tandem Blade. No gap nozzle area between the profiles

2.2 Boundary layer control mechanism

The boundary layer control mechanism of a tandem blade must be given due consideration whereby flow separation can be avoided. To explain this characteristic the diffusion factor separation criterion for turbulent boundary layers defined by Lieblein [12] is used.

$$\frac{\delta^{**}}{w} \cdot \frac{dw}{dx} \leq D_{\max}$$

Eq. 2-1

where δ^{**} is the boundary layer momentum thickness, w is the free stream velocity outside the boundary layer, $\frac{dw}{dx}$ is the variation of velocity over the surfaces of a typical compressor blade and D_{\max} is a maximum value that states the safe zone in which stall is not presented.

In a single profile, under highly loaded requirements, the rise in pressure could be sufficiently great that the growth of the momentum thickness in Eq. 2-1 generates a separation zone near the trailing edge of the blade. Whereas in a tandem blade row, the momentum thickness is refreshed by the formation of a new boundary layer at the aft airfoil of the downstream cascade while it is expected that the flow and boundary layer of the forward airfoil do not disturb the rear blade. Thus, the flow through a tandem blade avoids early flow separation resulting in larger values of flow deflections when compared with single airfoils.

2.3 Literature overview

In the technical literature, many attempts have been done to understand the flow in a tandem cascade. Experimental, as well as analytical approaches are reported for many flow conditions and different blade parameters.

The literature overview section gives insight into the major works in the field of tandem compressor cascades. It will start with a short review of the different works followed by one section that details an investigation in tandem cascades and its major conclusions. The final section is a summary of some applications of tandem blade rows.

2.3.1 Summary of works in tandem blades

One of the largest investigations was conducted to determine the potential of tandem-airfoil blading for improving the efficiency and stable operating range of compressor stages. The investigation included testing of one single-airfoil blading, one tandem-blade with a 20-80% loading split and one tandem-blade with 50-50% loading split (the loading was estimated using the diffusion factor criterion). The results of this effort was summarized by Wennerstrom [26] and state that the original hypotheses that tandem configuration with the majority of loading on the rear airfoil should have a larger operation range than conventional blades was not substantiated, but with 50 / 50 percent loading split between the airfoils the tandem arrangement demonstrated higher pressure rise and efficiency than the corresponding single one.

The technical papers that studied the optimal blade location in a tandem cascade [2] [16] [24] concluded that the axial and tangential displacement have to be set experimentally because they depend highly on the flow parameters and the geometry of the profiles. Therefore, there is no an established rule to assure an optimum blade performance for a tandem arrangement. The authors coincide in the fact that when the second blade is positioned in such a way that a gap nozzle area is formed in the interference zone between the two profiles, there is an advantage in terms of total losses.

Various investigations in tandem airfoils [17] [18] [19] [24] indicated that the flow deflection capabilities shown by the tandem configuration at design point, is higher compared with a single one. This fact has been explained by the formation of a new boundary layer at the rear blade.

Saha and Roy [17][18] conducted various aerodynamic performance evaluations of a single and a tandem cascade for a wide range of inlet angles. The purpose of the investigation was to determine the high deflection capabilities of the tandem blade and to compare the results at off design with an equivalent single one. The tandem blades were conformed by two scaled down CDA profiles with a gap nozzle geometry fixed in previous works. The results of the study showed that the diffusion capabilities of the tandem blade are higher compared to a single airfoil over a limited angles of attack. Therefore, it was concluded that the tandem blades has a narrow operational range due to the fact that both profiles are scaled down and they have low leading edge radius. Hence, the front and rear blades are limited to narrow incidences.

2.3.2 Experimental investigation of the flow in a 2D tandem compressor cascade

Bammert and Staude [2] conducted a representative investigation that summarizes the influence of the relative position between the two profiles that conform a tandem blade and the total losses of the whole arrangement. In this effort, three tandem-blade-rows were tested (Table 2-1).

Tandem cascade	Equivalent location on a multistage axial compressor blade
A	Hub
B	Middle
C	Tip

Table 2-1: Location of the three tandem cascades tested by Bammert and Staude [2]

The blades conforming the tandem configuration were NACA 65 airfoils and their characteristics are shown in Table 2-2.

Tandem cascade	Solidity (σ)	β_1 [°]	$\Delta\beta$ [°]
A	1.02	65.5	46.5
B	0.88	65.5	27.7
C	0.79	65.5	19.6

Table 2-2: Characteristics of the three tandem cascades tested by Bammert and Staude [2]

Bammert and Staude concluded that the pressure distribution along the suction surface of the front profile as well as the pressure distribution along the pressure surface of the rear blade is independent of the relative position between the blades. This fact was evidenced because there was no major difference between the results obtained in those surfaces for all the tandem blades tested (Figure 2-4).

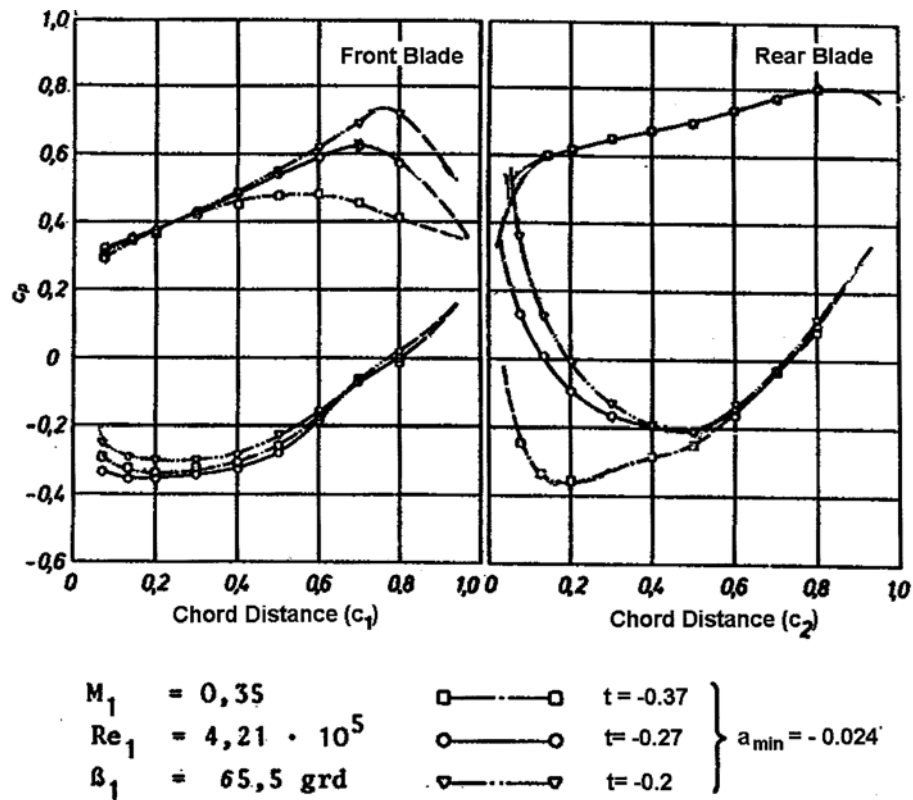


Figure 2-4: Pressure coefficient. Tandem cascade B tested by Bammert and Staude [2]

For each cascade, different blade locations were tested (varying the relative position between the profiles) and the results showed that the optimum configuration was obtained with the blades overlapping (a_{\min}). This characteristic is illustrated in Figure 2-5.

At the optimum location, it is important to remark that no high difference between the turning angle was noticeable when comparing the results obtained in a tandem cascade with the results of both blades acting independently ($a = \infty$), but a high decrease in total losses occurs ($\frac{\varpi}{\varpi_{\infty}} \approx 0,78 - 0,84$) (Figure 2-6). With these values it results interesting the fact that the losses

decrease almost 20% when the second profile is positioned at the optimum displacement in the tandem blade.

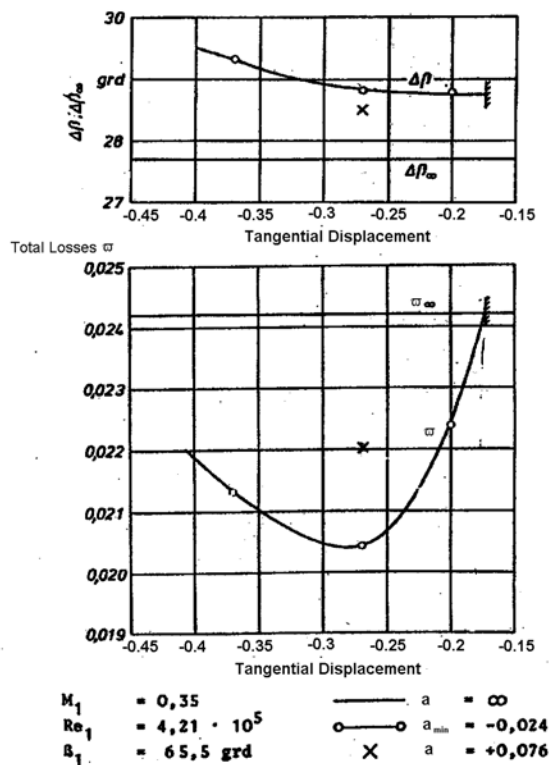


Figure 2-5: Turning angle and total losses of the tandem cascade B [2]

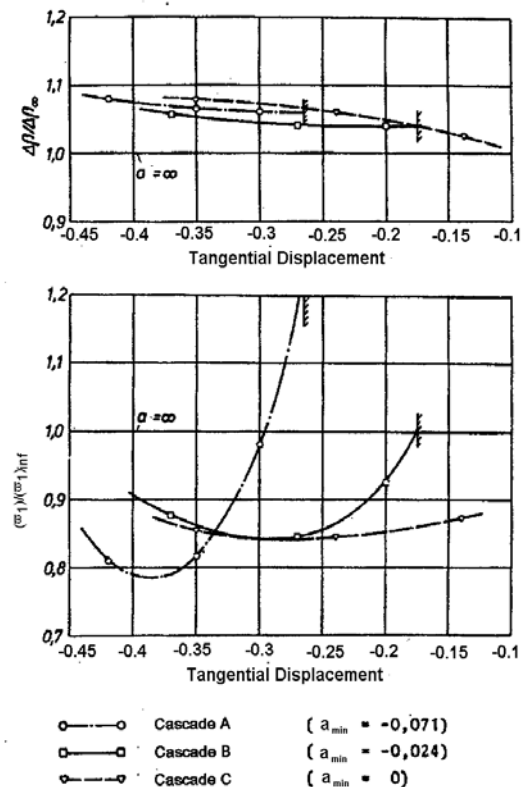


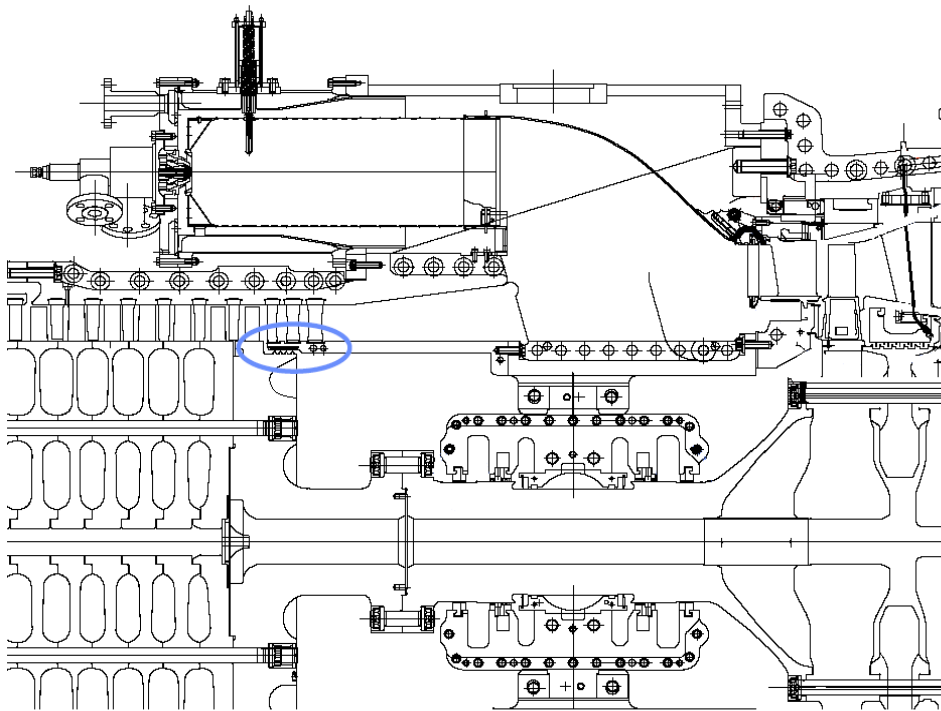
Figure 2-6: Turning angle and total losses relative to an equivalent single blade [2]

Three major conclusions referring the relative blade positions were extracted from Bammert's investigation:

- The optimum location of the blades is defined as the relative position that minimises the total losses of the arrangement. This optimum position depends on the aerodynamic and flow parameters and it is usually set experimentally.
- The ratio $F1/F2$ should be lower than 2 in order to avoid a blockage effect that will cause an increment in the losses.
- If the ratio $F1/F2$ is lower than 1 the interference zone acts as a diffuser causing an increment in the losses of the second profile.

2.3.3 Applications of tandem blade rows

In the practice, the tandem cascades are applied to compressors in the subsonic, transonic and even supersonic range for rotors and stators [24] but the main use of this arrangement is in the stator of the final stage in axial compressor where the flow enters with high swirl velocity and it has to be turned to the axial direction. Therefore, the flow-turning angle is rather high and the last stator row is heavily loaded with the danger of flow separation. Figure 2-7 shows a General Electric heavy-duty gas turbine that uses a triple tandem blade row in the stator of the last stage in the axial compressor. A similar use of tandem cascades is as an exit guide vane for the axial part of a mixed flow compressor where high deflection of the flow is also required.



Manufacturer	General Electric
Type	MS 7001 EA
Power	86,2 MW
Thermal efficiency (η_{th})	33,0 %
Pressure ratio (π)	11,9 [-]
Mass flow	299 [kg/s]
Turbine inlet temperature	Not Reported
Turbine outlet temperature	537 °C
Revolutions	3600 u/min

Figure 2-7: Heavy-duty gas turbine with tandem compressor blades in the last stator row

Recently, research [16] has been undertaken to find the operational feasibility of developing tandem cascade for the off-design condition. At off-design operation the inlet flow angle differs from its value at design point as well as the axial velocity [16]. The losses of the compressor increase and consequently the efficiency decrease. Therefore, to overcome this limitation and maintain the performance of the machine at off-design regimens, flexibility in

the operation of the component is required. One way to improve this situation is to operate the cascade in a variable camber mode using tandem blade rows where both blades can be adjusted independently from each other. By this means the blade can be adapted to the velocity triangles at off-design leading to less sacrifice of the cycle efficiency.

Tandem blades in centrifugal compressors are rarely used because of increasing manufacturing costs, and concern of potential large losses in aerodynamic performance. The main benefit that presents a tandem blade for this application is to reduce the highly distorted wake exit velocity profile typically encountered in single impeller designs [15]. A 3D representation of a tandem impeller design is showed in Figure 2-8.

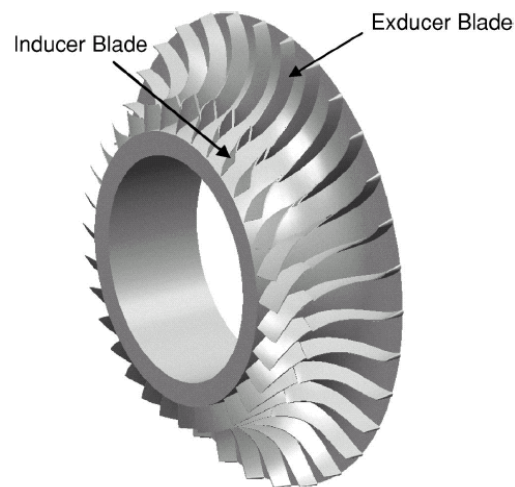


Figure 2-8: Three-dimensional representation of tandem-impeller [15]

3 Blade profile and data reduction

3.1 Type of blades used

Tandem blade rows are mainly used in the last stator blade row of multistage compressors where the flow is generally in the subsonic range. Since the type of blades used in compressors depends primarily on the Mach number range, for this application standardized series as NACA 65 are common¹.

3.1.1 NACA 65 profiles

NACA 65 series was designed for use as a low drag aircraft wing with the objective of obtaining desirable drag, critical Mach number, and maximum lift characteristics with a combination of camber and thickness distribution chosen to give a constant loading (i.e. pressure difference) between suction and pressure surface. Although the shape was originally designed for aircraft wings, it has been extensively used in cascade applications where the original pressure distribution would be lost.

The nomenclature for the shape and camber of the 65-series consists of a six-digit number and an annotation showing the mean line. As an example, in the airfoil *NACA 65,3-1510 a=0.5*, the meaning of each number is the following:

- The first digit “ 6 “ is the series designation.
- The second digit “ 5 “ means the position of minimum pressure in tenths of the chord behind the leading edge for the basic section at zero lift.
- The next digit “ 3 “ gives the range of lift coefficient in tenths above and below the design lift coefficient in which favourable pressure gradient exists on both surfaces.
- The two following digits “ 15 “ mean the design lift coefficient in tenths.
- The last two digits “ 10 “ denote the thickness of the wing section in percent of the chord.
- The annotation $a = 0.5$ shows the type of mean line. If this notation is omitted, it is understood that the uniform mean line ($a=1.0$) has been used.

Unlike other airfoils developed by the National Advisory Committee for Aeronautics (NACA 2 to 5 series), the thickness distribution of the NACA 6 series airfoils are not defined by algebraic equations, but use complex variable mapping of a circle into an airfoil shape. Therefore, it is common to use the geometry values reported in the technical literature for each specific blade and not to generate the blade using the conformal transformation. In this work the data for thickness distribution and mean line available in [1] was used.

¹ Cumpsty recommended the use of NACA – 65 blades up to inlet Mach number of 0.78 [4]

The final cambered blade is obtained by combining the thickness distribution and the mean line to give the required pressure distribution using the procedure described in Appendix 1.

3.1.2 NACA 65 cascade data

The largest investigation in NACA 65 series was developed by Emery et al. [7] and a large database for different NACA 65 series profiles has been build up with the results. The information of this investigation is presented in the NACA 1368 report in a rather inconvenient manner with tests performed at constant inlet angles for a range of blade staggers. Mellor replotted this data in a better way, using graphs of outlet flow angle (α_2) versus inlet flow angle (α_1) for blade sections of given camber and solidity, set at various staggers. In Mellor's diagrams stall is set at the condition at which the total loss is 1.5 times the minimum loss. Figure 3-1 illustrates a Mellor diagram for a NACA651210 cascade with $\sigma = 1$.

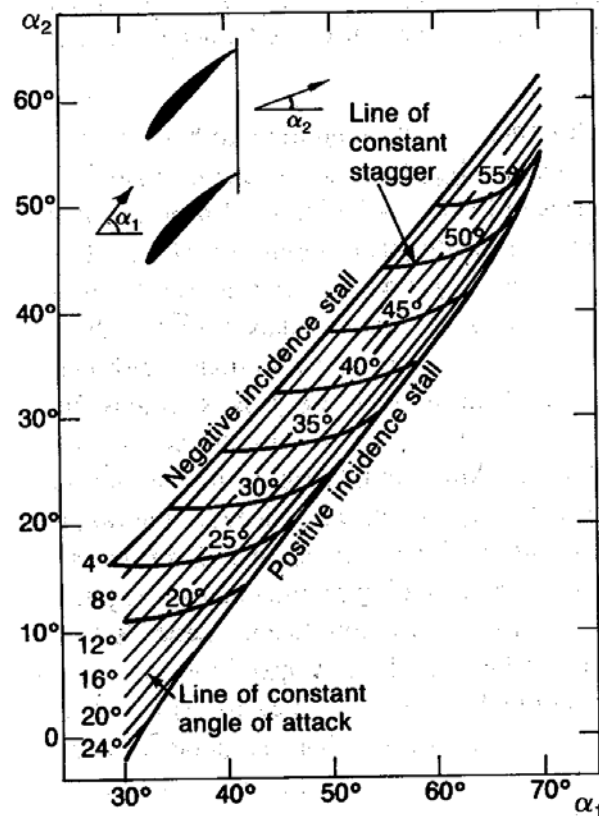


Figure 3-1: Mellor diagram: NACA 651210 cascade with $\sigma = 1.0$ [4]

The design points for each cascade tested in the NACA 1368 report are chosen on the basis of the smoothest pressure distribution observed on the blade surfaces [8]. These design points are obtained in this thesis using Figure 3-2.

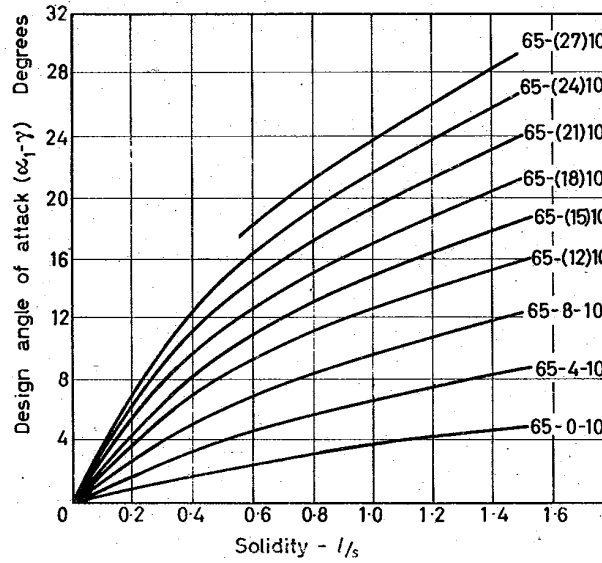


Figure 3-2: Design angles of attack for NACA 65 series [8]

In order to validate the turbulent and numerical model proposed in the two following chapters, the data available in Trenker's diploma thesis [22] is used. Trenker made a comparison between the numerical simulation of the flow on a NACA651510 cascade and the experimental data reported by Emery et al. [7] for the same blade.

In the present work, the blade parameters used to conform the different tandem arrangements was chosen from the cascade databases just mentioned.

3.2 Data reduction

The data reduction is done using local values calculated at different points along the blade spacing as well as overall values using a mass weighted average procedure (blade-to-blade average) defined for a global variable ϕ as follows

$$\bar{\phi} = \frac{\int_{ss}^{ps} (\phi \cdot \rho \cdot w_x) dy}{\int_{ss}^{ps} (\rho \cdot w_x) dy}$$

Eq. 3-1

3.2.1 Pressure coefficient

Since the distribution of pressure along the blade surface indicates the influence of the inlet flow angle on the blade loading, the knowledge of pressure distribution on the blade surface becomes necessary. The rise in static pressure is non-dimensionalized in this thesis by the inlet dynamic pressure of the blade row,

$$C_{p1} = \frac{p_{local} - p_1}{\frac{1}{2} \rho w_1^2}$$

Eq. 3-2

3.2.2 Pressure loss coefficient

The source of losses in turbomachinery can be divided in profile losses, shock losses, clearance losses, secondary losses, endwall losses and cavitation losses [11]. Due to the characteristics of this work only the two-dimensional losses will be studied. These losses can be classified as (1) profile losses, which are mainly associated with blade boundary layers in terms of flow separation and (2) wake mixing losses.

The two dimensional profile losses depend on the flow parameters (Reynolds number, Mach number, inlet turbulence) and blade parameters such as thickness, camber, solidity, stagger angle and blade roughness. The mixing losses arise due to mixing of the wake with the free stream, and this depends on, in addition to the parameter listed above, the distance downstream.

The profile and mixing loss evaluation takes into consideration the boundary layer growth, as well as the static pressure variation along the flow path and it is expressed in this work in form of a loss coefficient defined as follows

$$\omega_1 = \frac{p_{t1} - p_{t2}}{\frac{1}{2} \cdot \rho \cdot w_1^2}$$

Eq. 3-3

Based on Eq. 3-1 and Eq. 3-3 the mass average total pressure coefficient [11] is given by

$$\omega_1 = \frac{\int_{ss}^{ps} (p_{t1} \cdot \rho_1 \cdot w_{x1} - p_{t2} \cdot \rho_2 \cdot w_{x2}) dy}{\int_{ss}^{ps} (\rho_1 w_{x1}) (\frac{1}{2} \rho_1 w_1^2) dy}$$

Eq. 3-4

3.2.3 Diffusion factor

The diffusion factor (DF) is a measure of loading and gives an estimate of combined flow turning and diffusion capability of a cascade. This parameter was derived by Lieblein [12] for single airfoils in a cascade, and essentially it relates empirically the peak velocity on the suction surface of the blade to the velocity at the trailing edge,

$$DF = \frac{w_{\max} - w_2}{w_1}$$

Eq. 3-5

Because the magnitude of peak velocity involves knowledge of the flow field, it is better to use a parameter that does not require this variable. Through a series of simplify assumptions, Eq. 3-5 can be rewritten using one component of the deceleration of the flow and a second of the turning of the flow. Therefore, for a simple two-dimensional geometry, diffusion factor reduces to

$$DF = 1 - \frac{w_2}{w_1} + \frac{\Delta w}{2\sigma w_1} \quad \text{with} \quad \Delta w = w_{\theta 1} - w_{\theta 2}$$

Eq. 3-6

Lieblein sets the stall when the loss is twice the minimum with a value of $DF = 0.6$ [13].

4 Theoretical bases and concepts

In this chapter are treated the most significant theoretical bases which are of importance for the computing procedure.

4.1 Conservation equations

The starting point for the computation of a steady, incompressible and viscous flow are the conservation equations for continuity and linear momentum relating the laws of mechanics to the fluid:

$$\frac{\partial u_i}{\partial x_i} = 0$$

Eq. 4-1

$$\rho \left(u_j \frac{\partial u_i}{\partial x_j} \right) = -\frac{\partial p}{\partial x_i} + \frac{\partial}{\partial x_j} \left[\mu \left(\frac{\partial u_i}{\partial x_j} + \frac{\partial u_j}{\partial x_i} \right) \right]$$

Eq. 4-2

where the last term of Eq. 4-2 is the viscous stress tensor $(\tau_{ij})_{lam}$

$$(\tau_{ij})_{lam} = \mu \left(\frac{\partial u_i}{\partial x_j} + \frac{\partial u_j}{\partial x_i} \right)$$

Eq. 4-3

The impulse equation (Eq. 4-2) is called Navier Stokes equation. In some literature and also in this thesis the expression “Navier Stokes equations” refers however to the set of equations describing the flow consisting of the impulse equation and the continuity equation (Eq. 4-1).

4.2 Modelling turbulent flow

4.2.1 Reynolds averaged Navier Stokes equations

In order to solve a turbulent flow problem using the Navier Stokes equations, it requires direct numerical simulation of the entire turbulent spectrum. Since turbulence consists of random fluctuations of the various flow properties, a statistical approach is used, in which all the variables are cast into a mean value and a random fluctuating quantity as follows:

$$f(x, y, z, t) = \overline{f}(x, y, z) + f'(x, y, z, t)$$

Eq. 4-4

where $f(x, y, z, t)$, is the instantaneous variable, $f'(x, y, z, t)$ is the fluctuating component, and the overbar indicates time-averaged values, defined as

$$\bar{f}(x, y, z) = \frac{1}{\Delta t} \int_t^{t+\Delta t} f(x, y, z, t) dt$$

Eq. 4-5

The operator $f(x, y, z, t)$ is then used to replace all the dependent variables in the Navier Stokes equations and a time averaging² of the entire equation is performed [Appendix 2].

From the above procedure, the averaged continuity equation is

$$\frac{\partial \bar{u}_i'}{\partial x_i} = 0 \quad ; \quad \frac{\partial \bar{u}_i}{\partial x_i} = 0$$

Eq. 4-6

and the averaged momentum equation is

$$\bar{\rho} \bar{u}_j \frac{\partial \bar{u}_i}{\partial x_j} = -\frac{\partial \bar{p}}{\partial x_i} + \frac{\partial}{\partial x_j} \left[\mu \left(\frac{\partial \bar{u}_i}{\partial x_j} + \frac{\partial \bar{u}_j}{\partial x_i} \right) - \overline{\rho u_i' u_j'} \right]$$

Eq. 4-7

where $\overline{\rho u_i' u_j'}$ is a result of the time averaging process and is called the Reynolds-Stress tensor $(\tau_{ij})_{turb}$.

$$(\tau_{ij})_{turb} = -\overline{\rho u_i' u_j'} = -\rho \begin{bmatrix} \overline{u'u'} & \overline{u'v'} & \overline{u'w'} \\ \overline{u'v'} & \overline{v'v'} & \overline{v'w'} \\ \overline{u'w'} & \overline{v'w'} & \overline{w'w'} \end{bmatrix}$$

Eq. 4-8

The Reynolds stress tensor is a symmetric tensor ($\tau_{ij} = \tau_{ji}$), and thus has six independent components. Therefore, to solve Eq. 4-7 it is necessary to find enough equations to close the system.

The closure model that is used in the present work is the Boussinesq assumption, which states that the turbulent shearing stresses might be related by a mean strain through a scalar turbulent eddy viscosity. The physical idea behind the concept of “eddy” viscosity (μ_t), is the conceptual similarity between the turbulent fluctuations and the random molecular motion in laminar flows even the resemblance between these two motions is somewhat superficial. Nevertheless, it is assumed that the transfer of momentum by molecular motion is similar to that induced by turbulent fluctuations. It should be emphasized that molecular viscosity is a property of fluid and that turbulence is a property of flow. Therefore, the eddy viscosity is a function of the flow properties [28].

² Time averaging is appropriate for stationary turbulence, which means that the turbulence flow on average does not vary with time, which is acceptable for the flow encountered in this thesis.

The turbulent eddy viscosity will be quantified in this thesis using the two equation standard $k - \varepsilon$ turbulence model.

4.2.2 The two equation standard $k - \varepsilon$ turbulence model

Two equation models of turbulence have been the foundation for much of the turbulence model research during the last decades and have been very successful in computing two-dimensional flows. The most widely used model in this category is the Standard Jones-Lauder $k - \varepsilon$ model (1972, 1973) which is a semi-empirical model that assumes that the flow is fully turbulent, and the effects of molecular viscosity are negligible. Therefore, it is valid only for fully turbulent flows.

The standard $k - \varepsilon$ model is based on the Bussinesq assumption, that means that the components of the turbulent stress tensor are proportional to an averaged deformation tensor. Thus, the Reynolds tensor is expressed as follows

$$(\tau_{ij})_{turb} = \mu_t \left[\frac{\partial \bar{u}_i}{\partial x_j} + \frac{\partial \bar{u}_j}{\partial x_i} \right] - \frac{2}{3} \rho k \delta_{ij}$$

Eq. 4-9

where the operator δ_{ij} is equal to 1 when $i = j$ and equal to 0 when $i \neq j$.

Eq. 4-7 can be written using the viscous (Eq. 4-3) and turbulent (Eq. 4-9) tensor notations in the following way

$$\rho \bar{u}_j \frac{\partial \bar{u}_i}{\partial x_j} = - \frac{\partial \bar{p}}{\partial x_i} + \frac{\partial}{\partial x_j} \left[(\tau_{ij})_{lam} + (\tau_{ij})_{turb} \right]$$

Eq. 4-10

In Eq. 4-10 the term in brackets represent the combined viscous and turbulent stress tensor

$$\begin{aligned} (\tau_{ij})_{comb} &= (\tau_{ij})_{lam} + (\tau_{ij})_{turb} = \mu \left(\frac{\partial \bar{u}_i}{\partial x_j} + \frac{\partial \bar{u}_j}{\partial x_i} \right) + \mu_t \left[\frac{\partial \bar{u}_i}{\partial x_j} + \frac{\partial \bar{u}_j}{\partial x_i} \right] - \frac{2}{3} \rho k \delta_{ij} \\ &= (\mu + \mu_t) \left(\frac{\partial \bar{u}_i}{\partial x_j} + \frac{\partial \bar{u}_j}{\partial x_i} \right) - \frac{2}{3} \rho k \delta_{ij} = \mu_e \left(\frac{\partial \bar{u}_i}{\partial x_j} + \frac{\partial \bar{u}_j}{\partial x_i} \right) - \frac{2}{3} \rho k \delta_{ij} \end{aligned}$$

Eq. 4-11

where μ_e is the effective viscosity

As said before, the $k - \varepsilon$ model is used to calculate the turbulence eddy viscosity (μ_t) which is defined through the turbulent kinetic energy k and the turbulent dissipation rate ε .

$$\mu_t = \rho \nu_t \quad ; \quad \nu_t = C_\mu \frac{k^2}{\varepsilon}$$

Eq. 4-12

with

$$k = \frac{1}{2} \overline{u_i' u_i'} \quad ; \quad \varepsilon = \nu \overline{\frac{\partial u_i'}{\partial x_j} \frac{\partial u_i'}{\partial x_j}}$$

Eq. 4-13

In this model the partial differential equation for the specific turbulent kinetic energy k is given as follows

$$\rho \bar{u}_j \frac{\partial k}{\partial x_j} = \frac{\partial}{\partial x_j} \left[\frac{\mu_t}{\sigma_k} \left(\frac{\partial k}{\partial x_j} \right) \right] + P - \rho \varepsilon$$

Eq. 4-14

The term of the left-hand side in Eq. 4-14 is the convective transport of k ; the first term (in brackets) on the right –hand side represents diffusion of turbulence. The second term on the right side is the production of k by mean flow velocity gradients and is defined as

$$P = \mu_t \left(\frac{\partial \bar{u}_i}{\partial x_j} + \frac{\partial \bar{u}_j}{\partial x_i} \right) \frac{\partial \bar{u}_i}{\partial x_j}$$

Eq. 4-15

In order to provide a proper closure equation, the dissipation term is modelled by the following equation

$$\rho \bar{u}_j \frac{\partial \varepsilon}{\partial x_j} = \frac{\partial}{\partial x_j} \left[\frac{\mu_t}{\sigma_\varepsilon} \left(\frac{\partial \varepsilon}{\partial x_j} \right) \right] + \frac{\varepsilon}{k} (C_1 P - C_2 \rho \varepsilon)$$

Eq. 4-16

The three terms on the right-hand side of Eq. 4-16 are, respectively, diffusive transport, viscous production and destruction.

The closure coefficients used by Launder's group are presented in Table 4-1.

$C_\mu [-]$	$\sigma_k [-]$	$\sigma_\varepsilon [-]$	$C_1 [-]$	$C_2 [-]$
0.09	1.00	1.30	1.44	1.92

Table 4-1: Closure coefficients of the standard k - ε model

These values have been determined from experiments with air and water for fundamental turbulent shear flows. They have been found to work fairly well for a wide range of wall-bounded and free shear flows [5].

5 Numerical method

To convert the governing equations to algebraic equations that can be solved numerically it is used a control volume based technique that consist of:

- Division of the domain into discrete control volumes using a computational grid.
- Integration of the governing equations on the individual control volumes to construct algebraic equations for the discrete dependent variables.
- Linearization of the discretized equations and solution of the resultant linear equation system to yield updated values of the dependent variables.

One of the reasons for using the finite volume method to solve the governing fluid equations is that for a complicated geometry (as the geometry studied) the physical domain is divided into small volumes and the mass, momentum and turbulence equations are conserved when solved in integral form.

The solver FLUENT 6.1 is used to perform the numerical computation for all the models in this thesis.

5.1 Definition of the control volumes

As said before, the whole domain is divided into a finite number of cell-centered control volumes; that means that the main variables of the model are defined in the center of the control volume instead of the nodes.

This cell-centered arrangement is designated in the so called compass notation, where the CV center is named P, the adjacent cell centers are designated in capital letters referring the direction of the cell respect to the Control Volume (W (west), E (east), N (North), S (South), T (Top), B (bottom)) and the cell edges are designated with lowercase letter referring also the relative position respect the center (P) as seen in Figure 5-1.

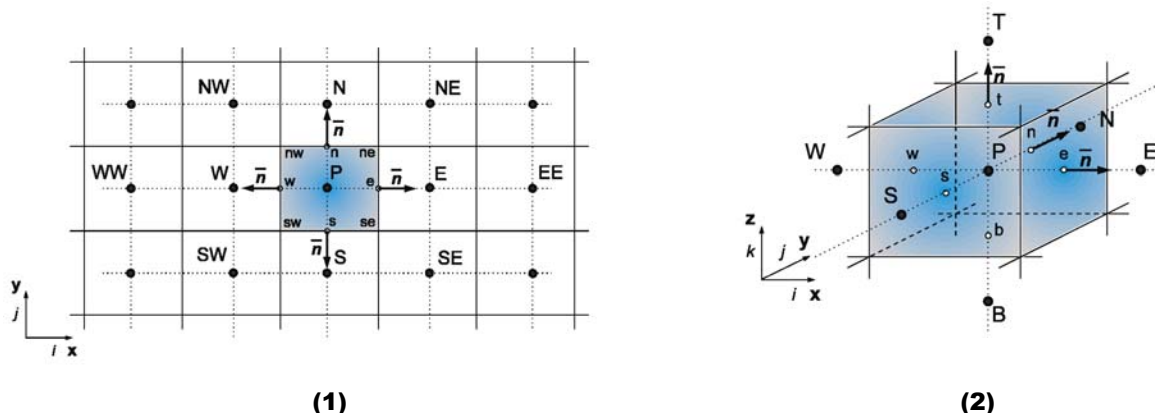


Figure 5-1. Control volume. (1) Two-dimensional grid. (2) Three-dimensional Grid

5.2 Integral form of the governing equations

The steady state Navier Stokes equations and the turbulent transport equations that govern the behaviour of the flow have a convective and a diffusive term as well as a source term. Due to its similar structure, the conservation equation for transport of a general variable ϕ can be expressed as

$$\underbrace{\frac{\partial(\rho u_j \phi)}{\partial x_j}}_{\text{convective Term}} = \underbrace{\frac{\partial}{\partial x_j} \left(\Gamma_\phi \frac{\partial \phi}{\partial x_j} \right)}_{\text{diffusive Term}} + \underbrace{s_\phi}_{\text{Source Term}}$$

Eq. 5-1

Where

$$\begin{aligned} \Gamma_\phi &= \text{Diffusion coefficient for } \phi \\ s_\phi &= \text{Source of } \phi \text{ per unit volume} \end{aligned}$$

Using the Finite Volume calculation, the Eq. 5-1 has to be integrated over each partial volume described in chap. 5.1. To perform this, the volume integrals corresponding to the convective and the diffusive terms are transformed into surface integrals using the integral theorem of Gauss.

Integral theorem of Gauss:

$$\int_V \frac{\partial u_i}{\partial x_i} dV = \int_A u_i \cdot n_i dA$$

Eq. 5-2

Applying Eq. 5-2, the general conservation equation (Eq. 5-1) can be written as

$$\int_A (\rho u_j \phi) n_j dA = \int_A \Gamma_\phi \frac{\partial \phi}{\partial x_j} \cdot n_j dA + \int_V s_\phi dV$$

Eq. 5-3

The integrations have to be now accomplished with the volume integral over the entire cell and with the area integral over the entire surface of the discrete control volume. The integrands of the surface integrals are called fluxes f , whereby f_c is the convective flux and f_d represents the diffusive flux.

$$f_c = (\rho u_j \phi) n_j$$

Eq. 5-4

$$f_d = \Gamma_\phi \frac{\partial \phi}{\partial x_j} \cdot n_j$$

Eq. 5-5

With the above definitions, the governing equations of the flow can be written in integral form as follows

Continuity (Eq. 4-6)

$$\int_V \rho \frac{\partial u'_i}{\partial x_i} dV = \underbrace{\int_A \rho u'_i \cdot n_i dA}_{\text{Convective Term}} \quad ; \quad \int_V \rho \frac{\partial \bar{u}_i}{\partial x_i} dV = \underbrace{\int_A \bar{\rho} u_i \cdot n_i dA}_{\text{Convective Term}}$$

Eq. 5-6

Momentum (Eq. 4-10)

$$\underbrace{\int_A \rho u_i u_j \cdot n_j dA}_{\text{Convective Term}} = - \underbrace{\int_A \bar{p} \cdot n_i dA}_{\text{Pressure Term}} + \underbrace{\int_A [(\tau_{ij})_{comb}] \cdot n_j dA}_{\text{Diffusive Term}}$$

Eq. 5-7

Turbulent kinetic energy (Eq. 4-14)

$$\underbrace{\int_A \rho k \bar{u}_j \cdot n_j dA}_{\text{Convective Term}} = \underbrace{\int_A \left[\frac{\mu_t}{\sigma_k} \left(\frac{\partial k}{\partial x_j} \right) \right] \cdot n_j dA}_{\text{Diffusive Term}} + \underbrace{\int_V (P - \rho \varepsilon) dV}_{\text{Source Term}}$$

Eq. 5-8

Turbulent dissipation (Eq. 4-16)

$$\underbrace{\int_A \rho \varepsilon \bar{u}_j \cdot n_j dA}_{\text{Convective Term}} = \underbrace{\int_A \left[\frac{\mu_t}{\sigma_\varepsilon} \left(\frac{\partial \varepsilon}{\partial x_j} \right) \right] \cdot n_j dA}_{\text{Diffusive Term}} + \underbrace{\int_V \left(\frac{\varepsilon}{k} (C_1 P - C_2 \rho \varepsilon) \right) dV}_{\text{Source Term}}$$

Eq. 5-9

5.3 Discretization

Surface integrals

In order to be able to discretize the surface integrals over the control volume, a geometrical surface division of the cell is performed where the number of cell faces is typically equal to the number of neighbours for each cell (boundary cells being the exception). After this, the flux f through each face of the CV is interpolated from the cell center values. Thus, the discretization of the surface integrals is done in the following way

$$\int_A f dA = \sum_l^{N_{faces}} F_l = \sum_l^{N_{faces}} \int_{A_l} f_l dA \approx \sum_l^{N_{faces}} f_l A_l \quad \text{with} \quad l = e, w, s, n, b, t \quad (\text{Figure 5-1})$$

Eq. 5-10

where

F_l = Flux through the surface l

f_l = Representative value of the flux f through face l . It can also be expressed as the value of the property ϕ convected through face l .

A_l = Area of face l .

N_{faces} = Number of faces enclosing the cell

Volume integrals

If it is supposed that a representative average value for a term q_ϕ exists in the center of the discrete volume, the discretization of the volume integral results as follows

$$Q_\phi = \int_V q_\phi dV = q_\phi \cdot V$$

Eq. 5-11

Approximation the gradient

The approximation of the diffusive terms in the Navier Stokes equations as well as certain source terms in the turbulent transport equations requires the computation of the gradient in the cell center P of the CV. This is approximated by the following equation

$$\left(\frac{\partial \phi}{\partial x_i} \right)_P \approx \frac{\sum_l^{N_{faces}} \phi_l n_l A_l}{V}$$

Eq. 5-12

where the value ϕ_l over the cell surface is calculated using an interpolation scheme.

5.3.1 Discretization the convective terms³

The convective flux for a general transport variable ϕ through the cell surface e is given by Eq. 5-4 and Eq. 5-10.

$$F_e^c = \int_{A_e} (\rho u_j \phi) n_j dA \approx \dot{m}_e \phi_e$$

Eq. 5-13

where \dot{m}_e is the mass flow through the face e .

The problem reduces now that for the convective flux $(f_c)_e$ it is require the face values ϕ_e and those quantities must be interpolated from the cell center values. Due to the flow in this thesis is not aligned with the grid (it crosses the grid lines obliquely), a second order upwind scheme⁴ is used to accomplish this interpolation.

³ In order to simplify the explanation, in the discretization of the convective and diffusive terms the cell surface e (Figure 5-1) of the control volume will be used as a representative surface.

⁴ Upwind means that the face value ϕ_e is derived from quantities in the cell upstream, or “upwind”, relative to the direction of the normal velocity.

5.3.2 Discretization the diffusive terms

Using Eq. 5-5 and Eq. 5-10 the diffusive flux F_e^d is approximated as follows

$$F_e^d = \int_{A_e} \Gamma_\phi \frac{\partial \phi}{\partial x_j} \cdot n_j dA = \Gamma_e \left(\frac{\partial \phi}{\partial x_j} \right)_e \cdot n_{j,e} A_e$$

Eq. 5-14

The gradient of ϕ is calculated in the cell centers P and E using Eq. 5-12 and then is interpolated to calculate the surface value through the face e .

5.3.3 Discretization the source terms

The source terms are calculated using Eq. 5-11 as

$$S_\phi = \int_V s_\phi dV = s_\phi \cdot V \approx (s_\phi)_P \cdot V$$

Eq. 5-15

5.3.4 Discretization the pressure term

The pressure term in the impulse equation is calculated using the integral theorem of Gauss and the Eq. 5-10 as follows:

$$-\int_V \frac{\partial p}{\partial x_i} dV = -\int_A p \cdot n_i dA \approx -\sum_l^{N_{faces}} p_l n_i A_l$$

Eq. 5-16

The Eq. 5-16 requires the value of the pressure at the cell surfaces l . Therefore, an interpolation scheme is required to compute the face values of pressure from the cell center values. For the case studied in this thesis, the variation of the pressure between the cell centers is smooth, so it is used a standard interpolation scheme to get the pressure surface quantities.

5.4 Pressure – Velocity coupling

As seen in Eq. 5-7, Eq. 5-13 and Eq. 5-16, to obtain the velocity field of the flow it is necessary to know the pressure field and the mass flow a priori. However, there is no relationship with the direct determination of the pressure for incompressible flows⁵, so the continuity equation is used to calculate the mass flow and the pressure field. This process leads on a pressure correction procedure, which was suggested in form of a SIMPLE algorithm (Semi-Implicit Method for Pressure-Linked Equations). This SIMPLE algorithm is used in the context of this work. The general form of the SIMPLE procedure is described by Patankar and it is not given here due to its lengthy arguments, but refers to [14].

⁵ For incompressible flows, the density is not directly related to pressure. Therefore, the continuity equation is independent of the pressure field and the SIMPLE algorithm is used to link both parameters.

5.5 Linearization of the set of equations

The Navier Stokes equations and the turbulent equations represented in the general transport equation (Eq. 5-1), contain the unknown scalar variable ϕ at the cell center as well as the unknown values in surrounding neighbour cells. Therefore, the set of equations are, non-linear with respect to these variables. To linearize those equations, it is used linear coefficients to relate the convective and diffusive terms.

The linearized form of Eq. 5-1 results in a linear algebraic equation for each partial volume:

$$A_P \phi_P = \sum_{NB} A_{NB} \phi_{NB} + b$$

Eq. 5-17

where

A_P, A_{NB}	Linearized convective and diffusive coefficients
NB	This subscript refers to neighbour cells.
b	Other terms as the pressure term in the impulse equation

Because the non-linearity of the governing flow equations, the change of the property ϕ has to be controlled. This is achieved by the under relaxation parameters, which reduces the change of ϕ iteration by iteration. In this way, the new value of the quantity ϕ within a cell depends upon the old value ϕ_{old} , the computed change $\Delta\phi$ and the under-relaxation factor, α , as follows:

$$\phi = \phi_{old} + \alpha \cdot \Delta\phi$$

Eq. 5-18

Where the change of ϕ is equal to the difference between the value computed and the old one ($\Delta\phi = \phi_{new} - \phi_{old}$). In this work, the under relaxation coefficients are fixed in the following values⁶ for all the simulations

Flow Variable	u_i	p	k	ε
Under-Relaxation Factor α	0.8	0.3	0.8	0.8

Table 5-1: Under relaxation factors used in the present work

5.6 Initial values and boundary conditions

5.6.1 Initial conditions

For internal flows, as the flow studied in this thesis, the velocity components and turbulent parameters on the inlet and the static pressure on the outlet are used in the whole domain to obtain the initial solution.

⁶ The values used for the under relaxation coefficients were reported as optimal for a large number of cases and are suitable for many problems. Furthermore, when running the simulation the convergence of the models was acceptable.

5.6.2 Boundary conditions

Inlet conditions

At the inlet, the velocity components, the turbulence kinetic energy and the turbulence dissipation rate are specified. The direction of the flow is established via the inlet flow angle β_1 , which depends on the operation range of the cascade.

The two turbulence parameters k and ε are specify using a turbulence intensity (T) and a mixing length (l_m).

The turbulence intensity is related to k and given by

$$T = 100 \sqrt{\frac{2k_{inlet}}{3u_{inlet}^2}} [\%]$$

Eq. 5-19

In the free stream region of the inlet plane, a turbulence intensity of 1% is assumed for all the simulations along the thesis. This value is set to 1% because it is commonly used for turbulent flow measurements and it is frequently found in the technical literature.

An expression for l_m can be obtained by applying the $k - \varepsilon$ model to an equilibrium near-wall boundary layer [3].

$$l_m = (C_\mu)^{3/4} \frac{k^{3/2}}{\varepsilon}$$

Eq. 5-20

Using Eq. 5-20, the rate of dissipation ε_{inlet} is determined via

$$\varepsilon_{inlet} = (C_\mu)^{3/4} \frac{k_{inlet}^{3/2}}{l_m} \quad \text{where} \quad (C_\mu)^{3/4} = 0.164$$

Eq. 5-21

The mixing length or dissipation length scale in Eq. 5-21 is estimated to 0.18% of the blade spacing [22].

Outlet conditions

Due to the characteristics of the flow (subsonic flow), the typical parameter at the outlet is the free stream static pressure. At the exit, the velocity components and turbulence parameters are extrapolated from the inner solution by assuming that the first derivatives of the flow properties are zero.

Periodic conditions

The periodic boundary condition is the easiest to implement due to it is simply a mathematically boundary condition. It ensures that all the variables have the same value at both ends of the computational domain. This boundary condition is needed in terms to

simulate a cascade distribution (creating the mesh only for one blade and then repeating it in circumferential direction).

Walls

The wall boundary conditions implemented states that there is no slip between the wall and the fluid. Consideration therefore was given as to how to make the model appropriate for such condition.

Experimental data shows that the flow near a wall can be divided in three different layers; the flow nearest the wall is predominantly laminar and has a linear velocity profile (this zone is named “viscous sublayer” due to the predominant role that plays the molecular viscosity), a transitional and intermittent with a log-linear velocity profile in the region of the transitional or buffer layer, and a fully turbulent layer with a logarithmic velocity profile in the outer region. The three subdivisions are plotted using non-dimensional coordinates in Figure 5-2.

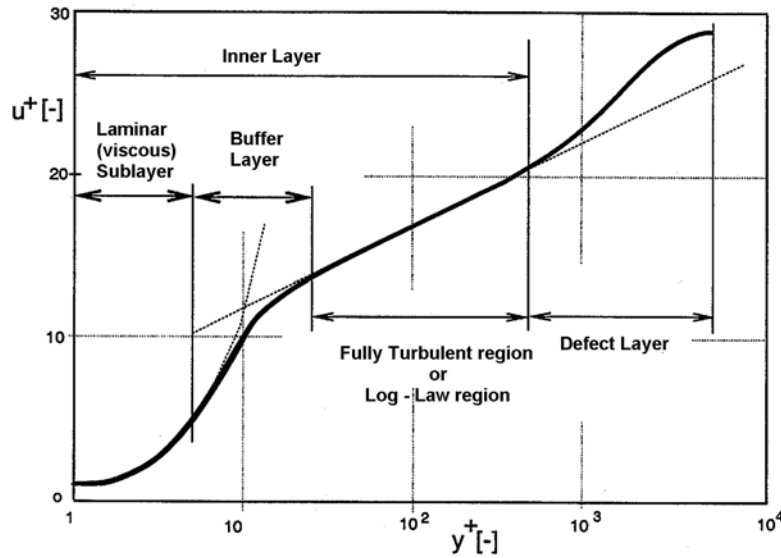


Figure 5-2: Subdivisions of the near-wall region [29]

As said in section 4.2.2, the $k - \varepsilon$ model is only valid for fully turbulent flows. Therefore, to make it suitable for wall-bounded flows, a semi-empirical formulas called “wall functions” are employed to bridge the viscosity affected inner region (viscous sublayer and buffer layer) and the fully turbulent region.

Wall functions

The “wall functions” defines a dimensionless velocity (u^+) and a characteristic non-dimensional distance from the wall (y^+)

$$u^+ = \frac{\bar{u}}{u_\tau} \quad ; \quad y^+ = \frac{\rho u_\tau y}{\mu}$$

Eq. 5-22

where u_τ is the wall friction velocity and its defined in terms of the shear stress at the wall (τ_w).

$$u_\tau = \sqrt{\frac{\tau_w}{\rho}}$$

Eq. 5-23

Although y^+ is a normalized distance, it is very helpful to think of it as a local Reynolds number that characterizes the state of the flow in the near-wall region. Thus the flow in the vicinity of the wall is laminar if the local Reynolds number is less than 5, is transitional between 5 and 30, and is fully turbulent if the Reynolds number is greater than 30.

The starting point to understand the way that the boundary layer is treated in the near wall layers is the momentum equation for a two-dimensional incompressible boundary layer

$$\rho \left(u \frac{\partial u}{\partial x} + v \frac{\partial u}{\partial y} \right) = -\frac{\partial p}{\partial x} + \mu \frac{\partial^2 u}{\partial y^2}$$

Eq. 5-24

For the laminar inner section, the wall boundary condition states that the velocity components in the wall are equal to zero, so the convective term in Eq. 5-24 is neglected. The pressure term is also set to zero as an assumption made to solve the equations. With this specifications, and time averaging the Eq. 5-24, the momentum turbulent boundary layer for the laminar sublayer is expressed as follows

$$0 = \frac{\partial}{\partial y} \left(\mu \frac{\partial \bar{u}}{\partial y} - \rho \overline{u'v'} \right) = \frac{\partial \tau_w}{\partial y}$$

Eq. 5-25

In Eq. 5-25 the shear stress has to be constant at the wall

$$\tau_w = \mu \frac{\partial \bar{u}}{\partial y} - \rho \overline{u'v'} = \text{Constant}$$

Eq. 5-26

As explained before, in the nearest layer to the wall the viscosity stresses plays a dominant role in the momentum exchange, so the term $\overline{u'v'}$ in Eq. 5-26 can be neglected.

$$\tau_w = \mu \frac{\partial \bar{u}}{\partial y}$$

Eq. 5-27

Then, substituting the non-dimensional variables and the wall friction velocity in Eq. 5-27, it leads to the well-known linear velocity wall law in the viscous sublayer.

$$u^+ = y^+ \quad ; \quad y^+ < 5$$

Eq. 5-28

On the other hand, for the outer layer, where the turbulence plays a major role, the momentum turbulent boundary layer is

$$u \frac{\partial u}{\partial x} + v \frac{\partial u}{\partial y} = -\frac{1}{\rho} \frac{\partial p}{\partial x} + \frac{\partial}{\partial y} \left(\mu \frac{\partial \bar{u}}{\partial y} - \rho \overline{u'v'} \right) \quad \text{with} \quad \left| \mu \frac{\partial \bar{u}}{\partial y} \right| \ll \left| -\rho \overline{u'v'} \right|$$

Eq. 5-29

Performing a dimensional analysis where the mean velocity is a function of the wall shear stress, the physic properties of the fluid and the distance y from the wall; the logarithmic velocity wall-law can be expressed as

$$u^+ = \frac{1}{\kappa} \ln(Ey^+) \quad ; \quad y^+ > 30$$

Eq. 5-30

where κ is the von Karman constant which has a value of about 0.41, and E is a further empirical constant which assumes a value of about 9.0 for aerodynamically smooth walls.

An alternative treatment for the wall functions used by FLUENT is to define a dimensionless velocity (u^*) and a characteristic non-dimensional distance from the wall (y^*) is this way

$$u^* = \frac{\rho \bar{u} C_\mu^{1/4} k^{1/2}}{\tau_w} \quad ; \quad y^* = \frac{\rho C_\mu^{1/4} k^{1/2} y}{\mu}$$

Eq. 5-31

With the above definitions the laminar stress-strain relationship can be written as

$$u^* = y^*$$

Eq. 5-32

and the logarithmic velocity wall-law yields

$$u^* = \frac{1}{\kappa} \ln(Ey^*)$$

Eq. 5-33

The logarithmic law for mean velocity is known to be valid for $y^* > 30$, but in FLUENT the log-law is employed when $y^* > 11.225$ [5].

It should be noted that the last definition of the law of the wall is based on the wall unit y^* , rather than y^+ . These quantities are approximately equal in equilibrium turbulent boundary layers but they differ when the boundary layer is not stable (i.e. flow separation tendency) by the fact that y^* depends on the turbulent kinetic energy and y^+ depends on the wall friction velocity. To illustrate this feature a simulation of the flow over a profile where there is flow separation tendency at the rear part of the blade was developed and the results are showed in Figure 5-3.

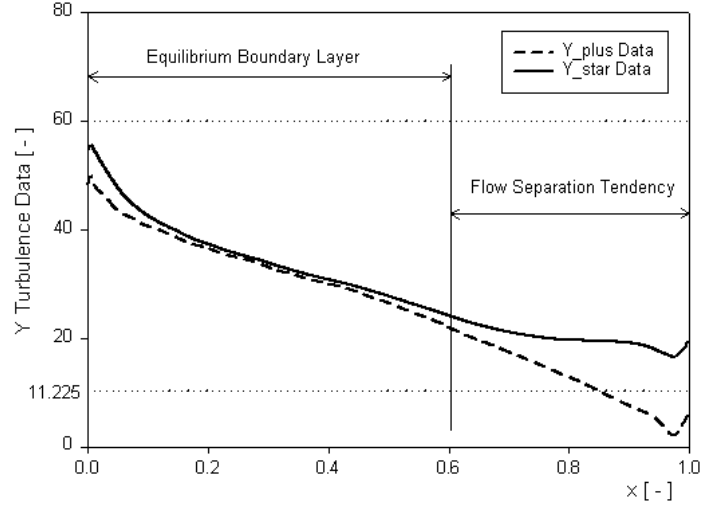


Figure 5-3: Comparison between y^+ and y^*

In the simulations performed in this thesis, it is expected the logarithmic wall profile for the velocity in the vicinity of the wall. Therefore the grid is generated in such a way that the parameter y^* in the nearest cell to the wall is higher than 11.225 and lower than 60.

5.7 Normalization

The governing fluid and turbulence equations are cast into dimensionless form in order to normalize all the variables preferably to order unity. Thus, the flow parameters are scaled using as reference values the chord of the first profile in the tandem blade (c_1), the inlet velocity (w_1) and the constant density (ρ_{ref}). Table 5-2 shows the normalization relations.

Variable	Non-dimensional representation [-]
x_i [m]	$\frac{x_i}{x_{ref}} = \frac{x_i}{c_1} = x_i^*$
u_i [m/s]	$\frac{u_i}{u_{ref}} = \frac{u_i}{w_1} = u_i^*$
ρ [kg/m ³]	$\frac{\rho}{\rho_{ref}} = \rho^* \equiv 1$
p [Pa]	$\frac{p}{\rho_{ref} w_1^2} = p^*$
$\mu, \mu_{comb}, \mu_{turb}$ [kg/m s]	$\frac{\mu}{\rho_{ref} w_1 c_1}, \frac{\mu_{comb}}{\rho_{ref} w_1 c_1}, \frac{\mu_{turb}}{\rho_{ref} w_1 c_1} = \text{Re}^{-1}, \text{Re}_{comb}^{-1}, \text{Re}_{turb}^{-1}$
k [m ² /s ²]	$\frac{k}{w_1^2} = k^*$
ε [m ² /s ³]	$\frac{\varepsilon}{w_1^3 / c_1} = \varepsilon^*$

Table 5-2: Normalization parameters

5.8 Solution the governing equations

The numerical procedure requires the solution of 3 equations for Navier Stokes (two equations of momentum and one equation of mass conservation) and 2 equations for turbulence. The equation system is solved sequentially (segreated one from other) following the steps described in Figure 5-4.

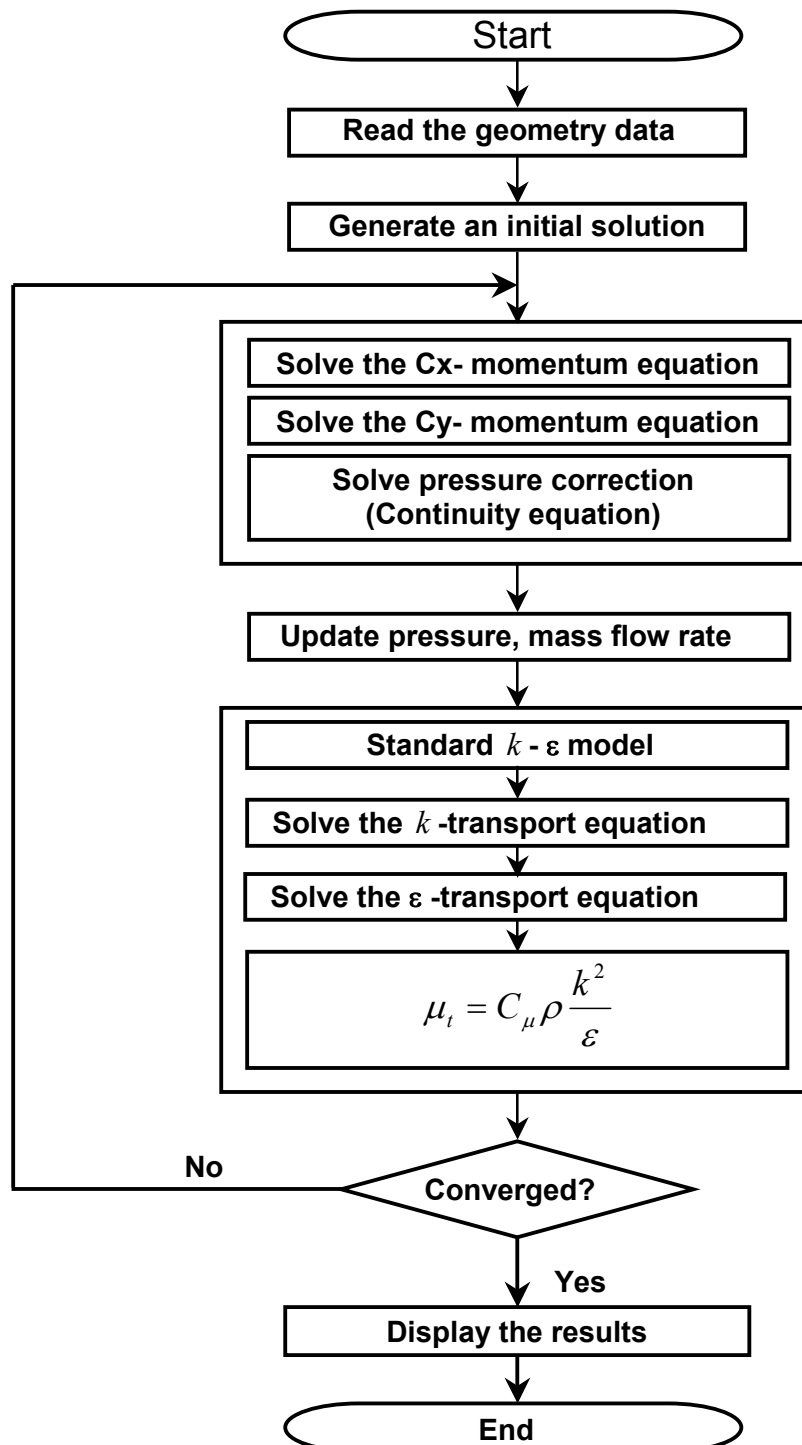


Figure 5-4: Overview of the solution method

5.9 Numerical method summary

A summary of the numerical method implemented for all the simulations is presented in Table 5-3.

Model	Steady, two dimensional, incompressible
Governing equations	Dimensionless form
Viscous model	$k - \varepsilon$ with standard wall functions
Solver	FLUENT 6.0 (Segregated method)
Materials	
Density	$\rho^* = 1$ [-]
Viscosity	Re^{-1}
Discretization	
Pressure	Standard
Pressure – Velocity coupling	SIMPLE
Momentum	Second order upwind
Turbulence kinetic energy	Second order upwind
Turbulence dissipation rate	Second order upwind
Under relaxation factors	Table 5-1
Boundary Conditions	
Inlet	
Velocity components	The velocity components are established via the inlet flow angle β_i with a non-dimensional velocity magnitude of $w_i^* = 1$ [-]
Turbulence kinetic energy	The turbulence kinetic energy (k_1^*) is set via an inlet turbulence intensity of 1% and the non-dimensional velocity magnitude at the inlet (w_i^*).
Turbulence dissipation rate	The turbulence dissipation rate (ε_1^*) is established via the turbulence kinetic energy at the inlet (k_1^*) and a mixing length estimated to 0.18% of the blade spacing.
Outlet	
Static pressure	$p_2^* = 0$ [-]
Turbulence parameters	$\frac{\partial k_2^*}{\partial x^*} = 0$; $\frac{\partial \varepsilon_2^*}{\partial x^*} = 0$
Stationary wall	
Shear condition	No slip
Wall treatment	Standard Wall Functions
Periodic	
Periodic type	Translational

Table 5-3: Numerical method specifications

5.10 Convergence criteria

“A truly converged solution is one that is no longer changing with successive iteration. If the residuals for all problem variables fall below the convergence criteria but are still in decline, the solution is still changing, to a greater or lesser degree.”

Fluent news

In the present investigation various simulations are performed and one of the goals is to compare the results between the different models. Therefore, to guaranty that the solutions are no changing, all the simulations were running to the convergence at the level of machine accuracy. This point occurs when the residual flatten in the residual plot. Figure 5-5 illustrates a residual graph representative for all the models in the thesis.

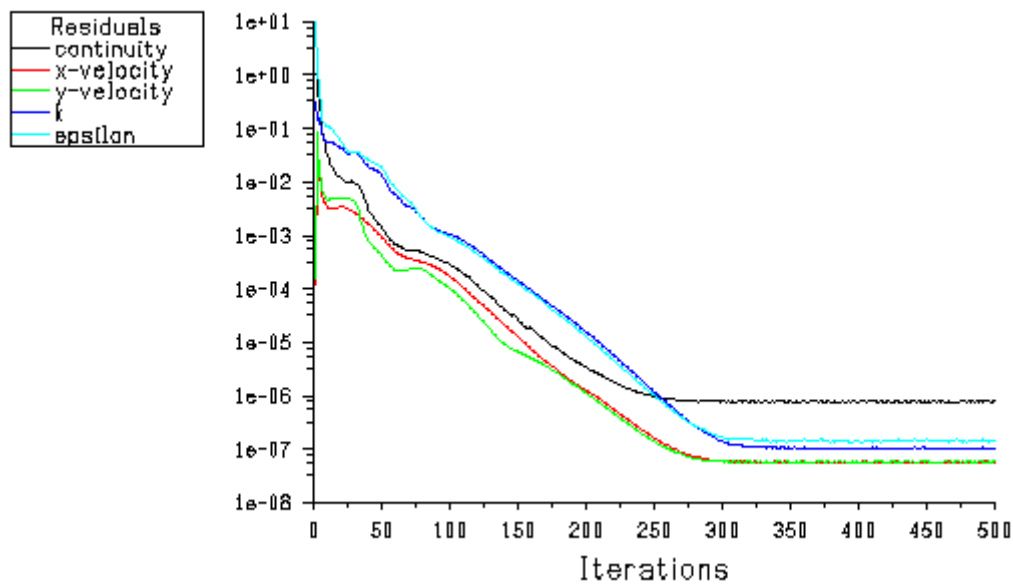


Figure 5-5: Residual plot. Convergence at the level of machine accuracy

6 Validation: Flow simulation in a NACA65 compressor cascade

To validate the turbulence and the numerical model, a simulation of the two-dimensional flow field in a linear compressor cascade at various incidences was developed. Seven different inlet flow angles, varying from high positive incidence to high negative incidence have been simulated. The computational results are compared with experimental data reported in [7] and with numerical data available in [22].

6.1 Cascade geometry

The blade profile corresponds to one of the many blades experimentally tested at low speeds by Emery et al. [7] and numerically investigated by Trenker [22] using a $k-\varepsilon$ model with wall functions in a finite-element based Navier-Stokes solver.

The geometry of the cascade was obtained in the NACA 1368 report and was generated using the procedure described in Appendix 1. The geometrical parameters are summarized in Table 6-1.

Geometrical parameters	
<i>Blade geometry</i>	NACA 651510
<i>Solidity</i>	$c/s = 1$
<i>Stagger angle</i>	$\gamma = 30.48^\circ$

Table 6-1: Geometrical parameters NACA651510

6.2 Inlet flow field and operating conditions

Emery et al. [7] reported a magnitude of the inlet velocity, measured in the free stream, of about $w_1 = 28.956$ m/s. However the analysis is non-dimensional, this velocity is used to calculate the upstream Mach number:

$$M_1 = \frac{w_1}{\sqrt{\kappa RT}} \approx 0.0845$$

Eq. 6-1

where the isentropic exponent κ is 1.4, the gas constant R is 286 J/kgK and the temperature is 293 K.

Since the compressibility effects of the flow has to be taken into account when the Mach number is higher than 0.2, the flow field under investigation is essentially incompressible.

Blade chord Reynolds number calculated with the constant inlet velocity (w_1) and the reported chord length ($c = 127\text{mm}$) is set to $\text{Re}_1 \approx 245000$.

The design angle of attack is fixed at 15° as indicate Figure 3-2 for the geometrical parameters of the blade. Thus, the inlet flow angle at design point is $\beta_{1d} = 45^\circ$.

The operating conditions of the cascade are estimated using the corresponding blade Mellor diagram. Figure 6-1 shows that the maximum negative and positive incidences acceptable for the stated design conditions are 39.5° and 52° respectively.

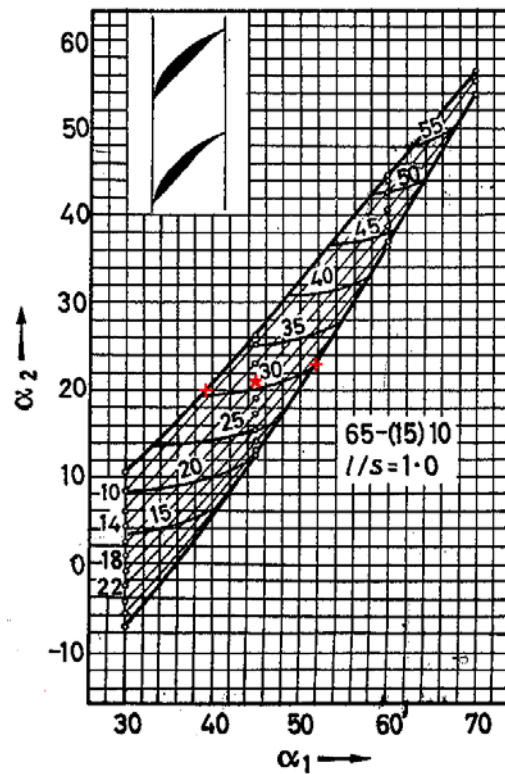


Figure 6-1: Mellor diagram. NACA651510, $\sigma = 1$ [8]

Due to the fact that Mellor specifies the blade stall when the total losses are 1.5 times the minimum losses and Lieblein states twice the minimum losses as the stall point; for the present simulation values slightly higher than those obtained by Mellor will be used as maximum incidences. Thus, the maximum negative incidence is set to 36° and the maximum positive incidence to 54° .

6.3 Numerical procedure

6.3.1 Numerical method

The set of governing equations defined in Chapter 4, for a steady two-dimensional incompressible flow, was solved numerically by the non-dimensional finite volume method of Chapter 5.

6.3.2 Finite volume mesh

A mesh formed by a structured region near the blade surface and an unstructured region on the remainder of the computational domain was used. Figure 6-2 shows the final mesh that consists approximately of 5300 quadrilateral cells.

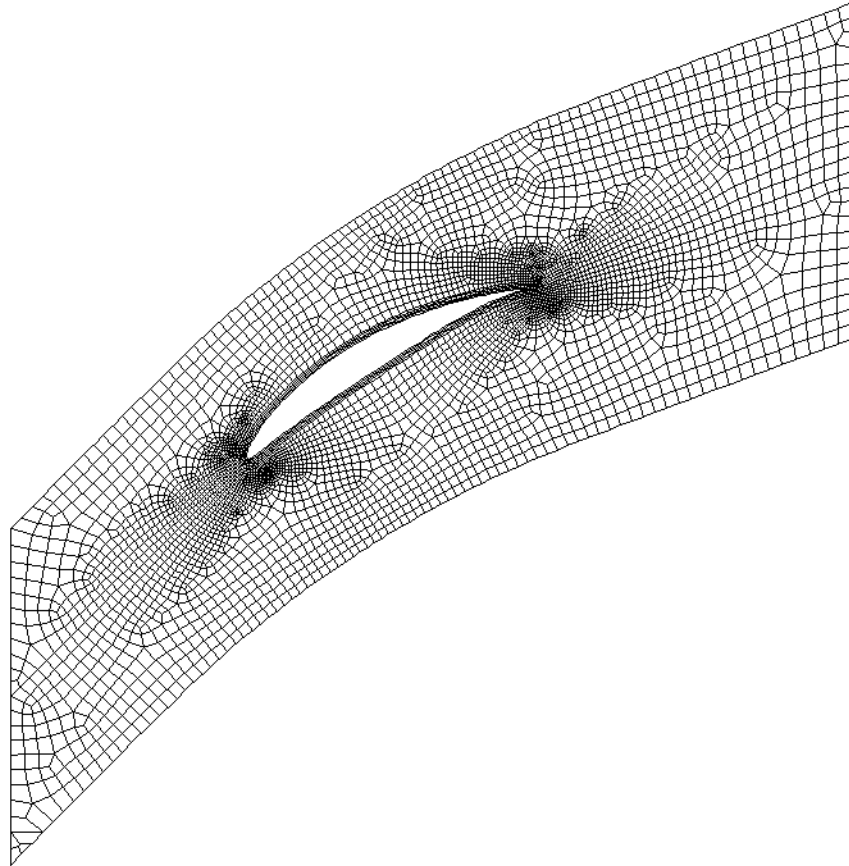


Figure 6-2: Finite volume mesh. NACA651510

The mesh density is higher where the velocity gradients are higher, that means in the proximities of the leading and trailing edges. Figure 6-3 illustrates a mesh detail for the blade tested.

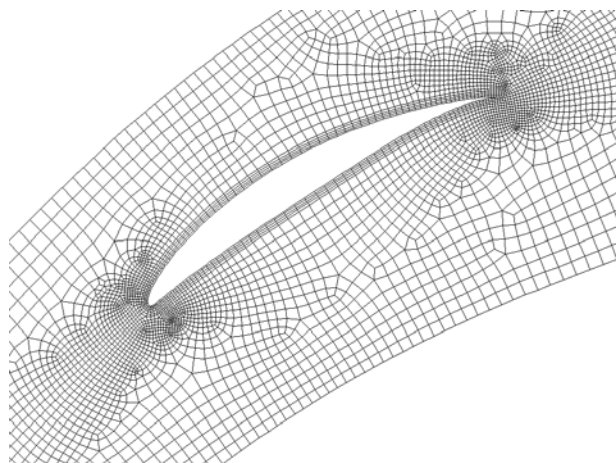


Figure 6-3: Mesh detail. NACA651510

With the boundary layer modelling the grid should be highly densified in the proximities of the walls. The wall functions model are used to capture the blade boundary layers and special consideration needs to be given to the cell size adjacent to the wall. Therefore, the thickness of the elements near to the blade surface was adjusted to satisfy the condition $y^* > 11.225$, with y^* as the non-dimensional parameter defined in section 5.6.2. The plots of y^* for maximum and minimum incidence are presented in Figure 6-4.

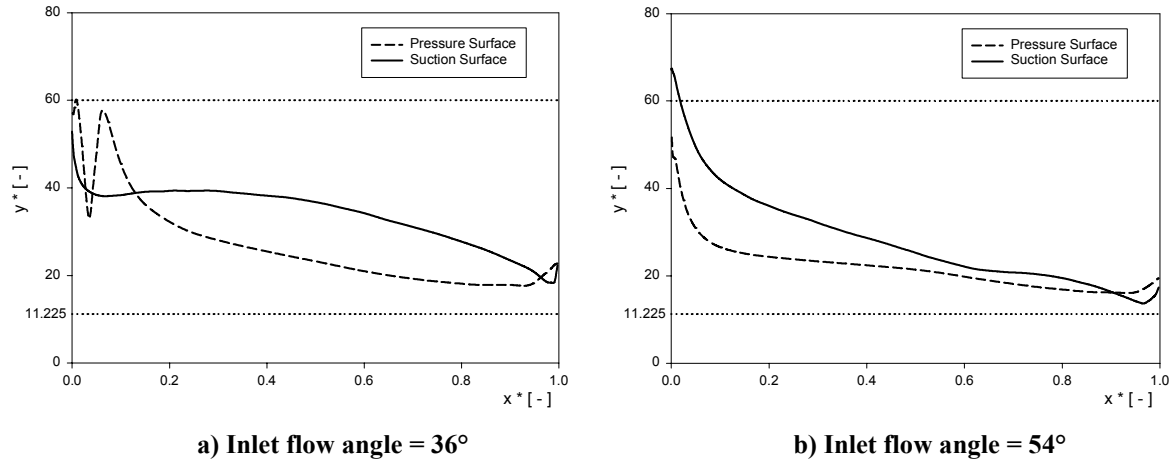


Figure 6-4: y^* values NACA651510 simulation

Due to the high gradients of pressure in the vicinity of the leading and trailing edge these areas are the most critical in terms of meshing. The grid cells needs to be designed so that the skewness would be as small as possible. A detail of the final mesh around the leading and trailing edge is illustrated in Figure 6-5.

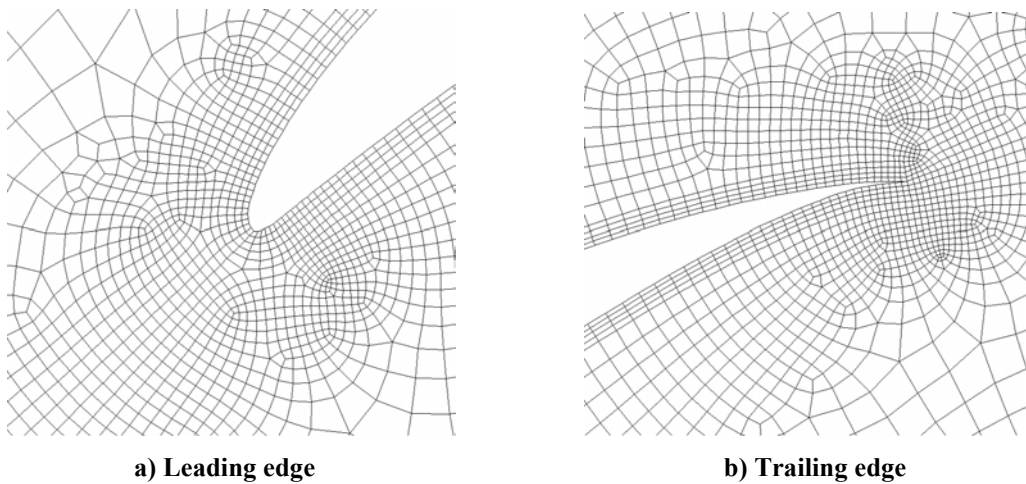


Figure 6-5: Enlargement of the final mesh

6.4 Results and discussion

The first part of the investigation was made on the basis of the following local quantities: blade surface pressure distribution and total pressure coefficient. The second part of the study is based on the pitchwise mass average flow angle and the pitchwise mass average total pressure coefficient.

Static pressure coefficient

A comparison between the static pressure coefficient at design point and the experimental and numerical data available in the literature is illustrated in Figure 6-6. The agreement between the measured values and the Finite volume method is acceptable (Figure 6-6a). In addition it is remarkable that the results obtained by both, finite volume and finite element, are almost the same (Figure 6-6b).

The flow behaviour along the blade shows an initial acceleration on the suction surface up to 20% of the chord from the leading edge. Thereafter a constant deceleration of the flow towards the trailing edge is noticeable. On the pressure surface the static pressure distribution remains almost constant along the blade.

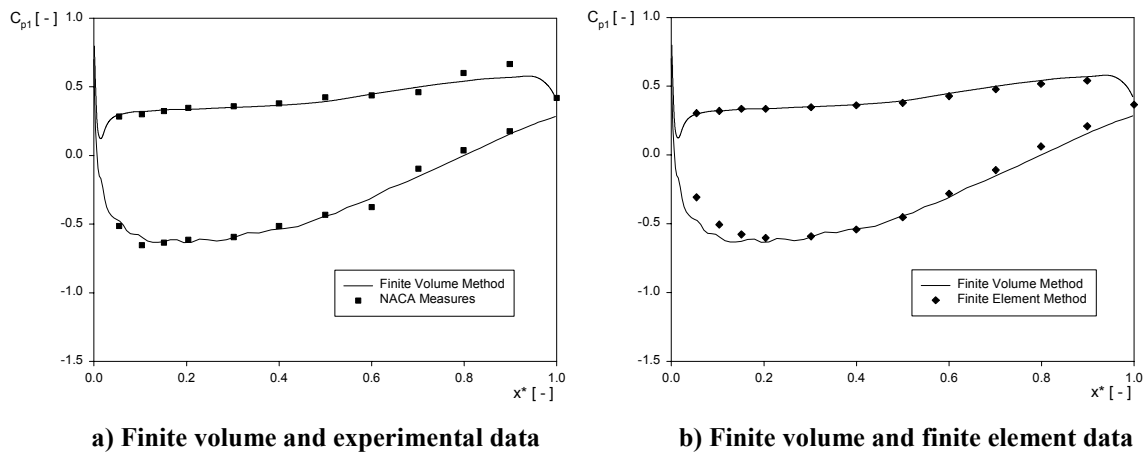


Figure 6-6: Blade pressure distribution at design incidence

The distribution of the pressure along the blade at off design incidence is plotted in Figure 6-7 for inlet angles of 36° and 54° . At maximum negative incidence (Figure 6-7a) the stagnation point moves toward the suction side. Due to the flow around the blade leading edge, high velocities occur on the pressure side near the leading edge, causing a separation tendency in this area. This separation tendency occurs approximately 5% of the chord and it is evident as a step in the deceleration processes that takes place in the pressure surface near the leading edge.

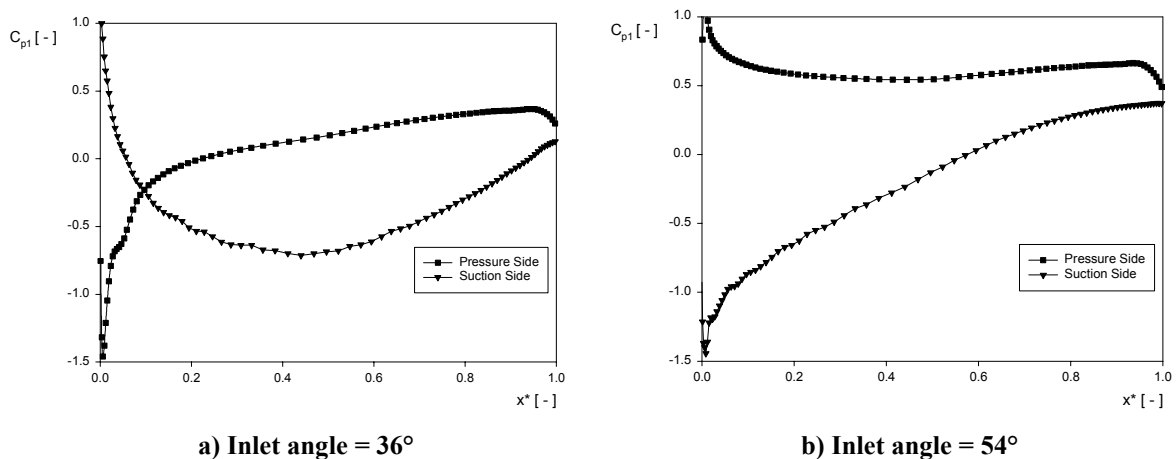


Figure 6-7: Profile pressure distribution at off design incidences

For positive incidences the maximum pressure difference is shifted toward the front of the blade. In Figure 6-7b there is a flow separation tendency in the rear part of the blade. This tendency is due to the high diffusion process along the suction side.

Total pressure loss coefficient

Total pressure coefficient calculated in the outlet plane (one chord from the trailing edge) is plotted in Figure 6-8 for maximum positive incidence, design incidence and maximum negative incidence.

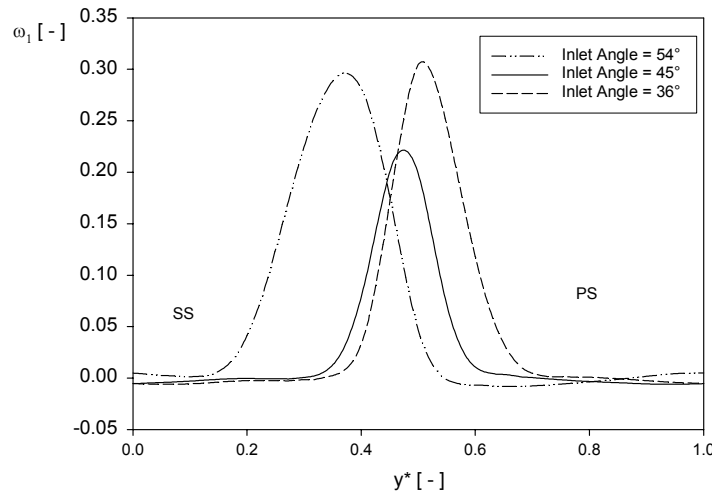
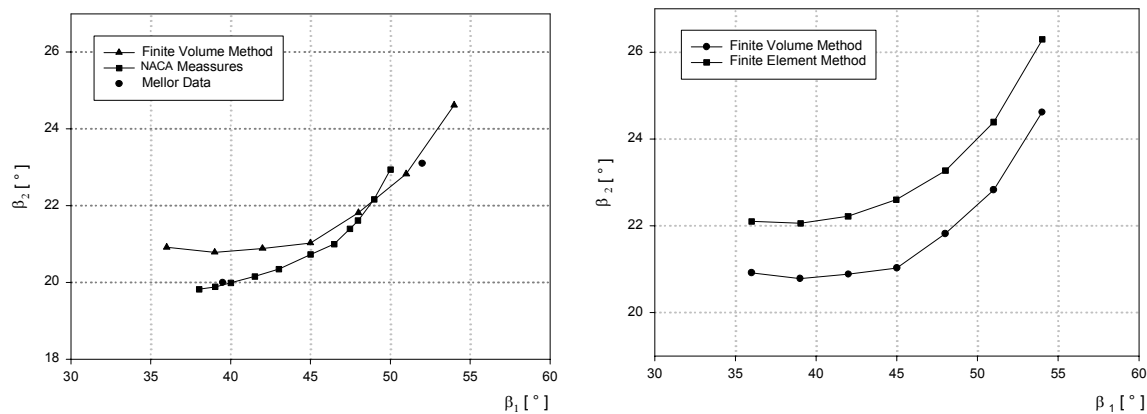


Figure 6-8: Total pressure loss coefficient

The total pressure coefficient indicates the regions where the losses occur. As seen in Figure 6-8, the inviscid region with no losses is presented by $\omega_1 \approx 0$. The losses are concentrated in the wake and it results evident that the minimum losses occur for design incidence. The loss profile for off design incidences shows thicker wake indicating higher growth of boundary layer, and hence high losses.

Pitchwise mass average flow angle

Figure 6-9 shows the pitchwise mass average flow angle as a comparison between the results obtained in the finite volume simulation and the experimental and numerical data reported in the technical literature.



a) Finite volume and experimental data

b) Finite volume and finite element data

Figure 6-9: Pitchwise mass averaged flow angle versus inlet flow angle

Starting with the condition at maximum positive incidence ($\beta_1 = 54^\circ$), the computed and the measured flow angles decreases with decreasing the inlet flow angle.

For positive incidence the agreement between the measured and computed averaged flow angles is better than for negative incidences. At design incidence the difference between both is about 0.2° , which means that the results obtained by the numerical calculation are reliable. There exist a constant difference of approximately 1° between the finite volume and the finite element results (Figure 6-9b).

Pitchwise mass average total pressure loss coefficient

The mass average loss coefficient was calculated from the wake survey by means of measuring the total pressure at the outlet plane. The variation of loss coefficient with different inlet angles for the tested cascade is shown in Figure 6-10. Loss coefficient values are found to be low over the entire range for the measured data due to the fully turbulent treatment given to the flow in the computational calculations. However, it is observed that the CFD-code was able to predict accurately loss increments for the variation in the aerodynamic parameters of the cascade.

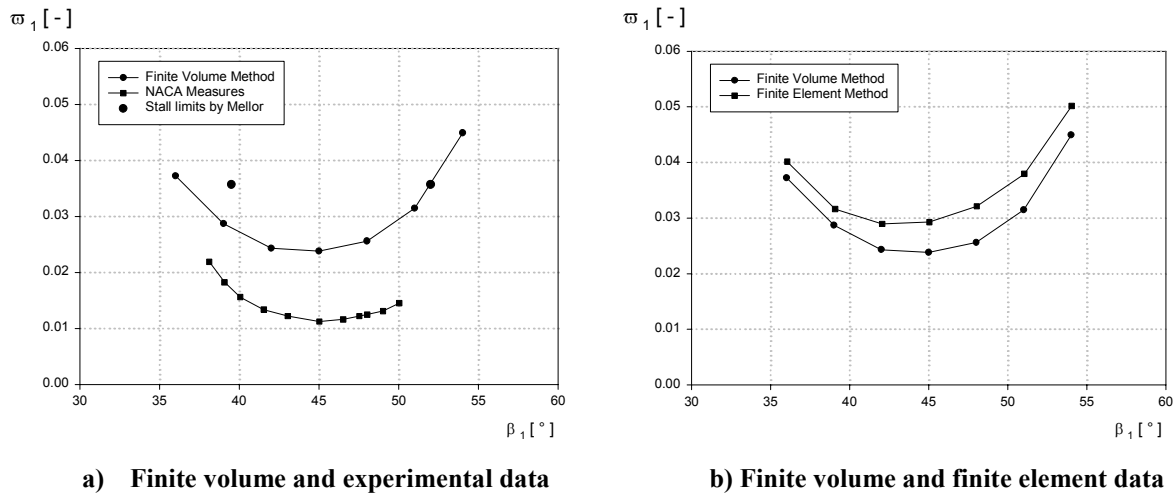


Figure 6-10: Pitchwise mass averaged loss coefficient versus inlet flow angle

The minimum measure profile loss coincides with the minimum computed profile loss coefficient at an inlet flow angle of about $\beta_1 \approx 45^\circ$.

The stall incidence angles using the condition imposed by Mellor (1.5 times the minimum losses) in the numerical calculation are $\beta_1 = 36.5^\circ$ for negative incidence and $\beta_1 = 52^\circ$ for positive incidence. Those results are very near with the experimental data obtained in the Mellor diagram (the maximum difference is about 3° for negative incidence).

It is interesting to remark the fact that the losses obtained by the finite volume method were lower than those obtained using a finite element calculation.

6.5 Validation summary

From the validation of the turbulence and numerical model a short summary is given before moving onto the main results. For the turbulence model it is sufficient to use the classical $k - \varepsilon$ model with wall functions as seen in the results obtained. In regards to the numerical model the finite volume method is adequate since the numerical results are quite similar with the experimental data. The comparison between the finite volume and the finite element method shows that the results obtained in both methods are very close.

7 Tandem blades: influence of the relative position

In order to recognize the interaction mechanisms between the two profiles that conform a tandem blade, a numerical simulation of a linear high turning compressor stator cascade using tandem blade rows is performed. The comparison between the blades acting independently and a tandem blade for various relative blade positions will lead to identify the mechanisms that affect the flow along the tandem arrangement.

To answer the question if the numerical computation is able to predict the main features of the tandem cascade flow field, the validation of the result is taken into account by a qualitative comparison with experimental data reported by Bammert and Staude [2]. A detailed description of the results of Bammert's investigation was summarised in section 2.3.2.

7.1 Inlet conditions

The overall data at design conditions chosen for the present simulation read as follows: The incoming flow with an inlet Mach number lower than 0.2 is considered incompressible. An inlet flow angle of $\beta_1 = 65^\circ$ has to be turned 46° , thereby the flow is diffused to leave the device with an outlet angle of approximately 19° at a reasonable low total pressure loss level. The Reynolds number calculated with the inlet velocity (w_1) and the chord of the first profile (c_1) is set for all the simulations to $Re = 245000$. Therefore, the overall Reynolds number defined with the inlet velocity (w_1) and the overall chord of the tandem blade (c_t) is always higher than 450000.

Due to the many variables that influence the design of a tandem cascade, the present work will take the following assumptions to perform the investigation:

- The front and rear profiles in the tandem cascade have the same chord ($c_1 = c_2$).
- The number of blades in the front and rear row of the cascades is the same. That means that the solidity of the front blade row, defined as $\sigma_1 = c_1/s$, is equal to the solidity of the second blade row ($\sigma_2 = c_2/s$).

The guideline used to choose the profile geometry was influenced by the results reported by Wennerstrom [25]. Thus, a tandem blade with approximately 50-50 % loading split, formed by a low cambered first blade NACA651210 that deflect the flow roughly 15° and a high cambered second blade NACA652110 responsible for the remained flow deflection of more than 30° , was chosen. The stagger angle for both blades was calculated at design point using blade's Mellor diagram. Detailed cascade blade geometry is summarized in Table 7-1

Blade variables	Front blade	Rear blade
Blade profile	NACA 651210	NACA652110
Stagger angle (°)	55°	30°
Solidity [-]	$\sigma_1 = 1$	$\sigma_2 = 1$

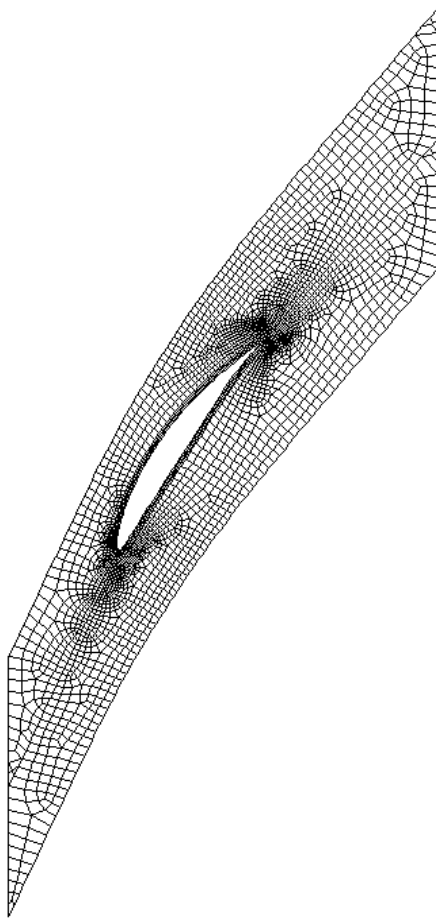
Table 7-1: Tandem cascade blade geometry

7.2 Initial configuration

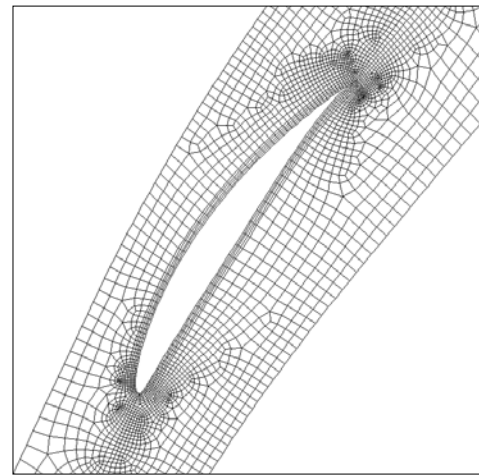
The first step in the investigation is to characterize the flow when there is no influence between the two blades that conform the tandem cascade. This is achieved by setting the axial displacement of the rear profile to a high value denoted as “a = inf”. In this case the whole arrangement will be treated as two isolated blades. Thus, two different models (related to each profile) are evaluated and the results are compiled into an equivalent tandem blade with high axial displacement.

7.2.1 Finite volume mesh

A mesh illustration and a specification of the mesh characteristics for each model are shown in Figure 7-1 and Figure 7-2.



a) Entire mesh

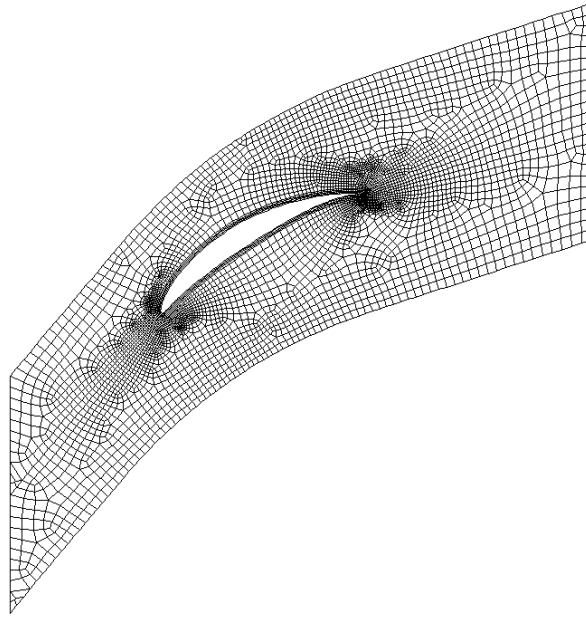


b) Mesh detail

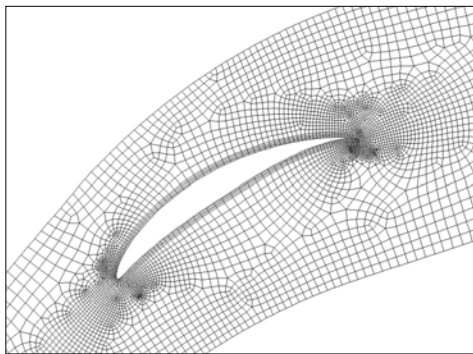
Total cells	3600
Topology	Structured near the blade surface and unstructured on the remainder of the computational domain

c) Mesh characteristics

Figure 7-1: Finite volume mesh. Front blade NACA651210



a) Entire mesh



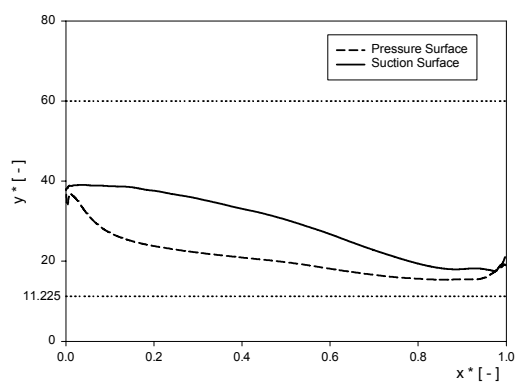
b) Mesh detail

Total cells	5300
Topology	Structured near the blade surface and unstructured on the remainder of the computational domain

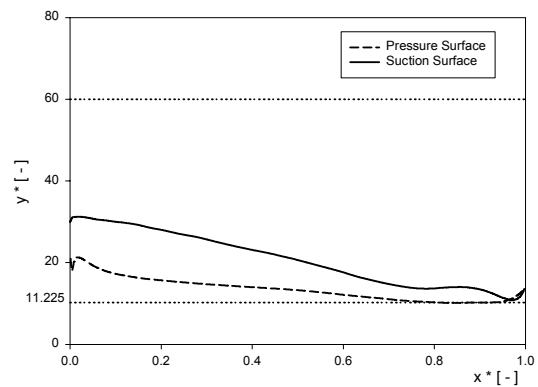
c) Mesh characteristics

Figure 7-2: Finite volume mesh. Rear blade NACA652110

The structured elements near the blade surface were adjusted to satisfy the value of $y^* > 11.225$. The plots of y^* for both models are presented in Figure 7-3.



a) Front blade



b) Rear blade

Figure 7-3: y^* values. Initial tandem configuration

7.2.2 Front blade results

The main results obtained for the first profile are summarized in Table 7-2.

<i>Mass average results front blade</i>			
Inlet velocity magnitude *	w_1	[-]	1
Inlet flow angle *	β_1	[°]	65
Outlet velocity magnitude	w_{12}	[-]	0.6741
Outlet flow angle	β_{12}	[°]	50.75
Deceleration	$\frac{w_{12}}{w_1}$	[-]	0.6741
Deflection angle	$\theta_1 = \beta_1 - \beta_{12}$	[°]	14.25
Diffusion factor	$(DF)_1$	[-]	0.52
Loss coefficient	$(\varpi_1)_1$	[-]	0.036

* Inlet parameters

Table 7-2: Numerical results. Front tandem blade

The numerical value for the outlet angle is quite similar with the experimental result reported by Mellor, which states an outlet angle of approximately 50.5°. A diffusion factor of 0.52 shows a highly loaded first blade. The load along the blade is attributed to the high flow deceleration of 0.68.

The pressure coefficient along the blade (Figure 7-4) shows an initial acceleration on the suction surface up to 30% of the chord from the leading edge. Thereafter a constant deceleration of the flow towards the trailing edge is noticeable. On the pressure surface the static pressure distribution remains almost constant along the blade. It is also evident a flow separation tendency near the trailing edge (95% of the chord).

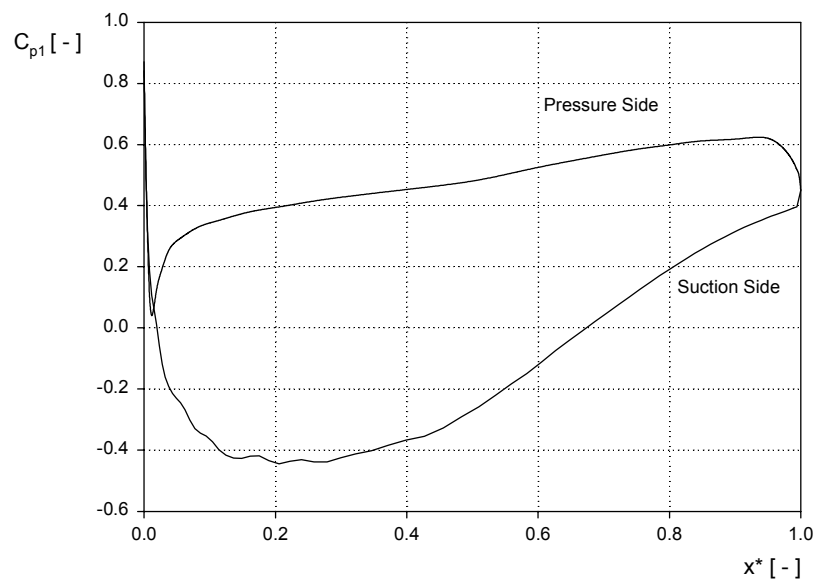


Figure 7-4: Pressure coefficient. Front blade of the tandem arrangement

7.2.3 Rear blade results

Table 7-3 presents the numerical results obtained for the rear blade.

<i>Mass average results rear blade</i>			
Inlet velocity magnitude *	w_{12}	[-]	0.6741
Inlet flow angle *	β_{12}	[°]	50.75
Outlet velocity magnitude	w_2	[-]	0.4572
Outlet flow angle	β_2	[°]	19.22
Deceleration	$\frac{w_2}{w_{12}}$	[-]	0.6782
Deflection angle	$\theta_2 = \beta_{12} - \beta_2$	[°]	31.52
Diffusion factor	$(DF)_2$	[-]	0.6
Loss coefficient	$(\varpi_1)_2$	[-]	0.016

* Values obtained in the front blade simulation (section 7.2.2)

Table 7-3: Numerical results. Rear tandem blade

The numerical quantities were comparable with the experimental data reported by Mellor. Thus, the difference between the experimental outlet angle and the value calculated was lower than 1°. A diffusion factor of 0.6 and a de Haller number of 0.67 indicates that the blade is highly loaded.

Figure 7-5 illustrates the pressure coefficient along the blade. The flow behavior shows an initial acceleration in the front part of the blade suction surface up to 10% of the chord. Thereafter the flow decelerates toward the trailing edge. A flow separation near the 90% of the chord is evidenced when the pressure gradient starts leveling off in the plot.

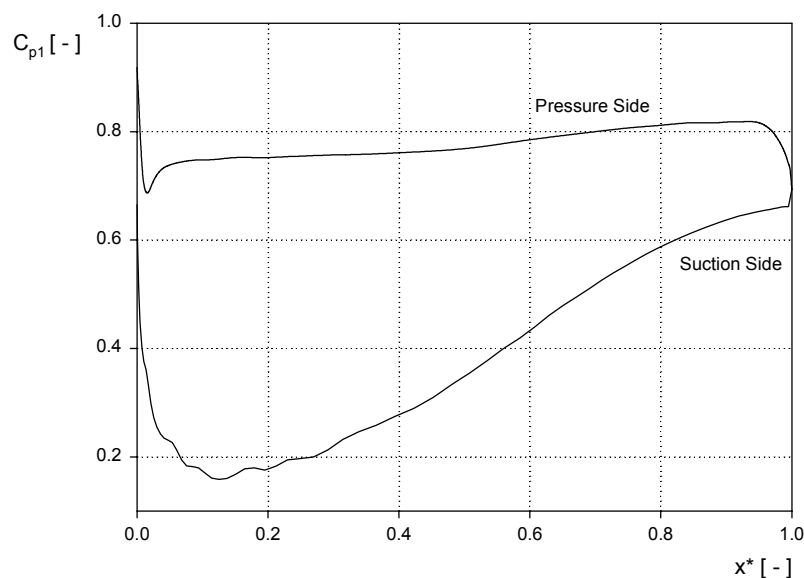


Figure 7-5: Pressure coefficient. Rear blade of the tandem arrangement

7.2.4 Tandem blade ($a = \text{inf}$): results summary

The results of the independent blades reported in sections 7.2.3 and 7.2.4 are joined to conform an equivalent tandem blade with high axial displacement ($a = \text{inf}$). The final tandem data is summarized in Table 7-4.

<i>Mass average results. Tandem blade $a = \text{inf}$.</i>			
Flow deceleration	$\frac{w_2}{w_1}$	[-]	0.4572
Deflection angle	$\theta = \beta_1 - \beta_2$	[°]	45.7°
Loading split		[%]	46.4 – 53.6
Loss coefficient	$\varpi_1 = (\varpi_1)_1 + (\varpi_1)_2$	[-]	0.052

Table 7-4: Numerical results. Tandem blade $a = \text{inf}$

It is important to remark the fact that the main part of the losses occurs in the front blade (70% of the total losses). This is due to the high inlet velocity magnitude (w_1) compared with the inlet velocity (w_{12}) at the rear profile.

7.3 Tandem blade simulations

In this section, the flow along the tandem blade will be studied using different simulations for various relative blade positions. In all the tandem models the front blade is fixed and the rear blade varies its position as a function of the axial and tangential displacement.

Two different approaches are chosen to identify the influence of the rear blade location in the tandem arrangement:

- The blade is positioned in such a way that there are no gap nozzle effects between the profiles.
- The blade is positioned in the vicinity of the trailing edge of the front profile in order to create a gap nozzle area.

Figure 7-6 shows a graphical discretization of the possible second blade locations in terms of gap nozzle effect. The division of the domain was done using a perpendicular line to the flow path at the trailing edge of the front profile in a tandem blade with $a=\infty$.

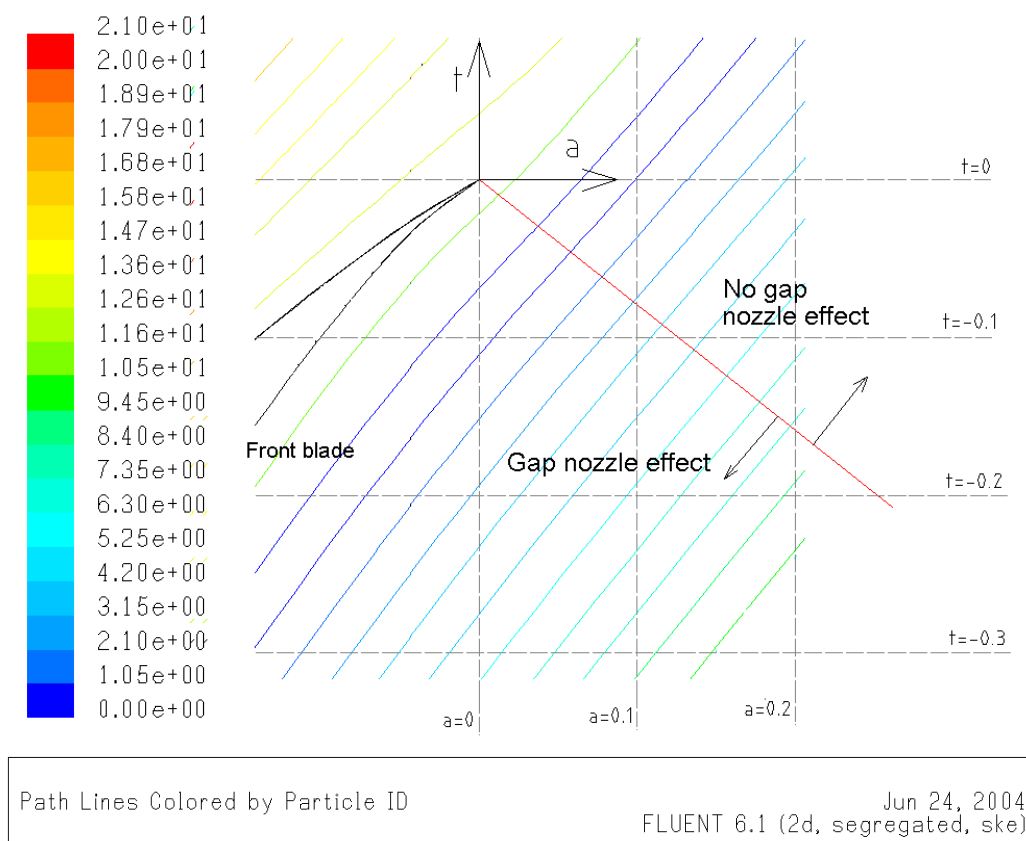


Figure 7-6: Gap nozzle area discretization

7.3.1 Finite volume mesh

The mesh generated for each tandem configuration was developed using a GAMBIT mesh algorithm detailed in Appendix 3. Due to the fact that each model needs a different mesh, it results inconvenient to show the mesh for all the tandem blades tested. Therefore, only one representative mesh corresponding a tandem blade with an axial displacement of -0.025 and a tangential displacement of -0.2 is shown in Figure 7-7.

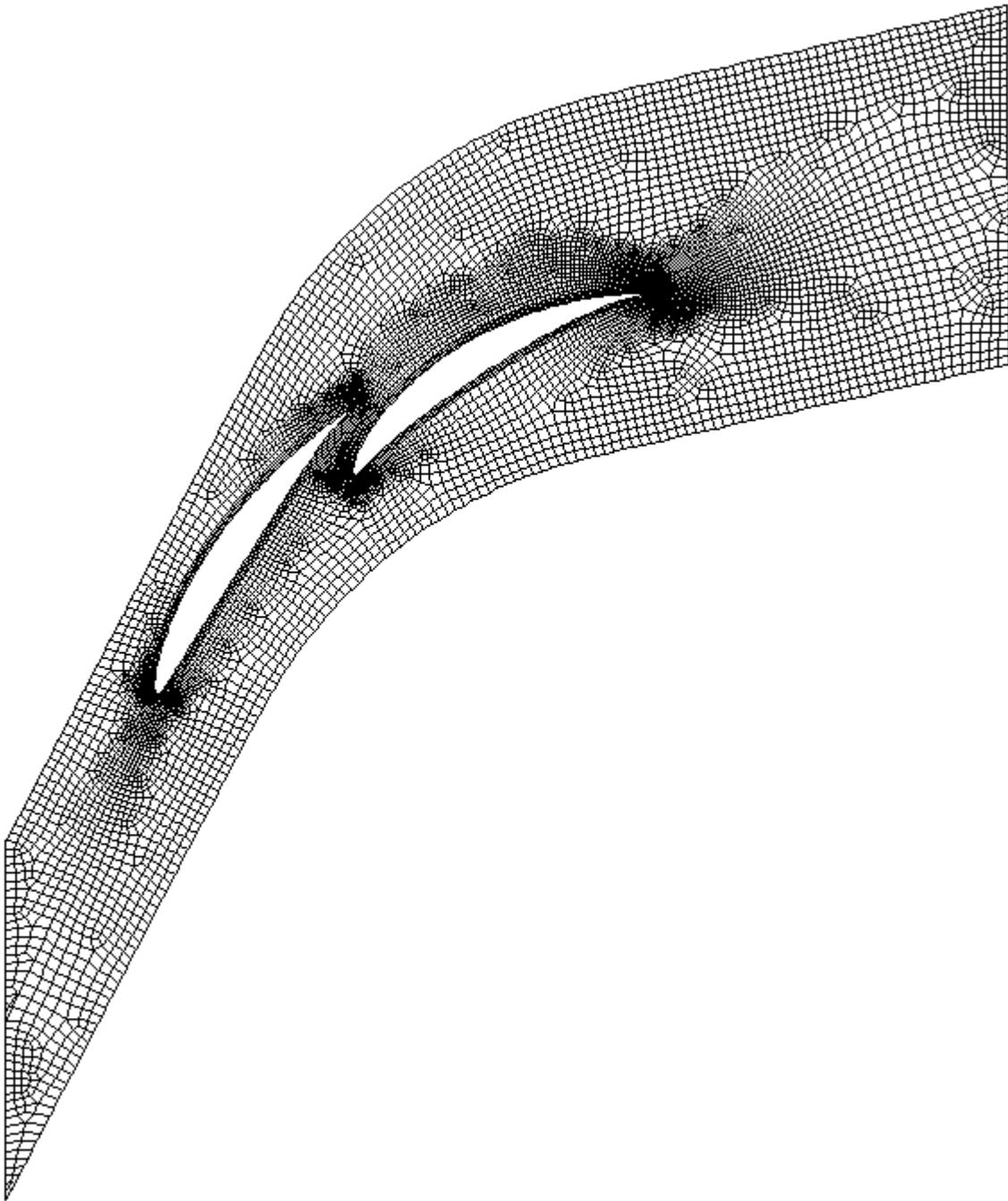


Figure 7-7: Tandem mesh. Tandem blade with $a = -0.025$ and $t = -0.2$

For all the models the solution for flow field and pressure distribution is tested reducing the grid sizes until the grid independent solution to the problem is obtained. For the various tandem blade models, the grid density is higher in the interference zone between the blades and in the proximities of the leading and trailing edges. Figure 7-8 and Figure 7-9 show grid details of a tandem blade with $a=-0.025$ and $t=-0.2$.

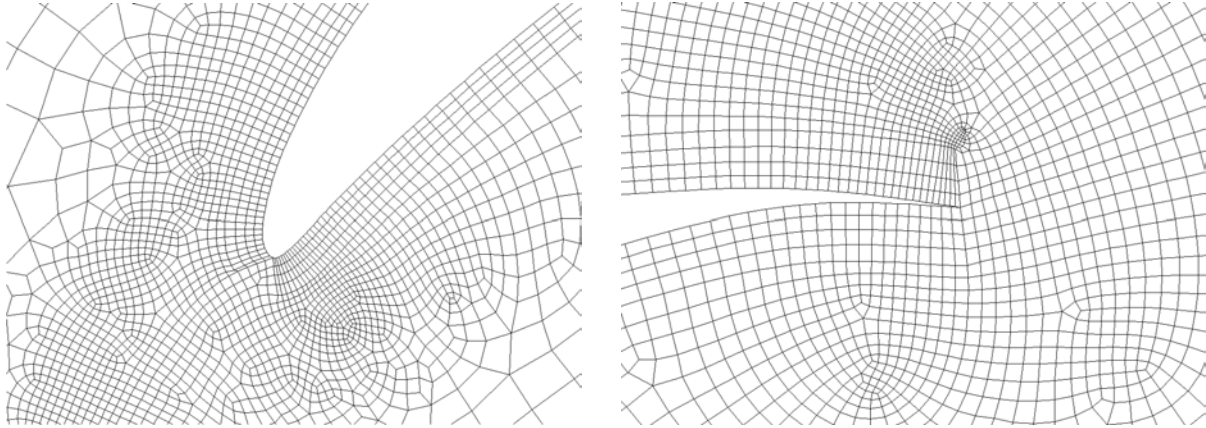


Figure 7-8: First profile LE and second profile TE detail for a tandem blade with $a=-0.025$ and $t=-0.2$.

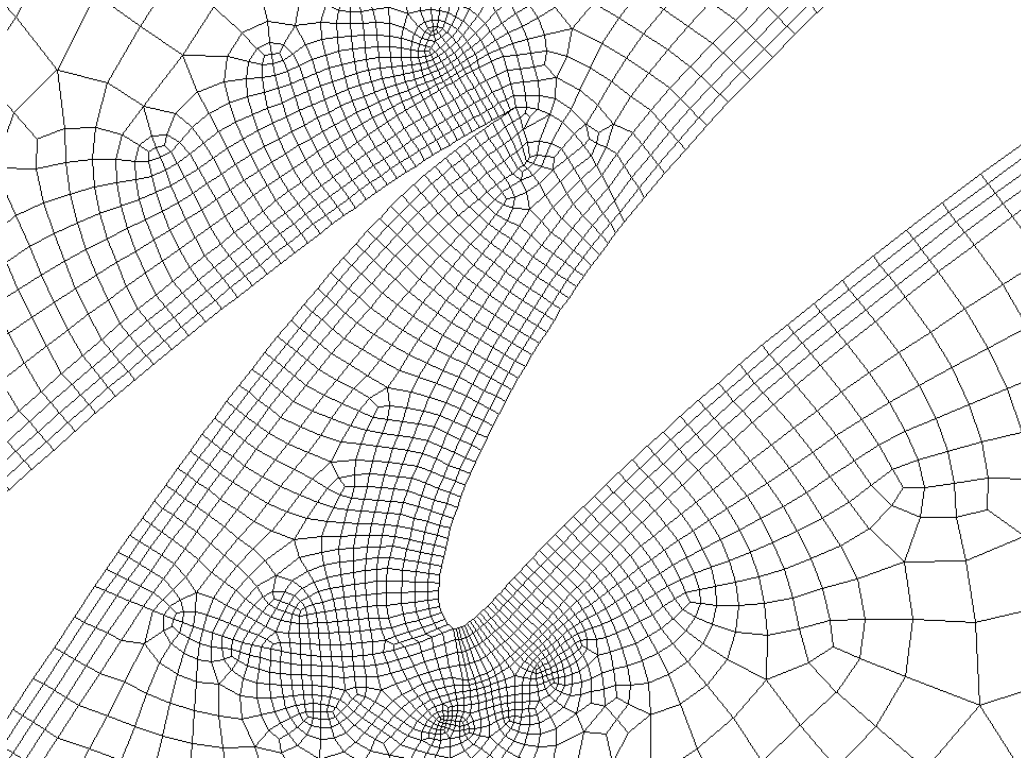


Figure 7-9: Grid detail for a tandem blade with $a=-0.025$ and $t=-0.2$

As said in chapter 5 the log law of the wall is expected in the vicinity of the walls. Therefore, the parameter y^* is set higher than 11.225 in the nearest cell to the wall in all the simulations.

7.3.2 No gap nozzle effect between the blades

Geometry configuration

When the second profile of a tandem blade is positioned in the “no gap nozzle effect” area (Figure 7-6), the interaction between the two blades is only evident in terms that the wake of the front profile affects the flow behavior along the arrangement.

To characterize the influence of the second blade position, four tandem blades are tested. Table 7-5 presents the geometrical parameters of the blades and the main characteristics of each configuration.

Axial displacement [-]	Tangential displacement [-]	Comments
0.2	-0.1	<ul style="list-style-type: none"> - No gap nozzle effects between the blades. - The second blade is positioned in the viscous free region of the first profile.
0.2	0	
0.2	0.2	<ul style="list-style-type: none"> - No gap nozzle effects between the blades. - The second blade is positioned in the wake of the first profile.
0.2	0.25	

Table 7-5: No gap nozzle effect. Representative tandem blades

The axial displacement for all the blades is set to 20% of the chord of the front profile. The tangential displacement is chosen as a function of the velocity field of the front blade. Figure 7-10 shows the velocity distribution of the front blade at an axial distance of 0.2 and a specification of the tangential displacement for each tandem blade tested.

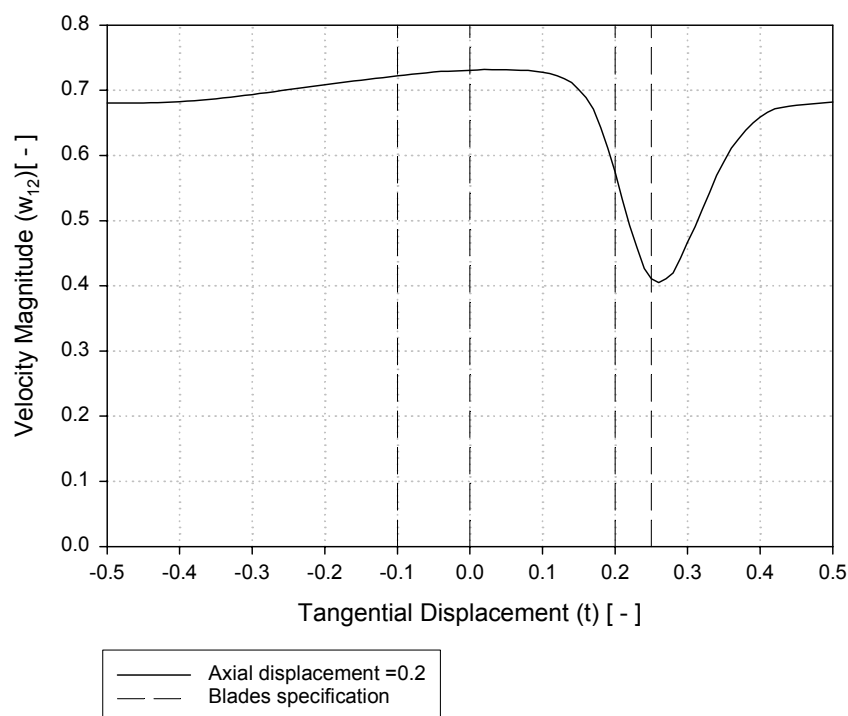


Figure 7-10: Velocity field front blade. Tandem blade no gap nozzle effects

Results and discussion

In this section the influence of the relative blade position when there is no gap nozzle effect is discussed. The comparison between the results obtained and the corresponding tandem blade with $a=\infty$ will lead to identify the main characteristics of the tandem configurations. Static pressure distribution, mass weighted loss coefficient and mass weighted deflection angle are the bases of the study.

Static pressure coefficient

Figure 7-11, Figure 7-12 and Figure 7-13 show the static pressure coefficient for three of the tandem blades. The blade with $a=0.2$ and $t=0.25$ is not characterized numerically because the model did not converge due to massive flow separation on the suction surface of the rear blade.

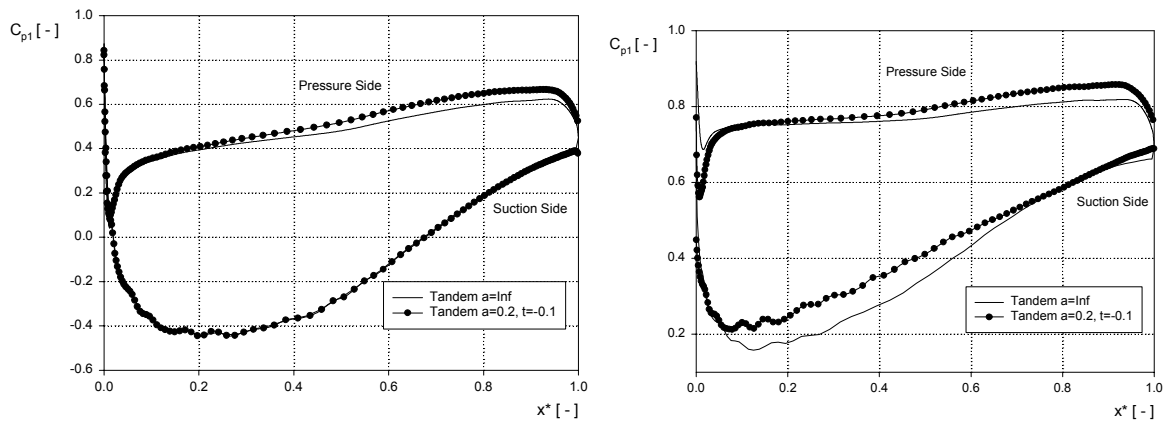


Figure 7-11: Pressure Coefficient tandem blade $a=0.2$, $t=-0.1$

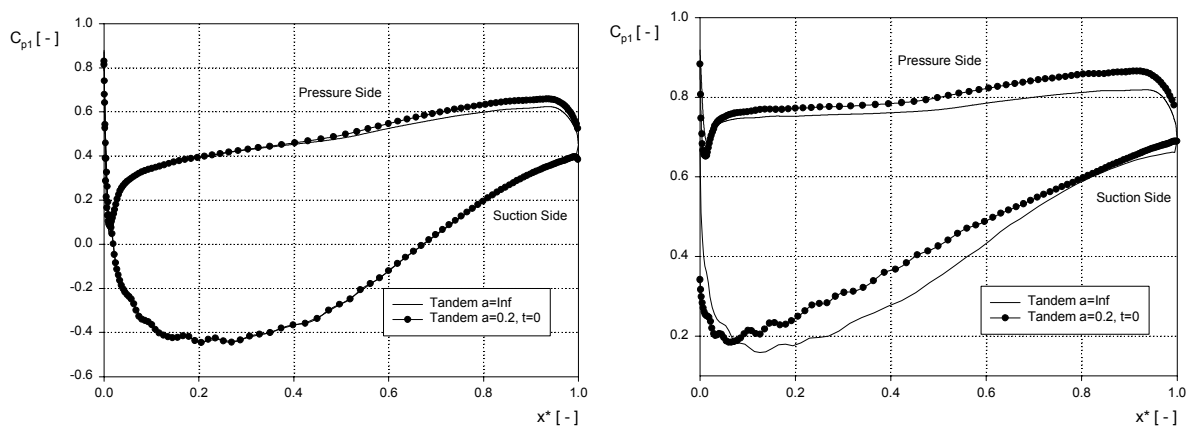


Figure 7-12: Pressure Coefficient tandem blade $a=0.2$, $t=0$

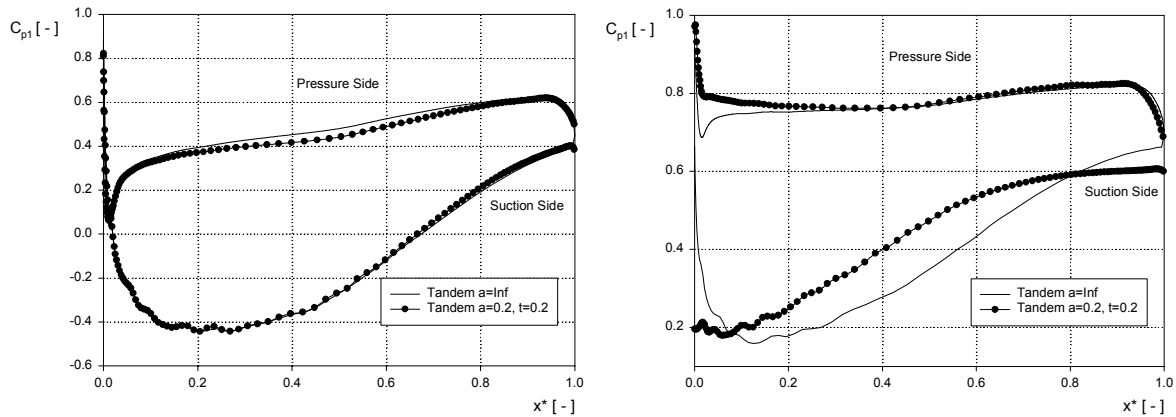


Figure 7-13: Pressure Coefficient tandem blade $a=0.2$, $t=0.2$

All the models showed that the flow behaviour along the suction surface of the first profile is not affected by the relative position of the rear blade. This characteristic is explained as a consequence of the no interaction between the blades in this surface.

The simulations of the tandem blades with the rear profile located in the viscous free zone showed that the flow along the pressure surface of the front profile is slightly more decelerated than the corresponding tandem blade with high axial displacement ($a=\text{inf}$). This is due to the presence of the second profile in the proximities of the trailing edge of the front blade.

The pressure distribution along the second profile shows that the maximum pressure difference is shifted toward the leading edge of the blade. That means that the flow incidence of the rear profile is higher than the tandem blade with $a=\text{inf}$ (this phenomenon is expected to increase for lower values of axial displacements and to decrease for higher values). Although the incidence is higher, the maximum pressure difference does not vary respect to the blade with high axial displacement. This is a consequence of the interaction between of the wake of the first profile and the velocity field in the vicinity of the suction surface of the rear blade. This phenomenon is illustrated with the velocity contours of a tandem blade with $a=0.2$ and $t=0$ in Figure 7-14.

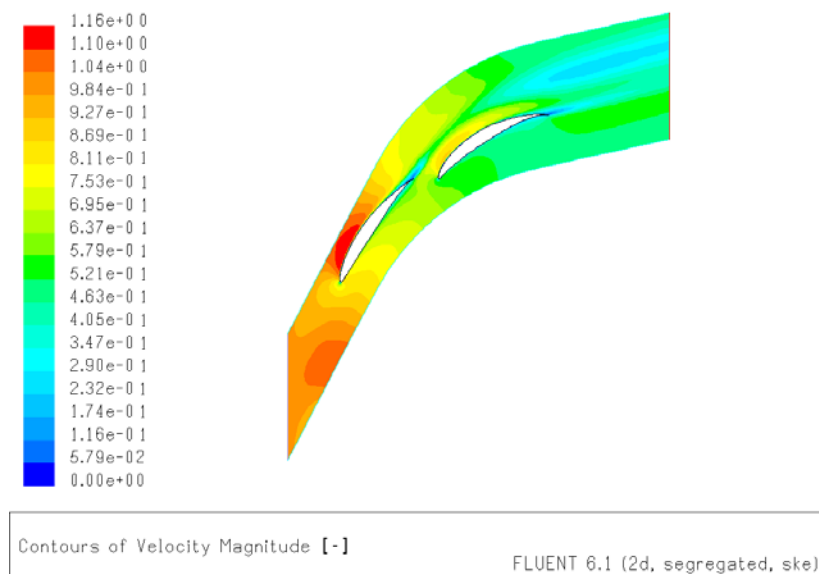


Figure 7-14: Velocity contours. Tandem blade with $a=0.2$ and $t=0$

Figure 7-11 and Figure 7-12 indicate that the flow separation tendency in the rear profile was avoided in the blades where the profile is positioned in the viscous free region. This is attributed to a higher inlet velocity in the rear blade due to its relative axial position (Figure 7-10 shows that w_{12} is approximately 0.71 for the blades tested and Table 7-3 reports an inlet velocity equal to 0.674 for the blade with $a=\infty$).

Figure 7-13 shows that massive flow separation on the suction surface of the rear blade occurs when the second profile is positioned in the wake of the front blade. The reason of the flow separation is the low flow momentum (produced by the velocity deficit in the wake region) at the leading edge of the rear blade (Figure 7-10). The velocity contours and velocity vectors for a tandem blade $a=0.2$ and $t=0.2$ are presented in Figure 7-15 and Figure 7-16. In both figures it can be seen the separation at the rear blade suction surface.

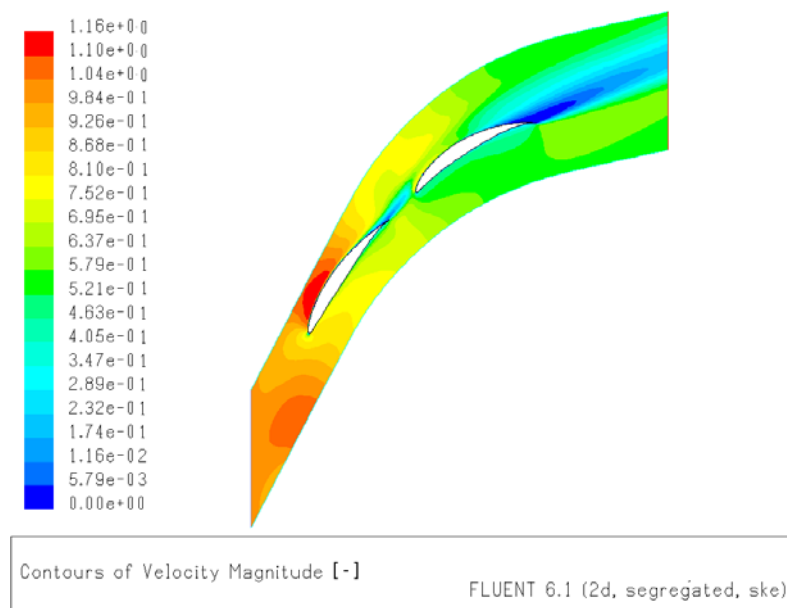


Figure 7-15: Velocity contours. Rear profile tandem blade with $a=0.2$ and $t=0.2$

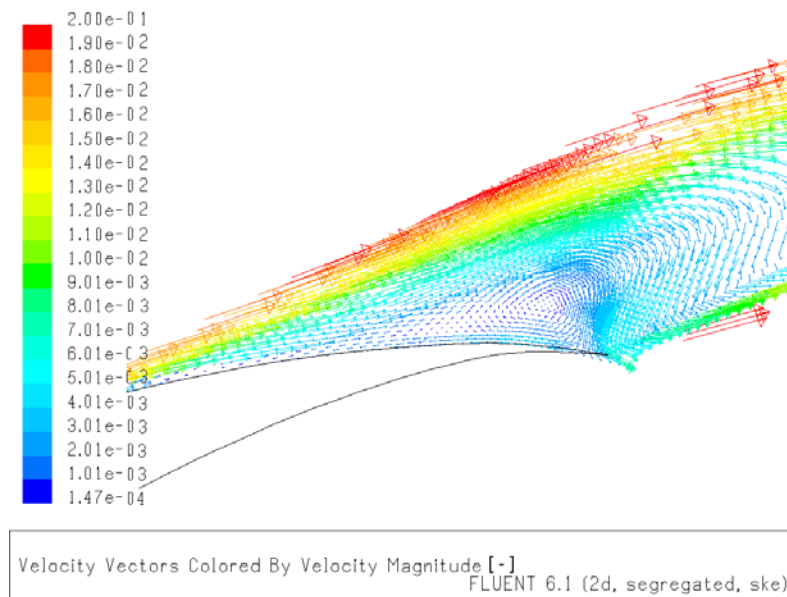


Figure 7-16: Velocity Vectors. Rear profile tandem blade with $a=0.2$ and $t=0.2$

Mass weighted average loss coefficient

The mass average loss coefficient is presented in Figure 7-17 as a comparison with the loss coefficient calculated for a tandem blade with high axial displacement. The results corresponding to the blade with $a=0.2$ and $t=0.25$ are not reported because the model did not converge. Thus, the dash line in the plot represents the tendency of the losses estimated for that blade.

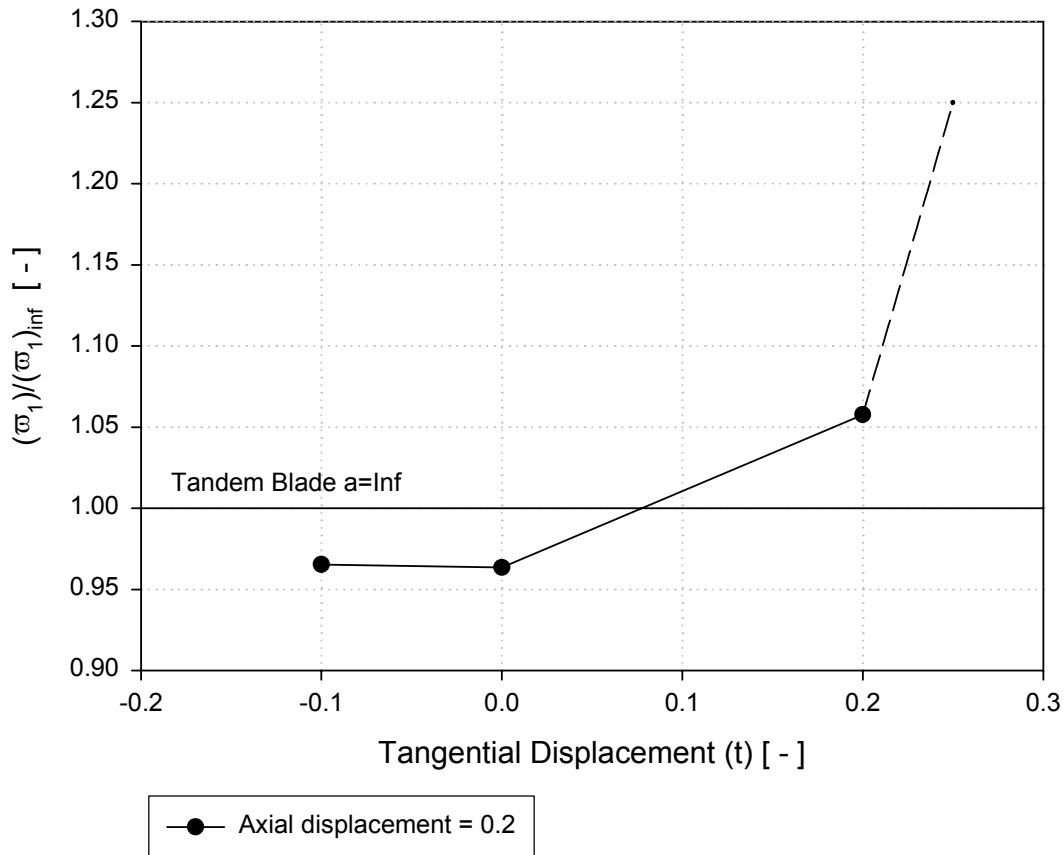


Figure 7-17: Mass average loss coefficient. Tandem blades (no gap nozzle effect)

From the above plot the following conclusions are extracted referring the flow behavior along the tandem blades tested:

- When the second profile is positioned in the wake of the front blade an increment in the total losses of the arrangement is evident. This is due to the flow separation on the suction surface of the rear blade as a result of the low inlet velocity w_{12} .
- When the second profile is located in the viscous free region of the front blade, the losses are 4% lower than the losses reported for the tandem blade with high axial displacement. This decrement occurs because the separation tendency presented in the tandem blades with $a = \infty$ does not occur in the two tandem blades of the plot.

Mass weighted average deflection angle

The results obtained for the deflection angle are given in Figure 7-18. The dashed line corresponds to the estimated tendency due to the no convergence of the last model.

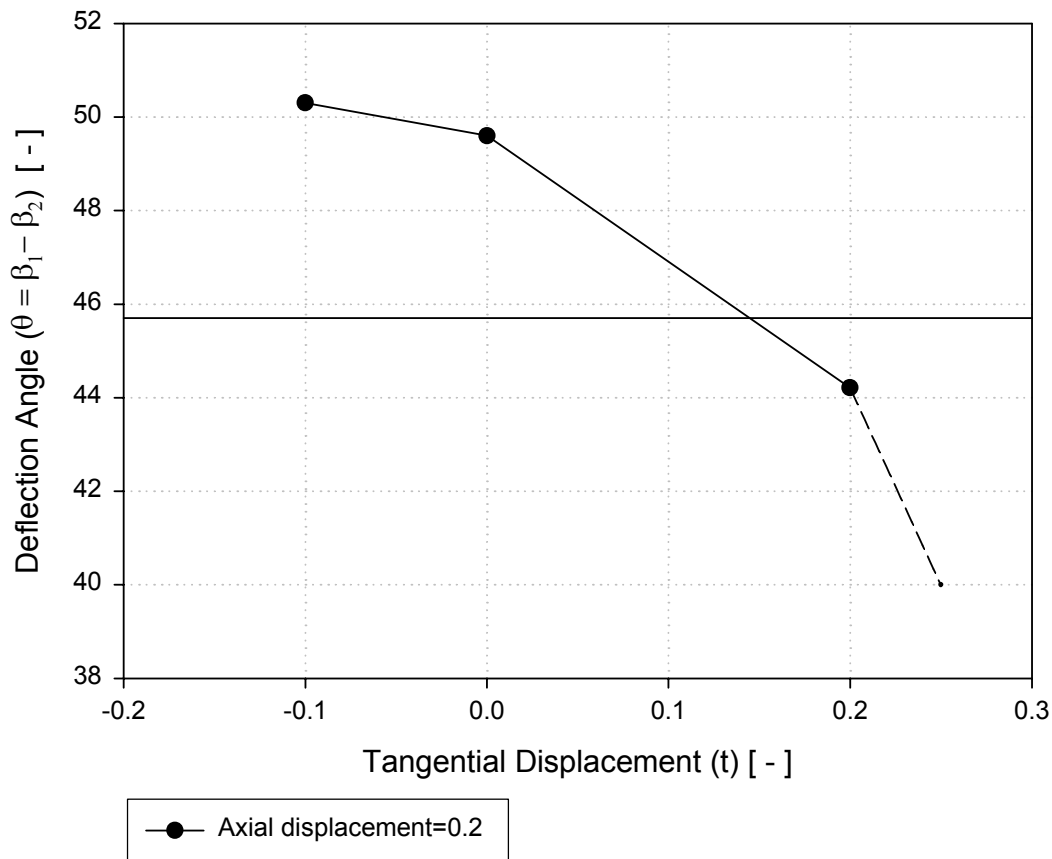


Figure 7-18: Mass weighted deflection angle. Tandem blade (no gap nozzle effects)

An extra deflection of approximately 4° was obtained in the tandem blades with the second profile positioned in the viscous free zone. This increment is attributed to the no presence of flow separation in the last part of the rear blade.

The tandem blades with the second profile located in the wake of the front profile showed a decrement in the deflection angle. This characteristic is due to the massive flow separation on the rear blade.

7.3.3 Gap nozzle effects

Geometry Configuration

The gap nozzle effects appear in the tandem blades when the rear profile is positioned in the vicinity of the trailing edge of the front blade. The zone between the blades can be represented as a convergent gap with an inlet and outlet area characterized by the distances $F1$ and $F2$ respectively (Figure 2-2). Therefore, the relation $F1/F2$ gives a measure of the flow acceleration by the presence of the nozzle geometry. In this section the ratio $F1/F2$ is used as a characteristic parameter for each tandem blade tested.

Taking as a reference the area discretization of Figure 7-6, a range of four axial displacements that varies between 0 and -0.075 are used. Hence, the gap nozzle effect is expected in all the models. The axial distances are illustrated in Figure 7-19.

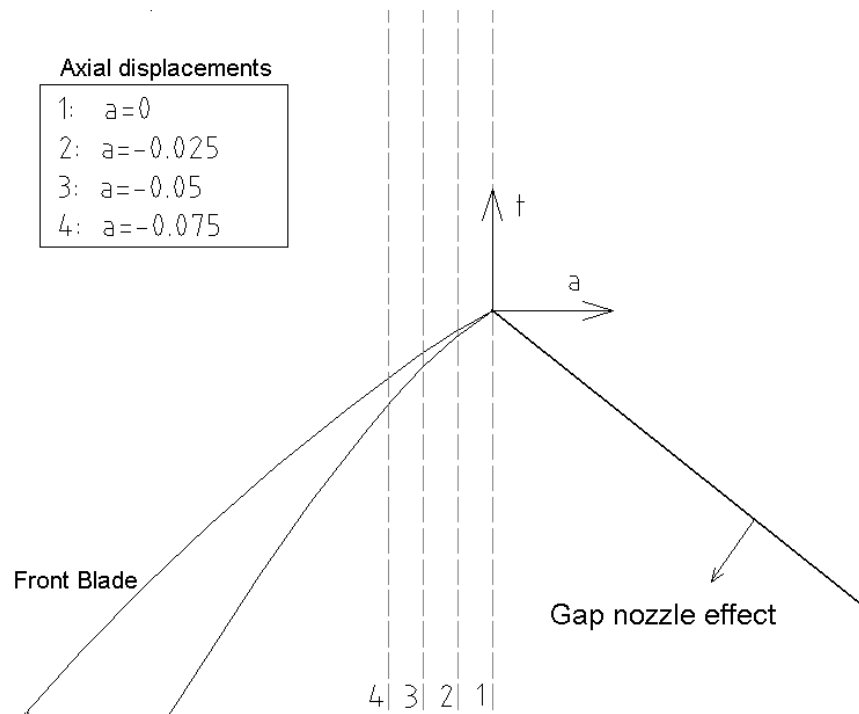


Figure 7-19: Second blade axial displacements. Gap nozzle effects

Bammert and Staude [2] suggest for tandem airfoils a ratio of $F1$ to $F2$ lower than 2 with the aim of avoiding an increment of the total losses. Nevertheless, in the present case $F1/F2$ will be varied from 1.5 to 3 with increments of 0.5 in order to investigate not only the optimum blade location but also to characterize the blockage phenomenon that causes the rise in the losses.

The tangential displacements that satisfy the condition fixed by the gap nozzle inlet and outlet ratio was calculated graphically using AUTOCAD V. 14. An example of the procedure is depicted in Figure 7-20 for a tandem blade with $F1/F2$ equal to 1.5 and axial distance of -0.025 . In the figure it is illustrated a value of $F1=0.169$ and $F2=0.111$, thus the ratio $F1/F2$ is approximately the expected quantity ($F1/F2=1.522$). Thereafter the tangential displacement is obtained as a function of $F1$, $F2$ and the blade axial distance.

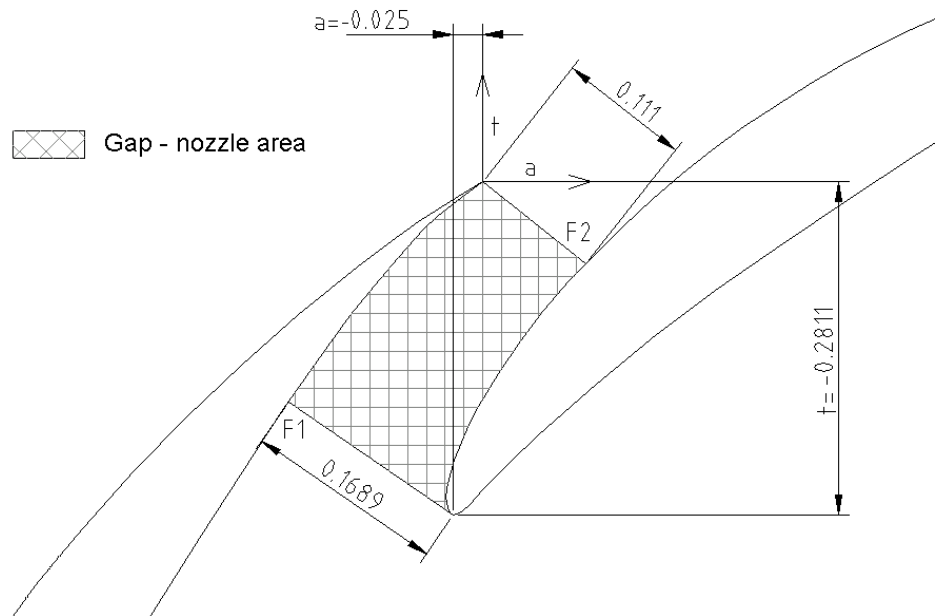


Figure 7-20: Gap nozzle parameters. Tandem blade with $F1/F2=1.5$ and $a=-0.025$

The blade chord portion affected by the nozzle zone for each profile is used to describe the effects of the nozzle geometry in the flow along the tandem cascades. For example, Figure 7-21 shows a geometrical representation of the gap nozzle channel for a blade with $F1/F2=1.5$ and axial displacement of -0.025 . In the figure it is illustrated the gap channel influence limit as a portion of the chord of each profile. Thus, the gap covers the 24.6% of the pressure surface in the rear part of the first blade, and the 20.3% of the suction surface in the front part of the second blade.

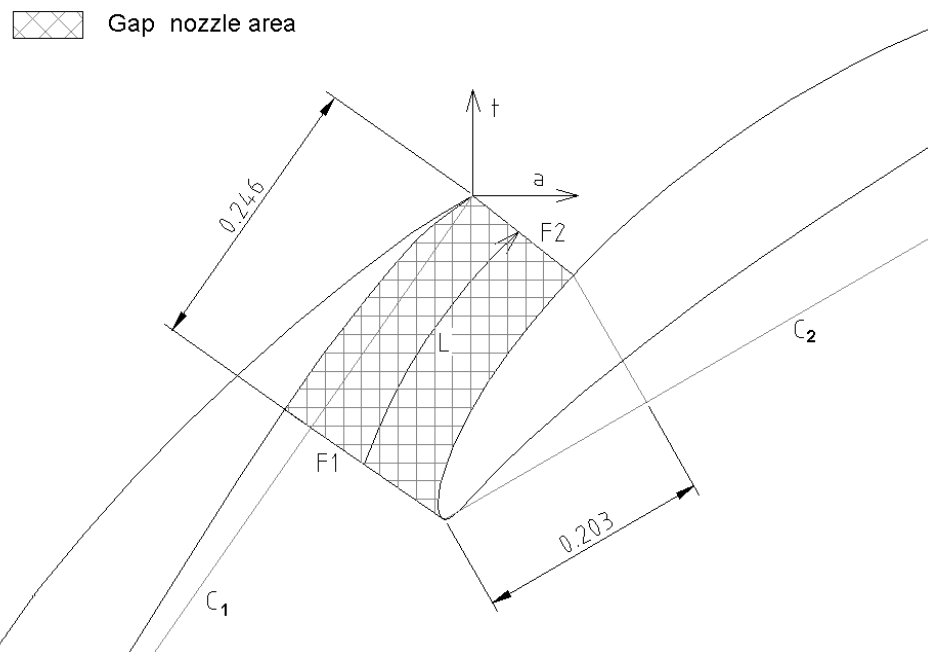


Figure 7-21: Gap channel influence limit. Tandem blade with $F1/F2=1.5$ and $a=-0.025$

The final gap-nozzle parameters that describe the area between the profiles are summarized in Table 7-6 for the various blades tested.

Axial displacement [-]	F1/F2 [-]	Tangential displacement [-] (Figure 7-20)	Gap channel influence limit (Figure 7-21)	
			% Chord front blade	% Chord rear blade
$a = 0.000$	1.5	-0.260	21.2	17.2
	2.0	-0.175	13.5	11.0
	2.5	-0.132	9.9	8.1
	3.0	-0.112	8.7	6.7
$a = -0.025$	1.5	-0.281	24.6	20.3
	2.0	-0.208	18.2	14.8
	2.5	-0.177	15.4	12.6
	3.0	-0.157	13.7	11.2
$a = -0.050$	1.5	-0.300	27.7	23.2
	2.0	-0.230	21.7	17.9
	2.5	-0.206	19.6	16.2
	3.0	-0.190	18.2	15.0
$a = -0.075$	1.5	-0.314	30.4	25.9
	2.0	-0.259	25.7	21.6
	2.5	-0.229	23.1	19.4
	3.0	-0.217	22.1	18.5

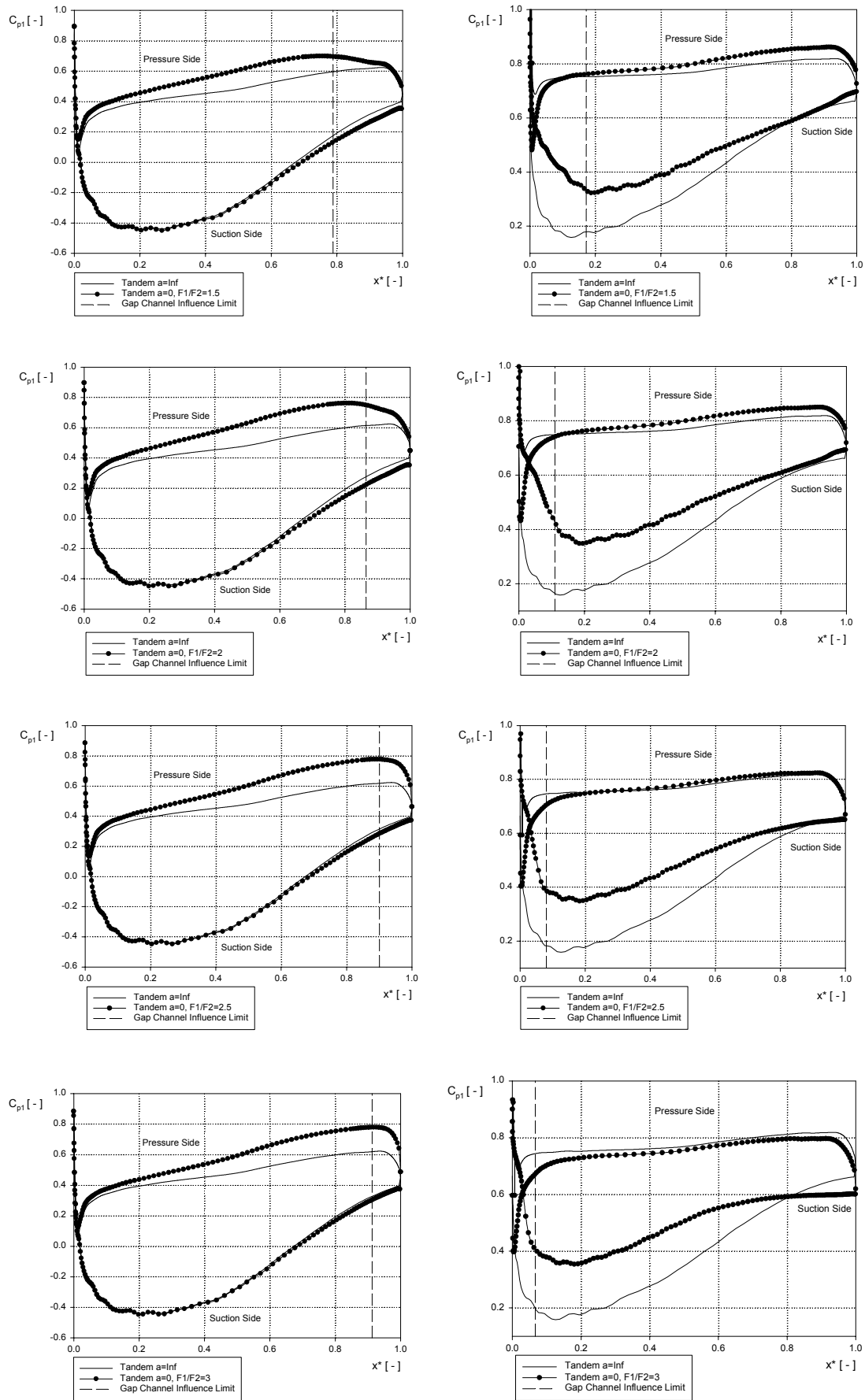
Table 7-6: Final blade parameters. Gap nozzle effect tandem blades

Results and Discussion

This part of the investigation has been conducted to assess the advantage of a tandem cascade with the presence of a gap nozzle geometry between the blades as opposed to the two single blades acting independently. The study is made on the bases of the static pressure distribution along the blades, the mass weighted loss coefficient and the mass weighted deflection angle at one chord downstream.

Static Pressure Coefficient

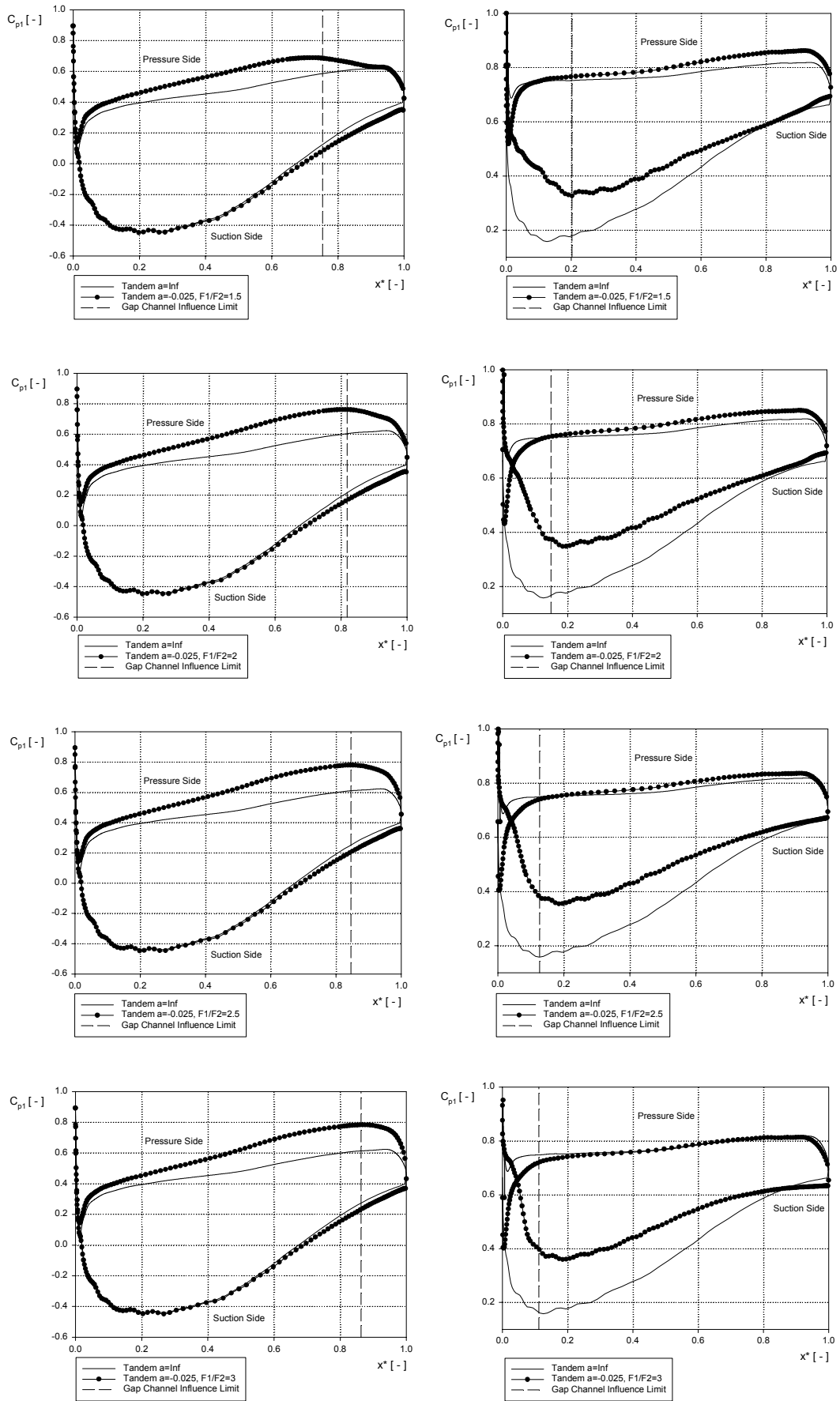
Blade surface pressure distribution of the tandem blades with axial displacements between $a = 0$ and $a = -0.075$ at various F1/F2 ratios are presented in Figure 7-22, Figure 7-23, Figure 7-24 and Figure 7-25. In all figures there is the comparison between the two blades that conform the tandem arrangement and the corresponding single blade acting independently. There is also a specification of the gap nozzle channel limit for each blade.



Front blade

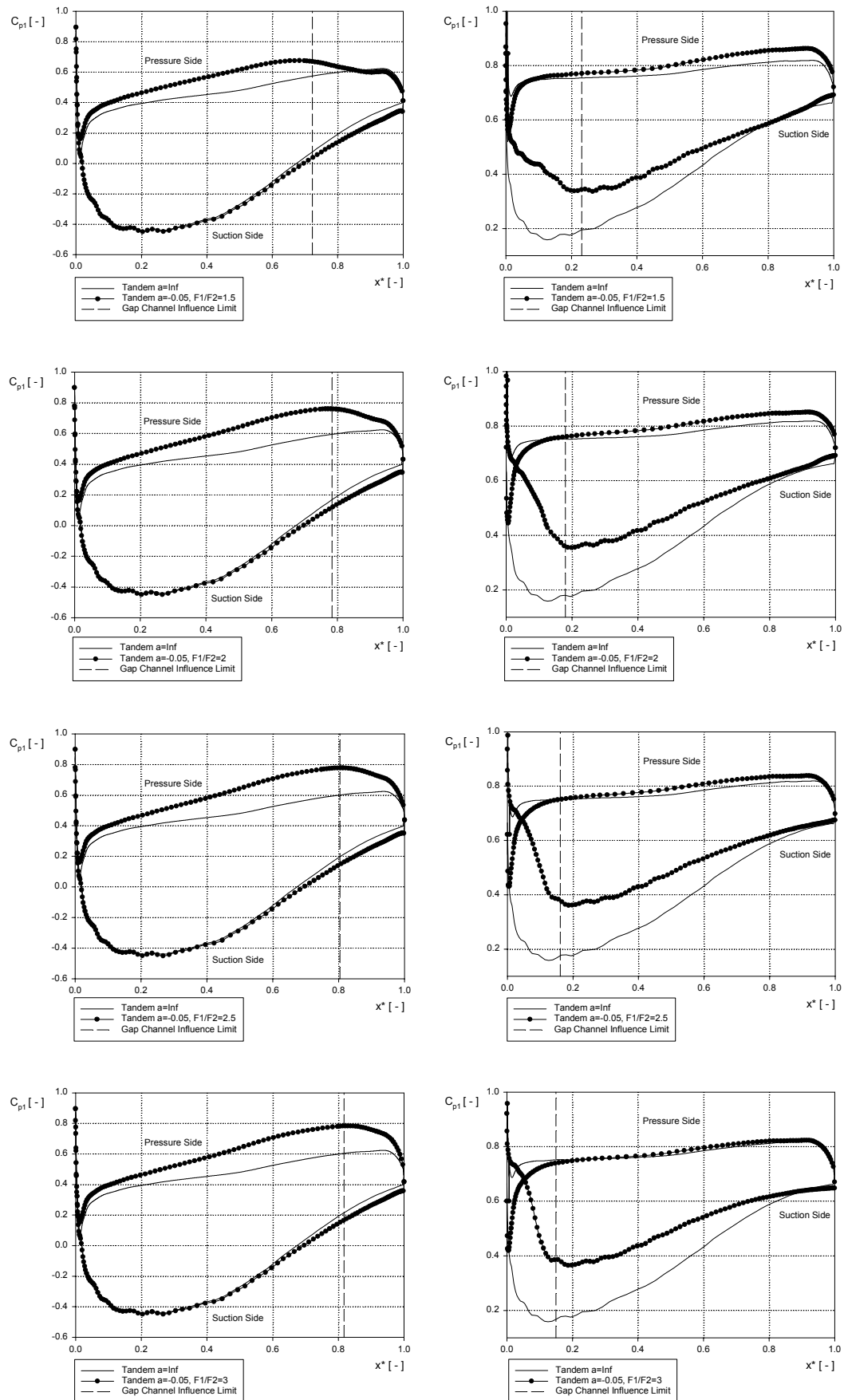
Rear blade

Figure 7-22: Pressure coefficient. Tandem blades $a=0$.



Front blade Rear blade

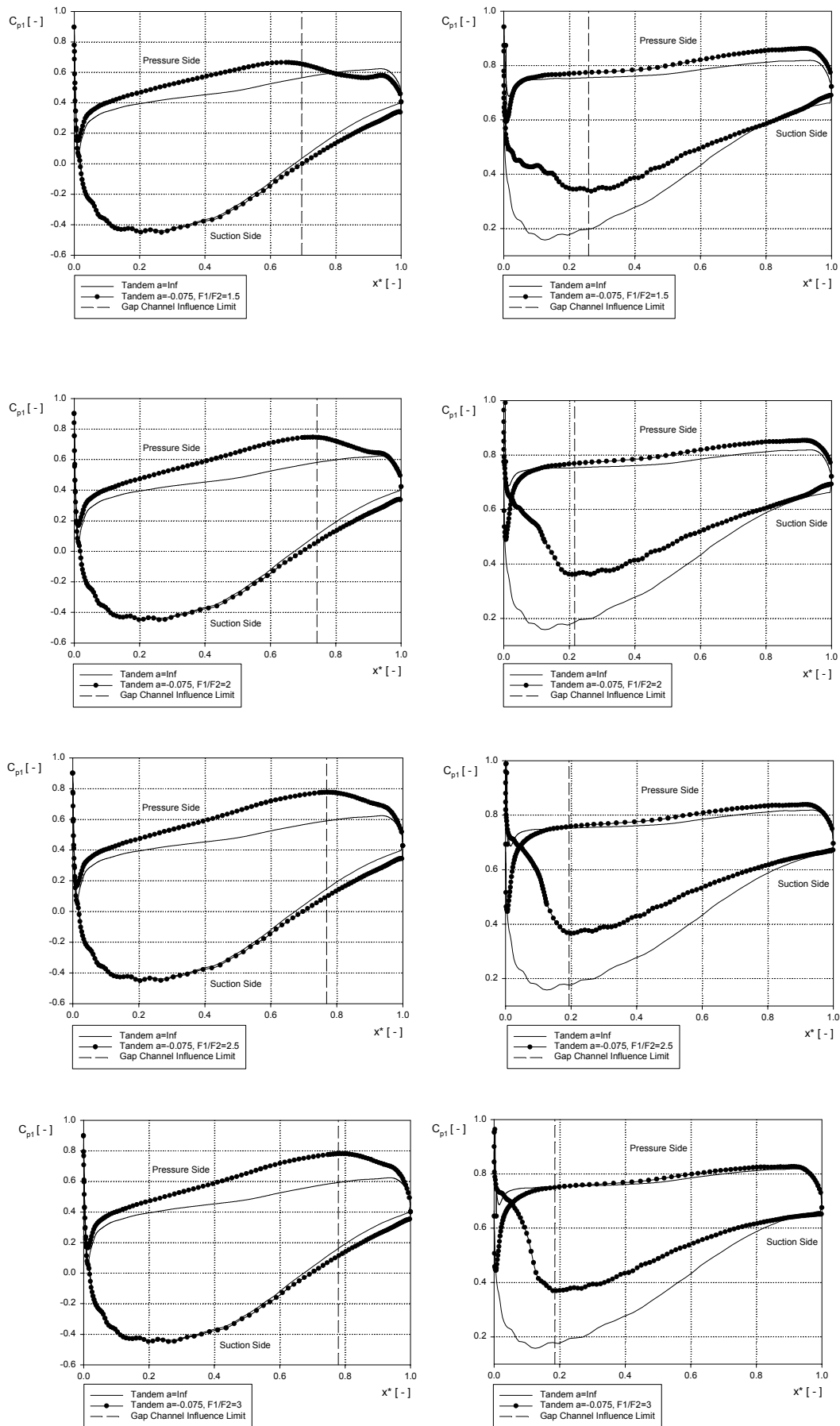
Figure 7-23: Pressure coefficient. Tandem blades $a = -0.025$.



Front blade

Rear blade

Figure 7-24: Pressure coefficient. Tandem blades $a=-0.05$.



Front blade

Rear blade

Figure 7-25: Pressure coefficient. Tandem blades $a=-0.075$.

Front blade discussion: In the tandem blades tested it was noticed that the relative position of the second profile does almost not disturb the flow along the suction surface of the front blade. This characteristic was expected because the interaction between both blades is inexistent in this surface. Thus, the flow behavior is quite similar to the flow along the blade acting independently (an initial acceleration up to 30% of the chord from the front blade leading edge, then the flow starts diffusing constantly toward the trailing edge). Nevertheless, it was appreciable that if the tangential displacement of the second blade is quite large (that means low values of $F1/F2$ ratio) the flow is slightly more accelerated than the corresponding flow on the suction surface of a tandem blade with $a=\infty$. This fact is attributed to a mass flow balance between the gap nozzle area (where the flow has low momentum) and the flow channel between two consecutive tandem blades.

On the pressure surface of the front blade it is evident that the flow is highly influenced by the gap nozzle area. This influence is presented as a blockage effect that causes a lower flow velocity in the proximities of the front blade trailing edge pressure surface. Figure 7-26 illustrates a comparison between various $F1/F2$ ratios for the front profile of a tandem blade with $a=-0.025$.

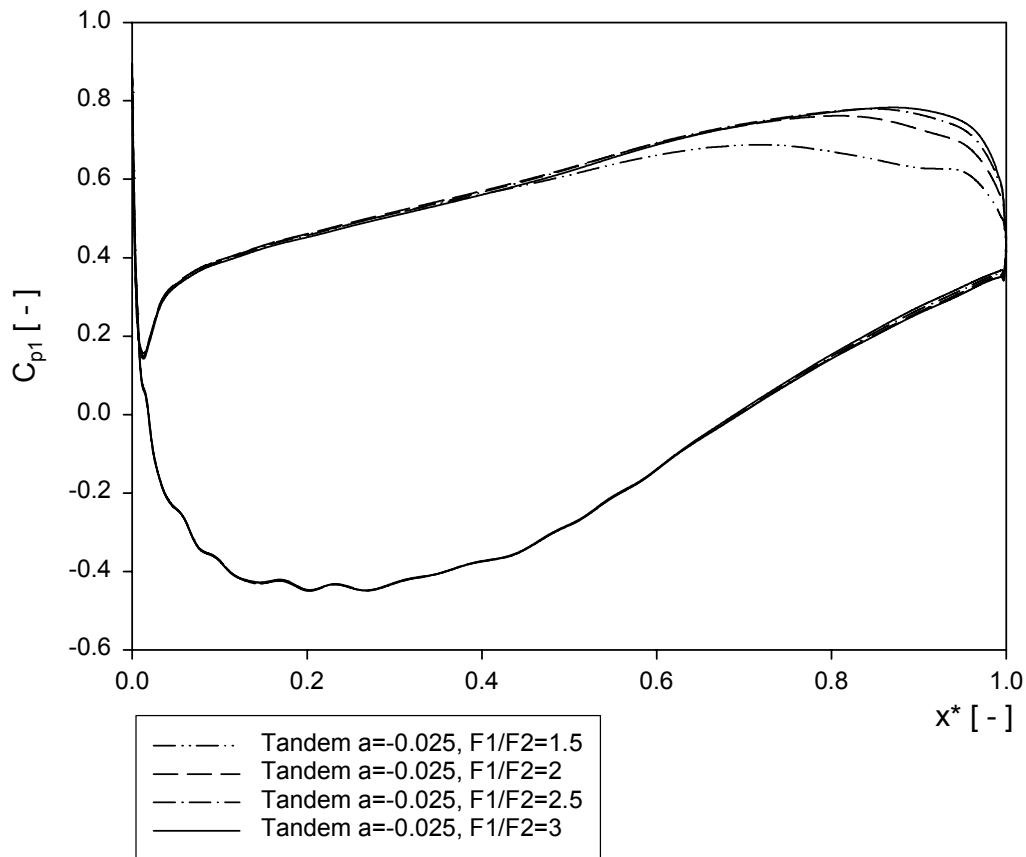


Figure 7-26: Pressure coefficient front profile. Tandem blade $a=-0.025$

Figure 7-26 shows that the lowest velocity in the pressure surface occurs when the ratio $F1/F2$ is the highest. It is also appreciable that when the ratio $F1/F2$ increases there is also an increment in the blockage effect. The flow behavior in this surface shows a constant deceleration up to the gap channel limit. Thereafter, the flow enters into the gap nozzle area and the velocity increases toward the trailing edge of the profile. This characteristic is due to the nozzle effect in the gap zone.

When the second blade is positioned in such a way that the gap channel influence area covers more than the 20% of the chord of the front profile it is appreciable that the flow acceleration in the gap nozzle is not constant. This flow pattern can be seen clearly in many of the figures but is particularly evident in the tandem blade with $a=-0.075$ and $F1/F2=1.5$ (Figure 7-25). This characteristic is attributed to the fact that for these locations the gap area has not the form of a single nozzle but a nozzle-diffuser (Figure 7-27).

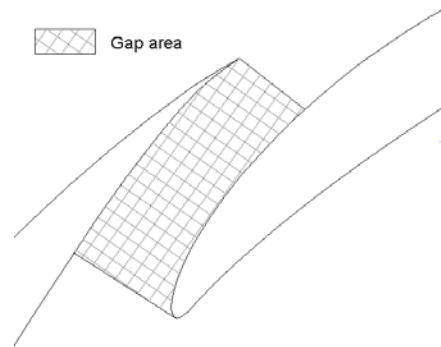


Figure 7-27: Convergent-divergent gap. Tandem blade $a=-0.075$, $F1/F2=1.5$

The comparison between the computational results of the front blade and the experimental data reported by Bammert and Staude in Figure 2-4 shows that the numerical method predicts quite good the flow characteristics along the blade. Thus, Figure 7.26 shows the same flow behaviour as the measurements.

Rear blade discussion: The pressure surface static pressure distribution of the second blade shows that for large tangential displacements (low values of $F1/F2$) the inlet incidence angle of the profile is higher compared with the corresponding tandem blade with $a=\text{inf}$. This phenomenon is attributed to the fact that the flow is not still totally deflected by the front profile. Therefore, it is expected an increment in the incidence of the rear blade proportional to the relative axial distance. Figure 7-28 shows the path flow for a tandem blade with $a=-0.05$ and $F1/F2=1.5$. In the figure it is evident that the inlet angle (β_{12}) is higher than the design inlet angle calculated with the velocity field of the front profile one chord downstream in a tandem blade with $a=\text{inf}$.

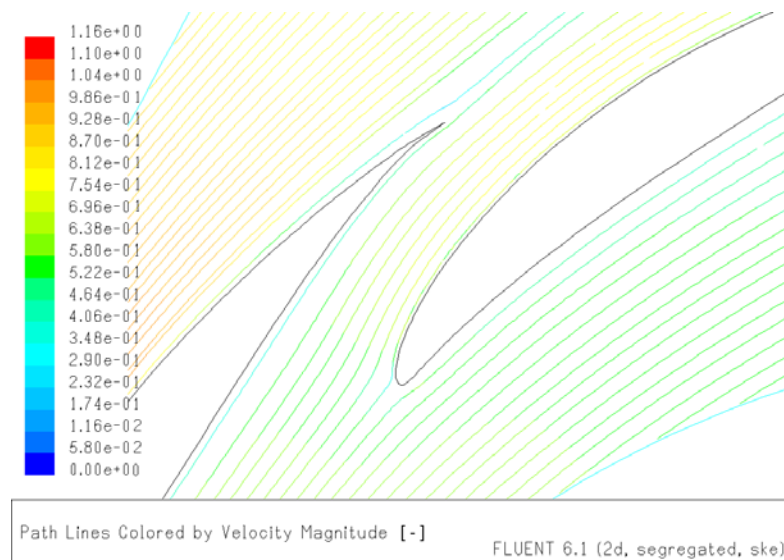


Figure 7-28: Path flow lines. Tandem blade with $a=-0.05$ and $F1/F2=1.5$

For high values of $F1/F2$ the flow is forced to go along the pressure surface of the second blade due to the blockage phenomenon in the gap nozzle area. Thus, the incidence angle of the second profile decreases and the momentum transfer on the rear blade suction surface is not sufficient to ensure the no presence of flow disturbances. This characteristic is illustrated in Figure 7-29 with the path lines of a tandem blade with $a=-0.05$ and $F1/F2=3$.

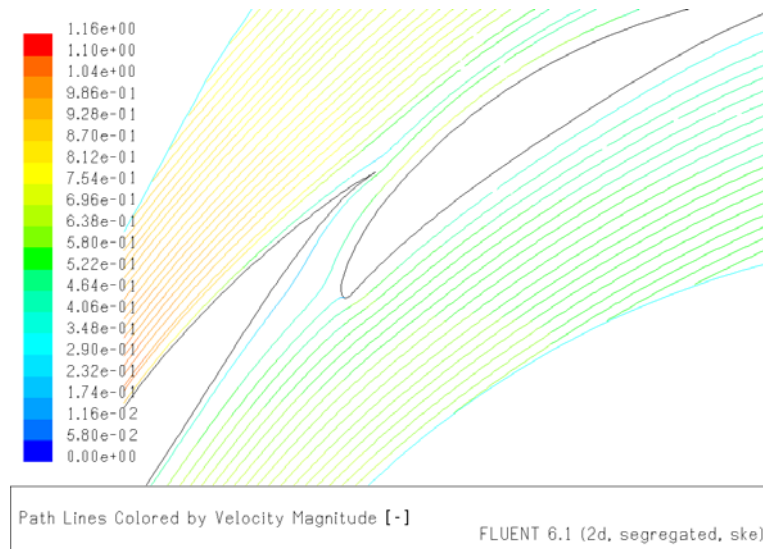


Figure 7-29: Path flow lines. Tandem blade with $a=-0.05$ and $F1/F2=3$

The flow along the rear blade suction surface presents high differences respect the corresponding blade acting independently. All the pressure distribution plots show that the gap nozzle geometry avoids high flow acceleration at the suction surface of the rear profile. Therefore, it is said that the peak velocity of the second blade is influenced by the relative position of the blades in a tandem cascade. In all the models the flow is characterized by an initial acceleration (limited by the nozzle geometry) up to the gap channel influence limit. Thereafter a constant deceleration toward the trailing edge is evident. Figure 7-30 shows a comparison between the rear blade of a tandem with $a=-0.025$ for different $F1/F2$ ratios.

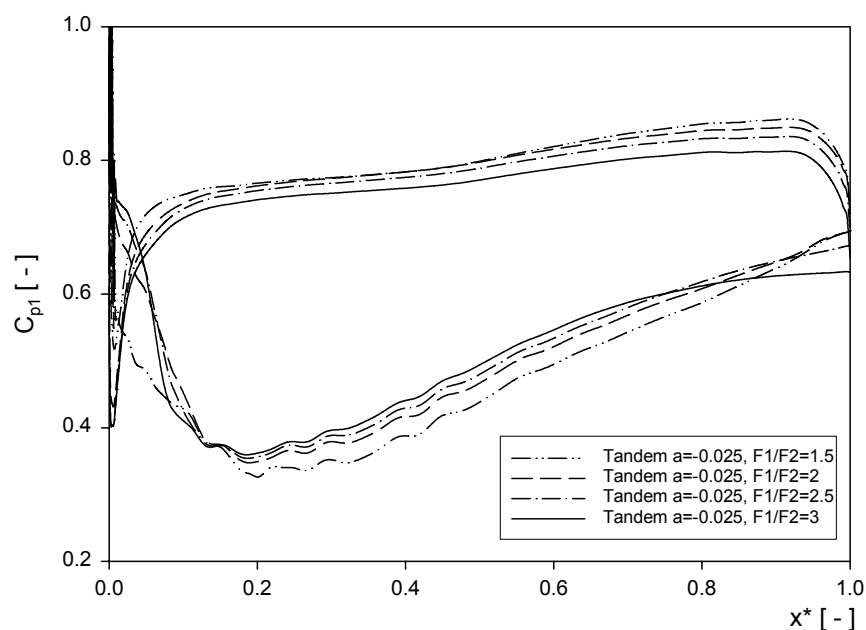
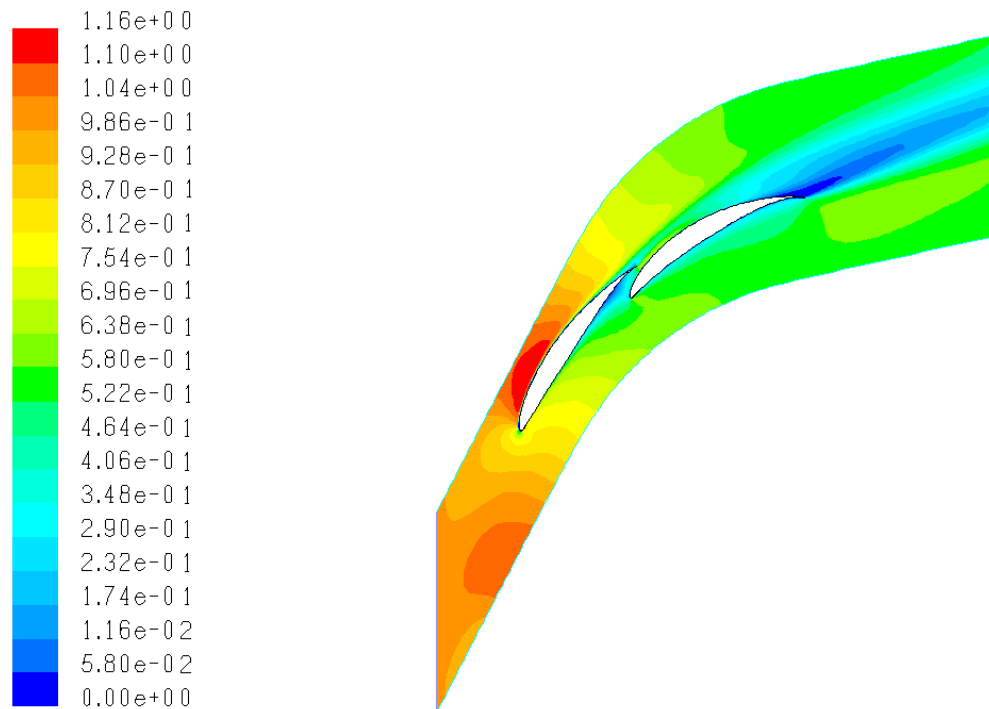


Figure 7-30: Pressure coefficient rear profile. Tandem blade $a=-0.025$

Figure 7-30 shows that the blockage effect (presented as a decrement of the flow peak velocity) increases for high values of $F1/F2$. It is also evident that the decrement in the velocity w_{12} causes a flow separation in the suction surface of the rear blade when the ratio $F1/F2$ is higher than 2.5. Thus, for the blade with $F1/F2$ equal to 3 the separation occurs near the 70 percent of the chord from the leading edge. This phenomenon is illustrated in Figure 7-31.



Contours of Velocity Magnitude [-]

FLUENT 6.1 (2d, segregated, ske)

Figure 7-31: Contours of velocity magnitude. Tandem blade $a=-0.025$, $F1/F2=3$

In the above figure the low momentum flow at the inlet of the gap zone (zero velocity contour) is responsible for the flow separation at the rear part of the second blade. Thus it is expected an increment of the total losses because the blade is working in stall conditions.

Bammert and Staude [2] conclude that the flow along the pressure surface of the rear profile is not affected by the relative position of the blade. This fact is true when the gap nozzle promotes sufficient momentum transfer in order not to create flow disturbances in this surface. But for high values of $F1/F2$ the computational results evidenced a separation tendency in the back tandem that was not mentioned in [2].

Mass Averaged Loss Coefficient

In this part of the investigation the mass averaged loss coefficient for each tandem blade is studied as a comparison of the loss coefficient calculated for the tandem blade with $a=\infty$. Figure 7-32 presents the mass averaged loss coefficient for all the tandem blades tested in terms of the ratio $F1/F2$ and Figure 7-33 shows the loss coefficient vs. the tangential position of the second blade.

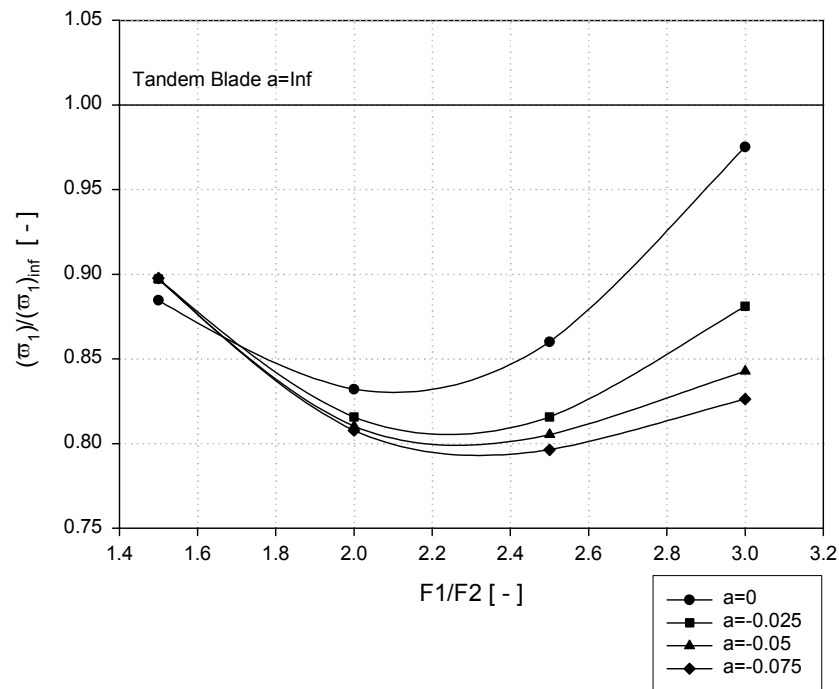


Figure 7-32: Mass average loss coefficient vs. $F1/F2$ ratio

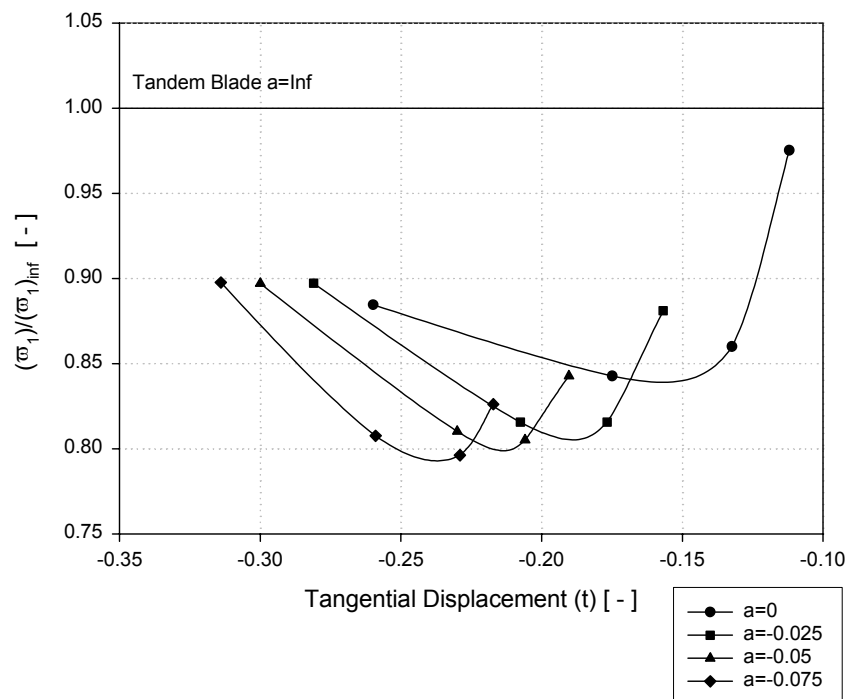


Figure 7-33: Mass average loss coefficient vs. tangential displacement

It is interesting that an appreciable decrease in the losses occurs when the ratio $F1/F2$ increases from 1.5 to 2 in all the models. The decrement is due to the interaction between the flow along the suction surface of the back tandem and the wake of the first profile. This characteristic can be seen clearly in the contours of loss coefficient in Figure 7-34 and Figure 7-35 for two tandem blades with the same axial displacement and different $F1/F2$ ratio.

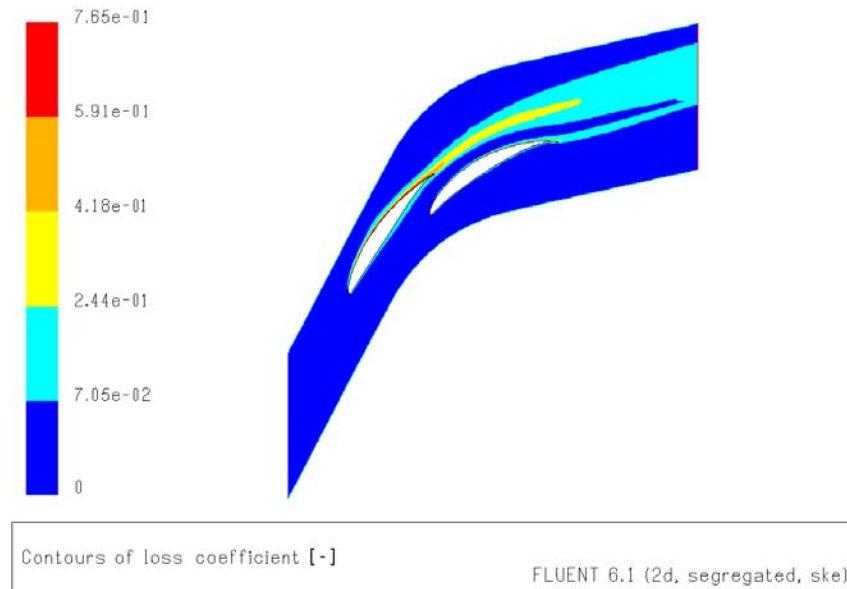


Figure 7-34: Contours of loss coefficient. Tandem blade with $a=-0.025$ and $F1/F2=1.5$

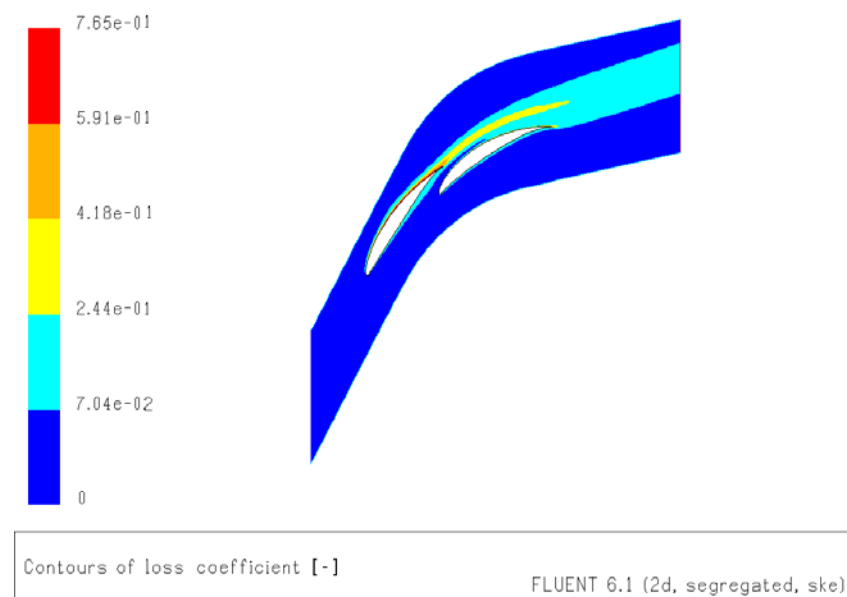


Figure 7-35: Contours of loss coefficient. Tandem blade with $a=-0.025$ and $F1/F2=2$

Figure 7-34 shows that for low tangential displacements (low values of $F1/F2$) the gap nozzle flow does not interact with the wake of the front profile. Therefore, the performance of the arrangement tends to be similar to the flow behavior along the blades acting separately. On the other hand, Figure 7-35 shows that if the back tandem is positioned in the optimum location the gap nozzle energizes the wake of the front profile and promotes sustained flow attachment on the suction surface of the rear blade (the wake having low momentum is filled up by the high momentum flow near the suction surface of the second profile).

For high values of $F1/F2$ (over 2.5) the gap nozzle geometry does not promote sufficient flow guidance for efficient momentum transfer on the suction surface of the rear blade. Therefore, massive flow separation occurs and the losses increase substantially.

It is shown that the total pressure loss of the tandem cascade differs from the total pressure loss obtained when the two blades of the tandem arrangement are tested separately. This difference is attributed to the interference between the two profiles. Thus is result very important to remark that a decrement of almost 20% is noticeable when the second blade is located in the optimum position.

Bammert and Staude [2] suggest that the ratio $F1/F2$ has to be lower than 2 in order to avoid an increase in the losses of the arrangement. The experimental results are supported with the computational data reported in Figure 7-32 and it is concluded that the numerical calculations are able to predict the flow characteristics along the gap nozzle geometry of a tandem blade. The surprising good agreement between the losses reported in Figure 2-6 and the predicted loss coefficient of Figure 7-33 proves that the used flow solver is a valid tool for analysis in tandem blades.

Mass Averaged Deflection Angle

Summary of the relationship between deflection angle and the relative position of the second profile in the tandem blade is given for each axial displacement in Figure 7-36.

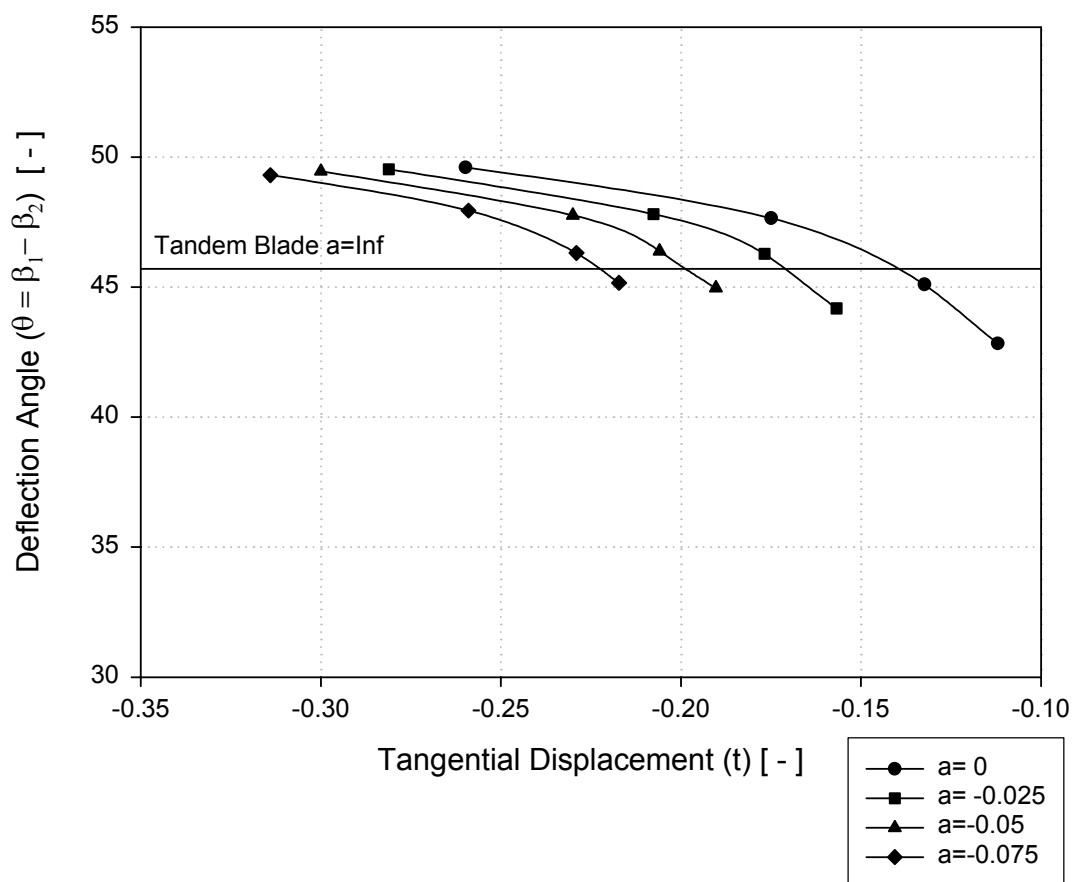


Figure 7-36: Mass average loss coefficient vs. tangential displacement

The results show that the deflection angle does not vary substantially between the tandem blades tested and the corresponding model with high axial displacement ($a=\infty$).

All the configurations showed that for equal values of $F1/F2$ the outlet angle almost not varies in terms of the axial displacement. Nevertheless, when the ratio $F1/F2$ increases, there is a decrement in the deflection angle. This trend is due to the separation tendency in the suction surface of the rear blade as a consequence of the blockage effect.

It is remarkable the fact that the tandem blades fulfill the requirement imposed in terms of flow deflection and a turning angle of approximately 46° was achieved without flow disturbances for almost all the configurations tested.

8 Conclusions

In the present investigation an attempt has been made to understand the flow behaviour along the two profiles that conform a tandem arrangement. The chosen tandem concept with a tandem blade conformed by two NACA65 profiles with 1:1 blade number ratio and the same chord length between both blades fulfill the design goal of 46° flow turning under 2D flow conditions. At the beginning, it could be thought to use a single blade to meet the required targets but the high flow deflection results in inconvenient due to the imminent flow separation on the suction surface of the blade. Thus, it is concluded that the deflection capabilities of tandem blades are higher compared with single profiles.

The interaction mechanism between both profiles was studied as a comparison with the results obtained for the two blades tested separately. Based in the literature overview and the computational data, the following conclusions can be drawn:

8.1 Profile selection

- The selection of the front profile should be done using the inlet flow parameters (w_1, β_1) and an estimated value for the blade loading (this value can be expressed in terms of flow deflection or flow deceleration). The technical literature recommends 50-50% loading split between both profiles.
- The selection of the rear blade should be done using the outlet flow parameters of the front profile (w_{12}, β_{12}) and the remained flow deflection and flow diffusion that satisfies the design targets. It is very important that the profile selection for both blades ensures the absence of flow disturbance along the blades.
- A narrow operational range characterizes tandem blades when the profiles are scaled down from a standard blade. This is a consequence of the low leading edge radius that causes limited flow guidance over the blades. Therefore, it is recommendable to use tandem blades conformed by scaled profiles only when the blades are supposed to work at design conditions.

8.2 Second blade location: no gap nozzle effect

- If the rear blade is located in the viscous free region and there are no gap nozzle effects between the profiles, the tandem arrangement can be treated as two isolated blades.
- If the rear blade is positioned in the wake of the front profile there is an increment in the losses as a consequence of the velocity deficit that causes flow disturbances on the suction surface of the back tandem (for low axial displacements flow separation occurs due to low values of w_{12}).

- It is concluded that tandem blades shows no advantages in terms of loss reduction when the rear tandem is located down stream (no gap nozzle effects) of the front profile. This is due to the fact that the interaction between both blades is reduced for these configurations.

8.3 Second blade location: gap nozzle effect

- An advantage in terms of total losses is appreciable when the second profile is positioned in the optimum location. A decrement of approximately 20% compared with the losses calculated for both blades acting independently was reported. This advantage occurs because the gap-nozzle energizes the wake of the front profile and promotes sustained flow attachment on the suction surface of the back tandem.
- The presence of the second blade in the proximities of the pressure surface of the front blade causes a decrement in the flow velocity. This decrement is characterized as a blockage effect that increases for high values of $F1/F2$ and decreases for low values.
- For high values of $F1/F2$, it was noticed a flow separation in the suction surface of the rear blade due to the low flow velocity caused by the blockage in the gap nozzle area.
- In all the models it was noticed that the gap nozzle geometry influences highly the peak velocity on the suction surface of the rear blade. It was also reported a similar flow behaviour in this surface characterized by an initial flow acceleration up to the gap channel limit. Therefore, it is concluded that the chord portion affected by the gap nozzle geometry in the rear blade should be always lower than the chord distance correspondent to the maximum pressure difference of the blade. This fact can be used as a guideline to calculate the minimum axial displacement permissible in a tandem blade.
- It is concluded that if the second blade is located in such a way that the gap nozzle geometry promotes sufficient flow guidance for efficient momentum transfer on the rear blade suction surface the tandem blade shows lower losses than the two blades tested separately.
- It is concluded that in the design of a tandem blade compromise has to be done between various aerodynamic and geometrical parameters. Thus, the field velocity as well as the profile geometries and the gap nozzle area has to be taken into account in order to obtain an advantage in terms of loss reduction and deflection capabilities.

8.4 Numerical model

- The qualitative comparison between experimental data reported in the literature with a finite volume numerical method, shows that the influence of the relative position between the two profiles that conform a tandem blade is well represented by the computational calculations.

Appendix 1

NACA 651510 profile: geometry generation

Data of thickness distribution for a NACA 650010 profile and mean line $a = 1$ obtained in ref [1] is presented in Table A1-1.

ID	Station, x	Thickness distribution ordinates, y_t	Mean line ordinates, y_c	Mean line slope, dy_c/dx
1	0	0	0	0
2	0.005	0.00772	0.0025	0.4212
3	0.0075	0.00932	0.0035	0.38875
4	0.0125	0.01169	0.00535	0.3477
5	0.025	0.01574	0.0093	0.29155
6	0.05	0.02177	0.0158	0.2343
7	0.075	0.02647	0.0212	0.19995
8	0.1	0.0304	0.02585	0.17485
9	0.15	0.03666	0.03365	0.13805
10	0.2	0.04143	0.0398	0.1103
11	0.25	0.04503	0.04475	0.08745
12	0.3	0.0476	0.0486	0.06745
13	0.35	0.04924	0.0515	0.04925
14	0.4	0.04996	0.05355	0.03225
15	0.45	0.04963	0.05475	0.01595
16	0.5	0.04812	0.05515	0
17	0.55	0.0453	0.05475	-0.01595
18	0.6	0.04146	0.05355	-0.03225
19	0.65	0.03682	0.0515	-0.04925
20	0.7	0.03156	0.0486	-0.06745
21	0.75	0.02584	0.04475	-0.08745
22	0.8	0.01987	0.0398	-0.1103
23	0.85	0.01385	0.03365	-0.13805
24	0.9	0.0081	0.02585	-0.17485
25	0.95	0.00306	0.0158	-0.2343
26	1	0	0	0

Table A1-1: Thickness distribution for a NACA650010 and mean line data [1]

The process for combining the mean line and the thickness distribution is shown Figure A1-1.

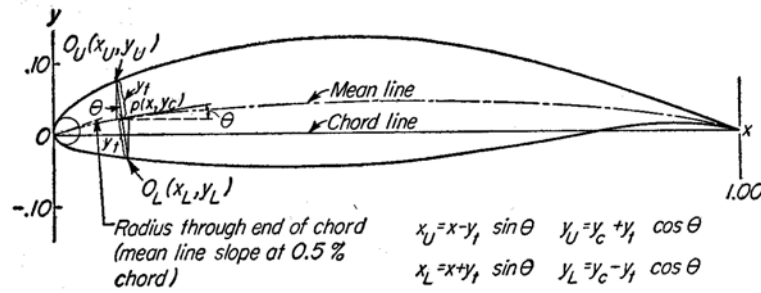


Figure A1-1: Blade geometry generation [1]

As seen, the ordinates of the final cambered wing section are obtained by laying off the thickness distribution perpendicular to the mean line.

If x_u and y_u represent, respectively, the abscissa and ordinate of a typical point of the upper surface of the wing section. The upper-surface coordinates are given by the following relations:

$$\begin{aligned} x_u &= x - y_t \sin \theta \\ y_u &= y_c + y_t \cos \theta \end{aligned}$$

Eq. A1-1

The corresponding expressions for the lower-surface coordinates are:

$$\begin{aligned} x_L &= x + y_t \sin \theta \\ y_L &= y_c - y_t \cos \theta \end{aligned}$$

Eq. A1-2

The desired camber line is properly obtained by scaling the ordinate of that camber line which would give an isolated airfoil lift coefficient of 1.

The results of the above procedure applied to the data in table 1 to generate a NACA 651510 profile is summarized in Table A1-2.

x	y_t^*	y_c^{**}	$\tan(\theta)$	x_u	y_u	x_L	y_L
0	0	0	-	0.00000	0.00000	0.00000	0.00000
0.005	0.00772	0.00375	0.6318	0.00088	0.01028	0.00912	-0.00278
0.0075	0.00932	0.00525	0.583125	0.00281	0.01330	0.01219	-0.00280
0.0125	0.01169	0.008025	0.52155	0.00709	0.01839	0.01791	-0.00234
0.025	0.01574	0.01395	0.437325	0.01869	0.02837	0.03131	-0.00047
0.05	0.02177	0.0237	0.35145	0.04278	0.04424	0.05722	0.00316
0.075	0.02647	0.0318	0.299925	0.06740	0.05715	0.08260	0.00645
0.1	0.0304	0.038775	0.262275	0.09229	0.06818	0.10771	0.00937
0.15	0.03666	0.050475	0.207075	0.14257	0.08637	0.15743	0.01458
0.2	0.04143	0.0597	0.16545	0.19324	0.10057	0.20676	0.01883
0.25	0.04503	0.067125	0.131175	0.24414	0.11177	0.25586	0.02248
0.3	0.0476	0.0729	0.101175	0.29521	0.12026	0.30479	0.02554
0.35	0.04924	0.07725	0.073875	0.34637	0.12636	0.35363	0.02814
0.4	0.04996	0.080325	0.048375	0.39759	0.13023	0.40241	0.03042
0.45	0.04963	0.082125	0.023925	0.44881	0.13174	0.45119	0.03251
0.5	0.04812	0.082725	0	0.50000	0.13085	0.50000	0.03461

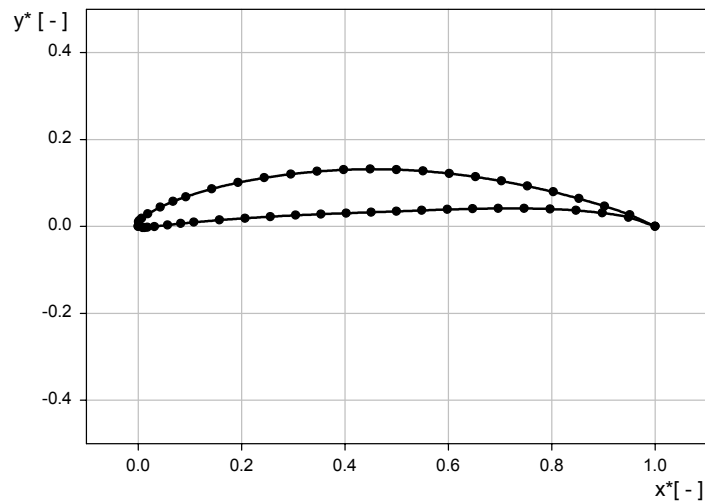
x	y_t^*	y_c^{**}	$\tan(\theta)$	x_u	y_u	x_L	y_L
0.55	0.0453	0.082125	-0.023925	0.55108	0.12741	0.54892	0.03684
0.6	0.04146	0.080325	-0.048375	0.60200	0.12174	0.59800	0.03891
0.65	0.03682	0.07725	-0.073875	0.65271	0.11397	0.64729	0.04053
0.7	0.03156	0.0729	-0.101175	0.70318	0.10430	0.69682	0.04150
0.75	0.02584	0.067125	-0.131175	0.75336	0.09275	0.74664	0.04150
0.8	0.01987	0.0597	-0.16545	0.80324	0.07930	0.79676	0.04010
0.85	0.01385	0.050475	-0.207075	0.85281	0.06404	0.84719	0.03691
0.9	0.0081	0.038775	-0.262275	0.90205	0.04661	0.89795	0.03094
0.95	0.00306	0.0237	-0.35145	0.95101	0.02659	0.94899	0.02081
1	0	0	-	1.00000	0.00000	1.00000	0.00000

Table A1-2: Final data points for a NACA651510

* Thickness distribution obtained from ordinates in Table 1.

** Ordinates of the mean line, 1.5 of the ordinate for lift coefficient equal to 1.

The final NACA651510 profile is presented in Figure A1-2.

**Figure A1-2: Final geometry of a NACA651510 profile**

Appendix 2

Reynolds average procedure

Reynolds averaged continuity equation

The continuity equation in tensor notation for a steady, incompressible flow is the following

$$\frac{\partial u_i}{\partial x_i} = 0$$

Eq. A2-1

Replacing the $f(x, y, z, t)$ operator in Eq. A2-1

$$\left(\frac{\partial \bar{u}_i}{\partial x_i} \right) + \left(\frac{\partial u'_i}{\partial x_i} \right) = 0$$

Eq. A2-2

time average entire equation,

$$\frac{1}{\Delta t} \int_t^{t+\Delta t} \left(\frac{\partial \bar{u}_i}{\partial x_i} \right) dt + \frac{1}{\Delta t} \int_t^{t+\Delta t} \left(\frac{\partial u'_i}{\partial x_i} \right) dt = 0$$

Eq. A2-3

commutation between differentiation and integration

$$\frac{\partial}{\partial x_i} \underbrace{\left(\frac{1}{\Delta t} \int_t^{t+\Delta t} \bar{u}_i dt \right)}_{\bar{u}_i} + \frac{\partial}{\partial x_i} \underbrace{\left(\frac{1}{\Delta t} \int_t^{t+\Delta t} u'_i dt \right)}_{\bar{u}'_i=0} = 0$$

Eq. A2-4

using the following properties, $\overline{\bar{f}} = \bar{f}$; $\overline{\bar{f}g} = \bar{f}\bar{g}$; $\overline{\bar{f} + g} = \bar{f} + \bar{g}$; $\overline{\left(\frac{\partial f}{\partial s} \right)} = \frac{\partial \bar{f}}{\partial s}$; $\overline{\int f ds} = \int \bar{f} ds$

and the fact that

$$\overline{f'}(x, y, z) = \frac{1}{\Delta t} \int_t^{t+\Delta t} f'(x, y, z, t) dt = 0$$

Eq. A2-5

the averaged continuity equation can be written as

$$\frac{\partial u'_i}{\partial x_i} = 0 \quad ; \quad \frac{\partial \bar{u}_i}{\partial x_i} = 0$$

Eq. A2-6

The main advantage of time averaging is that the terms \bar{u}'_i can be avoided, but it should be kept in mind that this is a mathematical technique not necessary a physical one [28].

Reynolds averaged momentum equation

Replacing the $f(x, y, z, t)$ operator in the momentum equation for a steady, incompressible and viscous flow

$$\rho \left(u_j \frac{\partial u_i}{\partial x_j} \right) = -\frac{\partial p}{\partial x_i} + \frac{\partial}{\partial x_j} \left[\mu \left(\frac{\partial u_i}{\partial x_j} + \frac{\partial u_j}{\partial x_i} \right) \right] \quad \text{with } u_i = \bar{u}_i + u'_i$$

Eq. A2-7

time average the fluctuating component of Eq. A2-7

$$\frac{1}{\Delta t} \int_t^{t+\Delta t} \left(u'_j \frac{\partial u'_i}{\partial x_j} \right) dt = \frac{1}{\Delta t} \int_t^{t+\Delta t} \left[\underbrace{u'_i \left(\frac{\partial u'_j}{\partial x_j} \right)}_0 + u'_j \frac{\partial u'_i}{\partial x_j} \right] dt = \dots = \frac{1}{\Delta t} \int_t^{t+\Delta t} \left[\frac{\partial (u_i u_j)}{\partial x_j} \right] dt$$

Eq. A2-8

commutation between differentiation and integration

$$\frac{\partial}{\partial x_j} \left[\frac{1}{\Delta t} \int_t^{t+\Delta t} \partial (u_i u_j) dt \right] = \frac{\partial}{\partial x_j} (\overline{u_i u_j})$$

Eq. A2-9

Replacing Eq. A2-9 in Eq. A2-7, the averaged momentum equation is expressed

$$\rho \bar{u}_j \frac{\partial \bar{u}_i}{\partial x_j} = -\frac{\partial \bar{p}}{\partial x_i} + \frac{\partial}{\partial x_j} \left[\mu \left(\frac{\partial \bar{u}_i}{\partial x_j} + \frac{\partial \bar{u}_j}{\partial x_i} \right) - \overline{\rho u'_i u'_j} \right]$$

Eq. A2-10

Appendix 3

Mesh generation

Due to the characteristics of the investigation (a general study of the tandem blades without a fixed geometry), the necessity to develop an interactive way to generate the mesh for different tandem configurations without rehash the whole process becomes primordial. Therefore, it is decided to use the GAMBIT parametric capabilities in order to give the user the possibility to create fast models for different tandem parameters.

The algorithm developed for this purpose use the following assumptions:

- The profiles are NACA 65xx10⁷ with a uniform chordwise loading from the leading edge to the trailing edge ($a=1$).
- The characteristic length, in the non-dimensional analysis, is the chord of the front blade ($x_{ref} = c_1$).
- The chord of the second profile is introduced as a fraction of the chord of the first profile.
- The front and rear outer boundaries are located at one-chord distances away from the blades, assuring that no effect of these boundaries on the cascade flow is evident.

Mesh characteristics

There exist two different types of mesh models that differ each other from the data structure used to describe the mesh itself. A structured mesh divides the model in regular parts such that the information of those parts can be stored in a matrix. In unstructured meshes the connections of each point are not regular and additional information is needed to specify the mesh. This kind of mesh does not store the global information of the model but it saves detailed data of the geometry.

The mesh characteristics used to create the tandem models are summarizes as follows:

- A structured mesh is created in the vicinity of the blade surface in order to capture the blade boundary layers and an unstructured in the remaining of the computational domain.
- The mesh density is higher in the gap nozzle area between the blades and in the proximities of the leading and trailing edges.
- The grid size is reduced until the grid independent solution is obtained.

⁷ The xx in the blade notation means that those values can be introduced as a parameter and are not fixed.

Geometry generation

The geometry of the blade is created using a set of geometrical and flow parameters, which are assigned by the variables referenced in Table A3 -1.

Variable Name	Meaning
<i>TANDEM_VAR1</i>	Inlet flow angle
<i>TANDEM_VAR2</i>	Outlet flow angle
<i>TANDEM_VAR3</i>	Stagger angle Blade1
<i>TANDEM_VAR4</i>	Stagger angle Blade2
<i>TANDEM_VAR5</i>	Lift Coefficient Blade1
<i>TANDEM_VAR6</i>	Lift Coefficient Blade2
<i>TANDEM_VAR7</i>	Solidity (c_l/s)
<i>TANDEM_VAR8</i>	Axial Displacement
<i>TANDEM_VAR9</i>	Tangential Displacement
<i>TANDEM_VAR10</i>	Chord of the rear blade related to the chord of the front blade.

Table A3 -1: Geometrical and flow parameters for a tandem blade

To generate the final geometry, two different models were created depending the relative position of the blades. This position is parameterized using the reference angle shown in Figure A3 -1.

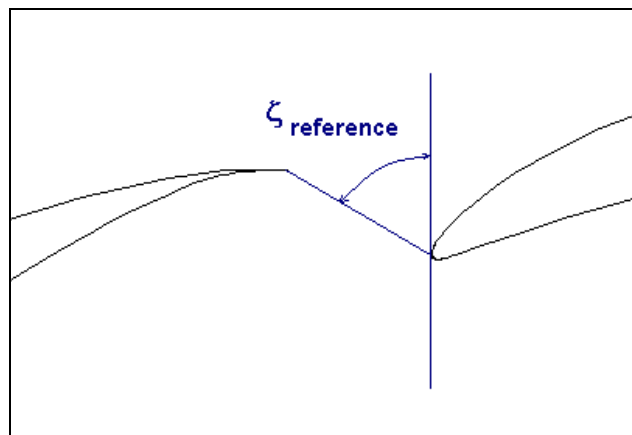


Figure A3 -1: relative position of the blades

So, when the angle $\xi_{reference}$ is higher than 45° the algorithm choose the model named “A” and if the angle ξ is lower than 45° (blades relative close or overlapping) the model “B” is used.

Model “A”

In this model the control surface consists of two faces (Figure A3 -2) bounded by 13 edges, 6 of which are the periodic and blade edges, three of which are used to split the face and four of which are the inlet and outlet edges.

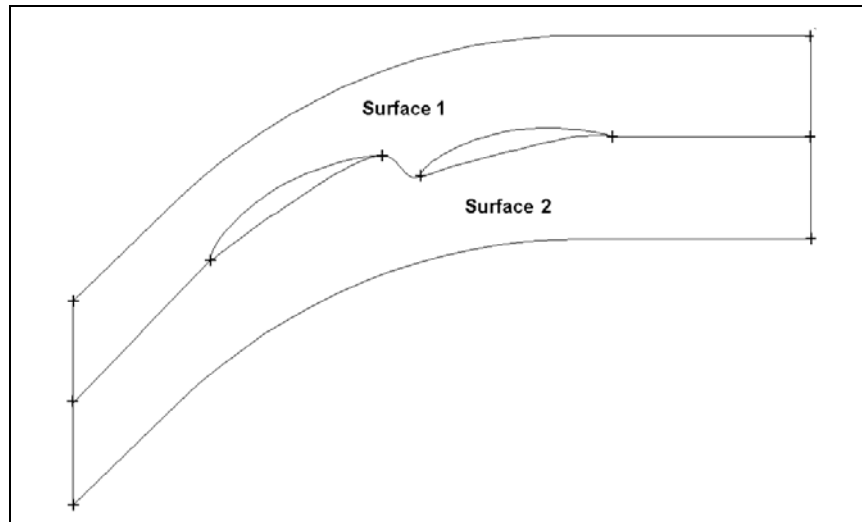


Figure A3 -2: Model “A”. Rear blade relative far behind the front blade

Model “B”

When the blades are relative close or they are overlapping, it is not possible to use the geometry in model “A”, because very cusp regions appear when the angle ξ is too small. Therefore, an iterative⁸ model (model “B”) was developed and the final result is presented in Figure A3 -3.

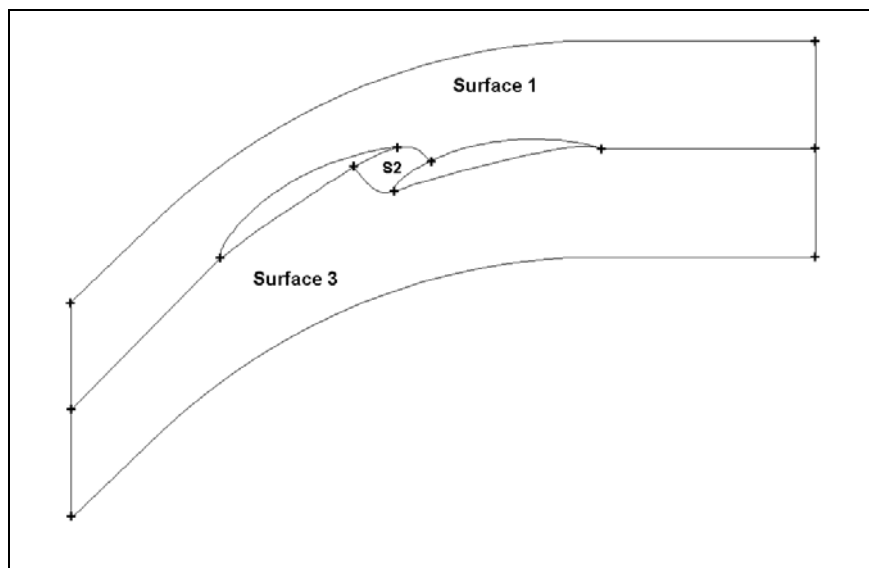


Figure A3 -3: model implemented when the angle ξ is lower than 45°

For this model the control surface consists of three faces (Figure A3 -3) that surround a region representing the blade; the face that represents the area between the two blades (S2) is named in the algorithm *INTERFERENCE_FACE* and two angles (Figure A3 -4) are used as a criterion to generate this area. The angle1 is fixed by a do... while bucle that iterates between the leading edge of the rear blade and the coordinate points of the pressure surface of the front blade. The angle2 is fixed by a do... while bucle that iterates between the trailing edge of the front blade and the coordinate points of the suction surface of the back tandem. The iteration process

⁸ It is said that this model is iterative because it is based on bucles (do ... while)

finishes when an angle introduced as a parameter in the algorithm is reached. This parameter was set to 45° in almost all the simulations in the thesis.

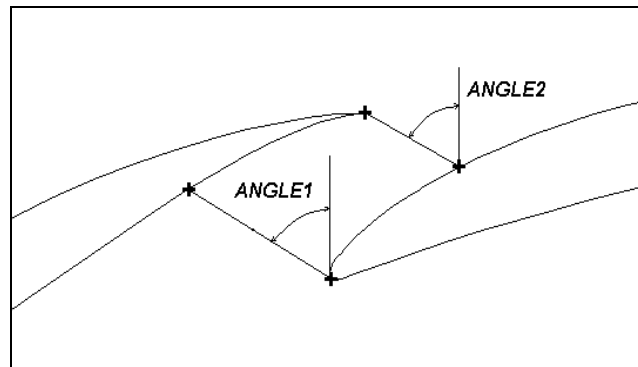


Figure A3 -4: Control angles of the interference face

Meshing the model

The algorithm assigns interval counts and grading parameters according to values specified by a set of variables named “*TANDEM_INT*” and “*TANDEM_GRAD*” respectively. Figure A3 -5 shows the general pattern of interval and grading assignments for a tandem blade model. The numbers shown in the figure indicate which parameters are used to specify interval counts and grading ratio. For example, the intervals assigned by default to edge a-b is specified by means of the variable named “*TANDEM_INT2*” and the grading is specified by the parameter “*TANDEM_GRAD2*”. For double sided grading edges, the variable that refers the grading range is asymmetric and there exist two different parameters that designate the grade for each side.

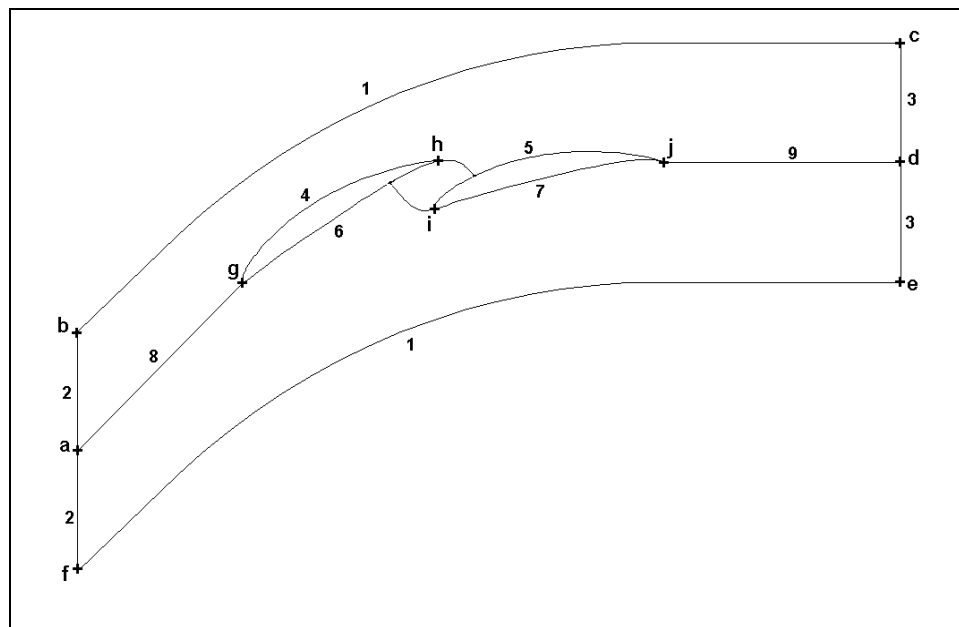


Figure A3 -5: Interval and grading pattern⁹

Table A3 -2 shows the interval count variables and the grading rate variables employed for each set of edges.

⁹ The figure shows a tandem configuration corresponding a model “B” but the pattern is the same for the model “A”

Interval count variable	Grading variable	Grading type	Edges
<i>TANDEM_INT1</i>	<i>TANDEM_GRAD1a</i> <i>TANDEM_GRAD1b</i>	Double-sided	b-c, f-e
<i>TANDEM_INT2</i>	<i>TANDEM_GRAD2</i>	Single-sided	a-b, a-f
<i>TANDEM_INT3</i>	<i>TANDEM_GRAD3</i>	Single-sided	d-c, d-e
<i>TANDEM_INT4</i>	<i>TANDEM_GRAD4a</i> <i>TANDEM_GRAD4b</i>	Double-sided	g-h (Suction Surface)
<i>TANDEM_INT5</i>	<i>TANDEM_GRAD5a</i> <i>TANDEM_GRAD5b</i>	Double-sided	i-j (Suction Surface)
<i>TANDEM_INT6</i>	<i>TANDEM_GRAD6a</i> <i>TANDEM_GRAD6b</i>	Double-sided	i-j (Pressure Surface)
<i>TANDEM_INT7</i>	<i>TANDEM_GRAD7a</i> <i>TANDEM_GRAD7b</i>	Double-sided	g-h (Pressure Surface)
<i>TANDEM_INT8</i>	<i>TANDEM_GRAD8</i>	Single-sided	a-g
<i>TANDEM_INT9</i>	<i>TANDEM_GRAD9</i>	Single-sided	j-d

Table A3 -2: Interval and Grading Variables

Structure of the program

The whole program that generates the final mesh of the tandem blades consists of four journal files described in Table A3 -3.

File name	Description
<i>tandem_profile.jou</i>	This file is the only one that has to be modified in order to create a model. In this file the user have to fix the value of the geometrical and mesh parameters for each tandem model.
<i>main_tandem_profile.jou</i>	This file generates the blade geometry for the two models ("A" and "B")
<i>case1.jou</i>	This file generates the mesh for the model "A"
<i>case2.jou</i>	This file generates the mesh for the model "B"
<i>NACA65010.jou</i>	This file contains the coordinates of the thickness distribution of a NACA650010 profile
<i>meanline_a1.jou</i>	This file contains the coordinates of the mean line for a chordwise loading equal to $a=1$

Table A3 -3: Files Description

tandem_profile.jou

/Journal File for GAMBIT 2.1.2

/***** Location of Blades Coordinate Files *****/

\$THICKNESS_FILE_BLADE1="/home/gcanon/First_simulation_tandem/NACA65010.jou"
\$MEANLINE_FILE_BLADE1="/home/gcanon/First_simulation_tandem/meanline_a1.jou"

\$THICKNESS_FILE_BLADE2="/home/gcanon/First_simulation_tandem/NACA65010.jou"
\$MEANLINE_FILE_BLADE2="/home/gcanon/First_simulation_tandem/meanline_a1.jou"

/***** VARIABLES *****/

/***** Geometrical and Flow Variables *****/

\$TANDEM_VAR1=65
\$TANDEM_VAR2=18
\$TANDEM_VAR3=55
\$TANDEM_VAR4=30
\$TANDEM_VAR5=1.2
\$TANDEM_VAR6=2.1
\$TANDEM_VAR7=1
\$TANDEM_VAR8=-0.05
\$TANDEM_VAR9=-0.1
\$TANDEM_VAR10=1

/***** Interval Count Variables *****/

\$TANDEM_INT1=128
\$TANDEM_INT2=11
\$TANDEM_INT3=11
\$TANDEM_INT4=80
\$TANDEM_INT5=80
\$TANDEM_INT6=76
\$TANDEM_INT7=76
\$TANDEM_INT8=50
\$TANDEM_INT9=58
/\$TANDEM_INT10=22

/***** Grading Variables *****/

\$TANDEM_GRAD1a=1
\$TANDEM_GRAD1b=1
\$TANDEM_GRAD2=1
\$TANDEM_GRAD3=1
\$TANDEM_GRAD4a=1.06
\$TANDEM_GRAD4b=1.04
\$TANDEM_GRAD5a=1.06
\$TANDEM_GRAD5b=1.04
\$TANDEM_GRAD6a=1.07
\$TANDEM_GRAD6b=1.045
\$TANDEM_GRAD7a=1.07
\$TANDEM_GRAD7b=1.045
\$TANDEM_GRAD8=0.96
\$TANDEM_GRAD9=0.965

/*****

read file "/home/gcanon/First_simulation_tandem/main_tandem_profile.jou"

end

main_tandem_profile.jou

```
/ Journal File for GAMBIT 2.1.2
```

```
reset
```

```
/******FRONT BLADE GEOMETRY *****/
```

```
/****** READ PROFILE GEOMETRY *****/
```

```
$cl=$TANDEM_VAR5
```

```
read file $THICKNESS_FILE_BLADE1
```

```
read file $MEANLINE_FILE_BLADE1
```

```
$i=1
```

```
declare $NACA65xx10 [1:6,1:26]
```

```
do para "$i" cond ($i .le. 26)
```

```
    $NACA65xx10[1,$i]=$NACA65010[1,$i]
```

```
    $NACA65xx10[2,$i]=$NACA65010[1,$i]-$NACA65010[2,$i]*SIN(ATAN($meanline_a1[3,$i]*$cl))
```

```
    $NACA65xx10[3,$i]=$meanline_a1[2,$i]*$cl+$NACA65010[2,$i]*COS(ATAN($meanline_a1[3,$i]*$cl))
```

```
    $NACA65xx10[4,$i]=$NACA65010[1,$i]+$NACA65010[2,$i]*SIN(ATAN($meanline_a1[3,$i]*$cl))
```

```
    $NACA65xx10[5,$i]=$meanline_a1[2,$i]*$cl-$NACA65010[2,$i]*COS(ATAN($meanline_a1[3,$i]*$cl))
```

```
    $NACA65xx10[6,$i]=$meanline_a1[2,$i]*$cl
```

```
enddo
```

```
/****** STAGGER COORDINATE - SYSTEM (FRONT BLADE) *****/
```

```
coordinate create "stagger_front_blade_sys" cartesian oldsystem "c_sys.1" offset 0 0 0 axis1\
```

```
"x" angle1 0 axis2 "y" angle2 0 axis3 "z" angle3 $TANDEM_VAR3 rotation
```

```
/******VERTEX CREATION *****/
```

```
declare $vertexname1_s [26]
```

```
declare $vertexname1_p [26]
```

```
declare $blade1_coordinates [1:4,1:26]
```

```
$i=1
```

```
do para "$i" cond ($i .le. 26)
```

```
    $vertexname1_s[$i]="vertex1_s." + NTOS($i)
```

```
    $vertexname1_p[$i]="vertex1_p." + NTOS($i)
```

```
    vertex create $vertexname1_s[$i] coordinates $NACA65xx10[2,$i] $NACA65xx10[3,$i] 0
```

```
    vertex create $vertexname1_p[$i] coordinates $NACA65xx10[4,$i] $NACA65xx10[5,$i] 0
```

```
    $blade1_coordinates[1,$i]=$NACA65xx10[2,$i]*cos($TANDEM_VAR3)-
```

```
$NACA65xx10[3,$i]*sin($TANDEM_VAR3))
```

```
    $blade1_coordinates[2,$i]=$NACA65xx10[3,$i]*cos($TANDEM_VAR3)+$NACA65xx10[2,$i]*sin($TANDEM
```

```
_VAR3))
```

```
    $blade1_coordinates[3,$i]=$NACA65xx10[4,$i]*cos($TANDEM_VAR3)-
```

```
$NACA65xx10[5,$i]*sin($TANDEM_VAR3))
```

```
    $blade1_coordinates[4,$i]=$NACA65xx10[5,$i]*cos($TANDEM_VAR3)+$NACA65xx10[4,$i]*sin($TANDEM
```

```
_VAR3))
```

```
enddo
```

```
/****** EDGES CREATION *****/
```

```
/****** NOSE *****/
```

```
edge create nurbs $vertexname1_s[4] $vertexname1_s[3] $vertexname1_s[2] $vertexname1_s[1]\
```

```
$vertexname1_p[2] $vertexname1_p[3] $vertexname1_p[4] interpolate
```

```
edge split "edge.1" vertex $vertexname1_s[1] connected
```

```
edge modify "edge.1" label "nose1_s"
```

```
edge modify "edge.2" label "nose1_p"
```

```
/****** SUCTION_SURFACE *****/
```

```
edge create "ID1" nurbs $vertexname1_s[4] $vertexname1_s[5] $vertexname1_s[6] $vertexname1_s[7] interpolate
```

```
edge create "ID2" nurbs $vertexname1_s[7] $vertexname1_s[8] $vertexname1_s[9] $vertexname1_s[10] interpolate
```

```
edge create "ID3" nurbs $vertexname1_s[10] $vertexname1_s[11] $vertexname1_s[12] $vertexname1_s[13] interpolate
```

```
edge create "ID4" nurbs $vertexname1_s[13] $vertexname1_s[14] $vertexname1_s[15] $vertexname1_s[16] interpolate
```

```
edge create "ID5" nurbs $vertexname1_s[16] $vertexname1_s[17] $vertexname1_s[18] $vertexname1_s[19] interpolate
```

```
edge create "ID6" nurbs $vertexname1_s[19] $vertexname1_s[20] $vertexname1_s[21] $vertexname1_s[22]
```

```
$vertexname1_s[23] $vertexname1_s[24] interpolate
```

```
edge create "ID7" nurbs $vertexname1_s[24] $vertexname1_s[25] $vertexname1_s[26] interpolate
```

```
edge merge "nose1_s" "ID1" "ID2" "ID3" "ID4" "ID5" "ID6" "ID7"
```

```

edge convert "v_edge.10"
edge modify "edge.10" label "SUCTION_SURFACE_1"

/***** PRESSURE_SURFACE *****/
edge create "ID1" nurbs $vertexname1_p[4] $vertexname1_p[5] $vertexname1_p[6] $vertexname1_p[7] interpolate
edge create "ID2" nurbs $vertexname1_p[7] $vertexname1_p[8] $vertexname1_p[9] $vertexname1_p[10] interpolate
edge create "ID3" nurbs $vertexname1_p[10] $vertexname1_p[11] $vertexname1_p[12] $vertexname1_p[13] interpolate
edge create "ID4" nurbs $vertexname1_p[13] $vertexname1_p[14] $vertexname1_p[15] $vertexname1_p[16] interpolate
edge create "ID5" nurbs $vertexname1_p[16] $vertexname1_p[17] $vertexname1_p[18] $vertexname1_p[19] interpolate
edge create "ID6" nurbs $vertexname1_p[19] $vertexname1_p[20] $vertexname1_p[21] $vertexname1_p[22]
$vertexname1_p[23] $vertexname1_p[24] interpolate
edge create "ID7" nurbs $vertexname1_p[24] $vertexname1_p[25] $vertexname1_p[26] interpolate
edge merge "nose1_p" "ID1" "ID2" "ID3" "ID4" "ID5" "ID6" "ID7"
edge convert "v_edge.18"
edge modify "edge.18" label "PRESSURE_SURFACE_1"

/***** REAR BLADE GEOMETRY *****/

/***** READ PROFILE GEOMETRY *****/
$c=$STANDEM_VAR10
$c1=$STANDEM_VAR6
read file $THICKNESS_FILE_BLADE2
read file $MEANLINE_FILE_BLADE2
$i=1
declare $NACA65xx10 [1:6,1:26]
do para "$i" cond ($i .le. 26)
    $NACA65xx10[1,$i]=$NACA65010[1,$i]*$c
    $NACA65xx10[2,$i]=$NACA65010[1,$i]*$c-$c*$NACA65010[2,$i]*SIN(ATAN($meanline_a1[3,$i]*$c1))
    $NACA65xx10[3,$i]=$meanline_a1[2,$i]*$c1*$c+$c*$NACA65010[2,$i]*COS(ATAN($meanline_a1[3,$i]*$c1))
    $NACA65xx10[4,$i]=$NACA65010[1,$i]*$c+$c*$NACA65010[2,$i]*SIN(ATAN($meanline_a1[3,$i]*$c1))
    $NACA65xx10[5,$i]=$meanline_a1[2,$i]*$c1*$c-$c*$NACA65010[2,$i]*COS(ATAN($meanline_a1[3,$i]*$c1))
    $NACA65xx10[6,$i]=$meanline_a1[2,$i]*$c1*$c
enddo

/***** NEW COORDINATE - SYSTEM / REAR PROFILE *****/
$x_distance=cos($STANDEM_VAR3)+$STANDEM_VAR8
$y_distance=sin($STANDEM_VAR3)+$STANDEM_VAR9
coordinate create "stagger_rear_profile_sys" cartesian oldsystem "c_sys.1" offset $x_distance $y_distance 0 axis1\
"x" angle1 0 axis2 "y" angle2 0 axis3 "z" angle3 $STANDEM_VAR4 rotation

/***** VERTEX CREATION *****/
declare $vertexname2_s [26]
declare $vertexname2_p [26]
declare $blade2_coordinates [1:4,1:26]
$i=1
do para "$i" cond ($i .le. 26)
    $vertexname2_s[$i]="vertex2_s." + NTOS($i)
    $vertexname2_p[$i]="vertex2_p." + NTOS($i)
    vertex create $vertexname2_s[$i] coordinates $NACA65xx10[2,$i] $NACA65xx10[3,$i] 0
    vertex create $vertexname2_p[$i] coordinates $NACA65xx10[4,$i] $NACA65xx10[5,$i] 0
    $blade2_coordinates[1,$i]=$x_distance+($NACA65xx10[2,$i]*cos($STANDEM_VAR4)-
$NACA65xx10[3,$i]*sin($STANDEM_VAR4))
    $blade2_coordinates[2,$i]=$y_distance+($NACA65xx10[3,$i]*cos($STANDEM_VAR4)+$NACA65xx10[2,$i]*sin
($STANDEM_VAR4))
    $blade2_coordinates[3,$i]=$x_distance+($NACA65xx10[4,$i]*cos($STANDEM_VAR4)-
$NACA65xx10[5,$i]*sin($STANDEM_VAR4))
    $blade2_coordinates[4,$i]=$y_distance+($NACA65xx10[5,$i]*cos($STANDEM_VAR4)+$NACA65xx10[4,$i]*sin
($STANDEM_VAR4))
enddo

/***** EDGES CREATION *****/

/***** NOSE *****/
edge create nurbs $vertexname2_s[4] $vertexname2_s[3] $vertexname2_s[2] $vertexname2_s[1]\
$vertexname2_p[2] $vertexname2_p[3] $vertexname2_p[4] interpolate
edge split "edge.19" vertex $vertexname2_s[1] connected
edge modify "edge.19" label "nose2_s"
edge modify "edge.20" label "nose2_p"

```

```

/***** SUCTION_SURFACE *****/
edge create "ID1" nurbs $vertexname2_s[4] $vertexname2_s[5] $vertexname2_s[6] $vertexname2_s[7] interpolate
edge create "ID2" nurbs $vertexname2_s[7] $vertexname2_s[8] $vertexname2_s[9] $vertexname2_s[10] interpolate
edge create "ID3" nurbs $vertexname2_s[10] $vertexname2_s[11] $vertexname2_s[12] $vertexname2_s[13] interpolate
edge create "ID4" nurbs $vertexname2_s[13] $vertexname2_s[14] $vertexname2_s[15] $vertexname2_s[16] interpolate
edge create "ID5" nurbs $vertexname2_s[16] $vertexname2_s[17] $vertexname2_s[18] $vertexname2_s[19] interpolate
edge create "ID6" nurbs $vertexname2_s[19] $vertexname2_s[20] $vertexname2_s[21] $vertexname2_s[22]
$vertexname2_s[23] $vertexname2_s[24] interpolate
edge create "ID7" nurbs $vertexname2_s[24] $vertexname2_s[25] $vertexname2_s[26] interpolate
edge merge "nose2_s" "ID1" "ID2" "ID3" "ID4" "ID5" "ID6" "ID7"
edge convert "v_edge.28"
edge modify "edge.28" label "SUCTION_SURFACE_2"

/***** PRESSURE_SURFACE *****/
edge create "ID1" nurbs $vertexname2_p[4] $vertexname2_p[5] $vertexname2_p[6] $vertexname2_p[7] interpolate
edge create "ID2" nurbs $vertexname2_p[7] $vertexname2_p[8] $vertexname2_p[9] $vertexname2_p[10] interpolate
edge create "ID3" nurbs $vertexname2_p[10] $vertexname2_p[11] $vertexname2_p[12] $vertexname2_p[13] interpolate
edge create "ID4" nurbs $vertexname2_p[13] $vertexname2_p[14] $vertexname2_p[15] $vertexname2_p[16] interpolate
edge create "ID5" nurbs $vertexname2_p[16] $vertexname2_p[17] $vertexname2_p[18] $vertexname2_p[19] interpolate
edge create "ID6" nurbs $vertexname2_p[19] $vertexname2_p[20] $vertexname2_p[21] $vertexname2_p[22]
$vertexname2_p[23] $vertexname2_p[24] interpolate
edge create "ID7" nurbs $vertexname2_p[24] $vertexname2_p[25] $vertexname2_p[26] interpolate

edge merge "nose2_p" "ID1" "ID2" "ID3" "ID4" "ID5" "ID6" "ID7"
edge convert "v_edge.36"
edge modify "edge.36" label "PRESSURE_SURFACE_2"

/***** BOUNDARY GEOMETRY *****/

/***** VERTEX CREATION *****/

$midpitch=0.5/($TANDEM_VAR7)
coordinate activate "c_sys.1"
vertex create "P1" coordinates (-cos($TANDEM_VAR1)) (-sin($TANDEM_VAR1)-$midpitch) 0
vertex create "P2" coordinates (-cos($TANDEM_VAR1)) -sin($TANDEM_VAR1) 0
vertex create "P3" coordinates (-cos($TANDEM_VAR1)) (-sin($TANDEM_VAR1)+$midpitch) 0
$x=cos($TANDEM_VAR3)/2
$y=0.5*sin($TANDEM_VAR1)+$midpitch
vertex create "P4" coordinates $x $y 0
$x=cos($TANDEM_VAR3)+$TANDEM_VAR8+($TANDEM_VAR10*cos($TANDEM_VAR4)/2)
$y=sin($TANDEM_VAR3)+$TANDEM_VAR9+$TANDEM_VAR10*sin($TANDEM_VAR4)+$midpitch
vertex create "P5" coordinates $x $y 0
$x=(cos($TANDEM_VAR2))+cos($TANDEM_VAR3)+$TANDEM_VAR8+$TANDEM_VAR10*cos($TANDEM_VAR4)
$y=sin($TANDEM_VAR2)+sin($TANDEM_VAR3)+$TANDEM_VAR9+$TANDEM_VAR10*sin($TANDEM_VAR4)+$
midpitch
vertex create "P6" coordinates $x $y 0
$x=(cos($TANDEM_VAR2))+cos($TANDEM_VAR3)+$TANDEM_VAR8+$TANDEM_VAR10*cos($TANDEM_VAR4)
$y=sin($TANDEM_VAR2)+sin($TANDEM_VAR3)+$TANDEM_VAR9+$TANDEM_VAR10*sin($TANDEM_VAR4)
vertex create "P7" coordinates $x $y 0
$x=(cos($TANDEM_VAR2))+cos($TANDEM_VAR3)+$TANDEM_VAR8+$TANDEM_VAR10*cos($TANDEM_VAR4)
$y=sin($TANDEM_VAR2)+sin($TANDEM_VAR3)+$TANDEM_VAR9+$TANDEM_VAR10*sin($TANDEM_VAR4)-
$midpitch
vertex create "P8" coordinates $x $y 0
$x=cos($TANDEM_VAR3)+$TANDEM_VAR8+($TANDEM_VAR10*cos($TANDEM_VAR4)/2)
$y=sin($TANDEM_VAR3)+$TANDEM_VAR9+$TANDEM_VAR10*sin($TANDEM_VAR4)-$midpitch
vertex create "P9" coordinates $x $y 0
$x=cos($TANDEM_VAR3)/2
$y=0.5*sin($TANDEM_VAR1)-$midpitch
vertex create "P10" coordinates $x $y 0

/***** EDGE CREATION *****/

edge create "INLET_PRESSURE" straight "P1" "P2"
edge create "INLET_SUCTION" straight "P2" "P3"
edge create "R3" straight "P3" "P4"
edge create "R1" straight "P5" "P6"
edge create "OUTLET_SUCTION" straight "P6" "P7"

```

```

edge create "OUTLET_PRESSURE" straight "P7" "P8"
edge create "R4" straight "P8" "P9"
edge create "R6" straight "P10" "P1"
$i=1
$FILLED_RADIUS=0.1
do para "$i" cond ($i .eq. 1) INCR 0
    edge create "R5" fillet "R4" "R6" parameters 0.01 0.99 RADIUS $FILLED_RADIUS trim
    edge create "R2" fillet "R3" "R1" parameters 0.01 0.99 RADIUS $FILLED_RADIUS trim
    $i = OPERERRR()
    $FILLED_RADIUS=$FILLED_RADIUS+0.1
enddo
edge create "H1" straight "P2" $vertexname1_s[1]
edge create "H2" straight "P7" $vertexname2_s[26]
edge merge "R1" "R2" "R3"
edge convert "v_edge.49"
edge modify "edge.49" label "PERIODIC1"
edge merge "R4" "R5" "R6"
edge convert "v_edge.50"
edge modify "edge.50" label "PERIODIC2"

/***** BOUNDARY LINES (INTERFERENCE) *****/

$slope=ATAN(($blade2_coordinates[2,1]-$blade1_coordinates[2,26])/($blade2_coordinates[1,1]-
$blade1_coordinates[1,26]))
if cond ($slope .ge. -45 .and. $slope .le. 0)
    $x_coordinate1=$blade1_coordinates[1,26]+cos(0)*0.021
    $y_coordinate1=$blade1_coordinates[2,26]+sin(0)*0.021
    vertex create "ve1_H3" coordinates $x_coordinate1 $y_coordinate1 0
    $x_coordinate2=$blade2_coordinates[1,1]-cos(21)*0.021
    $y_coordinate2=$blade2_coordinates[2,1]-sin(21)*0.021
    vertex create "ve2_H3" coordinates $x_coordinate2 $y_coordinate2 0
    edge create "H3" nurbs $vertexname1_s[26] "ve1_H3" "ve2_H3" $vertexname2_s[1] interpolate
    if cond ($eval.EQ. 1)
        read file "/home/gcanon/First_simulation_tandem/case1.jou"
    endif
else
    $i=1
    do para "$i" cond ($i .le. 26)
        $slope=ATAN(($blade2_coordinates[2,$i]-$blade1_coordinates[2,26])/($blade2_coordinates[1,$i]-
$blade1_coordinates[1,26]))
        if cond ($slope .ge. -45.and. $slope .le. 0)
            vertex create "ve2_L3" coordinates $blade2_coordinates[1,$i] $blade2_coordinates[2,$i] 0

            $x_coordinate=$blade1_coordinates[1,26]+cos(0)*0.0021
            $y_coordinate=$blade1_coordinates[2,26]+sin(0)*0.0021
            vertex create "ve1_L3" coordinates $x_coordinate $y_coordinate 0
            edge create "L3" nurbs "ve2_L3" "ve1_L3" $vertexname1_s[26] interpolate
            declare $LENGHT2 [1:4]
            $LENGHT2[1]=arclen("SUCTION_SURFACE_2")
            edge split "SUCTION_SURFACE_2" vertex "ve2_L3" connected
            edge modify "SUCTION_SURFACE_2" label "INTERFERENCE_BLADE_2"
            edge modify "edge.52" label "SUCTION_SURFACE_2"
            $LENGHT2[2]=arclen("SUCTION_SURFACE_2")
            $LENGHT2[3]=arclen("INTERFERENCE_BLADE_2")
            $LENGHT2[4]=arclen("L3")
            break
        endif
    enddo
    $i=1
    do para "$i" cond ($i .le. 26)
        $k=27-$i
        $slope=ATAN(($blade2_coordinates[2,1]-$blade1_coordinates[4,$k])/($blade2_coordinates[1,1]-
$blade1_coordinates[3,$k]))
        if cond ($slope .ge. -45 .and. $slope .le. 0)
            vertex create "ve2_L4" coordinates $blade1_coordinates[3,$k] $blade1_coordinates[4,$k] 0

            $x_coordinate=$blade2_coordinates[1,1]-cos(21)*0.021
            $y_coordinate=$blade2_coordinates[2,1]-sin(21)*0.021
            vertex create "ve1_L4" coordinates $x_coordinate $y_coordinate 0

```



```
edge create "L4" nurbs "ve2_L4" "ve1_L4" $vertexname2_s[1] interpolate
declare $LENGHT1 [1:4]
$LENGHT1[1]=arclen("PRESSURE_SURFACE_1")
edge split "PRESSURE_SURFACE_1" vertex "ve2_L4" connected
edge modify "edge.54" label "INTERFERENCE_BLADE_1"
$LENGHT1[2]=arclen("PRESSURE_SURFACE_1")
$LENGHT1[3]=arclen("INTERFERENCE_BLADE_1")
$LENGHT1[4]=arclen("L4")
break
endif
enddo
read file "/home/gcanon/First_simulation_tandem/case2.jou"
endif
```

case1.jou

```

/***** MESH MODEL 1 *****/

/ ***** FACE CREATION *****/

face create "SUCTION_FACE" wireframe "INLET_SUCTION" "PERIODIC1" "OUTLET_SUCTION" "H2"
"SUCTION_SURFACE_2" "H3" "SUCTION_SURFACE_1" "H1" real
face create "PRESSURE_FACE" wireframe "INLET_PRESSURE" "PERIODIC2" "OUTLET_PRESSURE" "H2"
"PRESSURE_SURFACE_2" "H3" "PRESSURE_SURFACE_1" "H1" real

/ ***** MESHING THE MODEL *****/

$х=$blade1_coordinates[1,26]-$blade2_coordinates[1,1]
$у=$blade1_coordinates[2,26]-$blade2_coordinates[2,1]
$DISTANCE=SQRT(POW($х,2)+POW($у,2))

/*****BOUNDARY LAYER *****/

blayer create "B_surface" first 0.0045 growth 1.1 rows 4 transition 1 trows 0
blayer attach "B_surface" face "SUCTION_FACE" "SUCTION_FACE" edge "SUCTION_SURFACE_1"
"SUCTION_SURFACE_2"
blayer create "B_presface" first 0.0045 growth 1.1 rows 4 transition 1 trows 0
blayer attach "B_presface" face "PRESSURE_FACE" "PRESSURE_FACE" edge "PRESSURE_SURFACE_1"
"PRESSURE_SURFACE_2"

/ ***** MESH EDGES *****/

$TANDEM_INT10=INT(22*$DISTANCE/0.1)
edge mesh "PERIODIC1" successive ratio1 $TANDEM_GRAD1a ratio2 $TANDEM_GRAD1b intervals $TANDEM_INT1
edge link "PERIODIC1" "PERIODIC2" direction 0 1 periodic
edge mesh "INLET_SUCTION" successive ratio1 $TANDEM_GRAD2 intervals $TANDEM_INT2
edge link "INLET_SUCTION" "INLET_PRESSURE" direction 0 1
edge mesh "OUTLET_SUCTION" successive ratio1 $TANDEM_GRAD3 intervals $TANDEM_INT3
edge link "OUTLET_SUCTION" "OUTLET_PRESSURE" direction 0 1
edge mesh "SUCTION_SURFACE_2" successive ratio1 $TANDEM_GRAD5a ratio2 $TANDEM_GRAD5b intervals
$TANDEM_INT5
edge mesh "PRESSURE_SURFACE_2" successive ratio1 $TANDEM_GRAD7a ratio2 $TANDEM_GRAD7b intervals
$TANDEM_INT7
edge mesh "H1" successive ratio1 $TANDEM_GRAD9 intervals $TANDEM_INT9
edge mesh "H2" successive ratio1 $TANDEM_GRAD8 intervals $TANDEM_INT8
/edge mesh "H3" successive ratio1 $TANDEM_GRAD10a ratio2 $TANDEM_GRAD10b intervals $TANDEM_INT10
edge mesh "H3" lastlength ratio1 0.006 ratio2 0.006 intervals $TANDEM_INT10

/ ***** MESH FACES *****/

$i=1
do para "$i" cond ($i .eq. 1) INCR 0
    edge mesh "PRESSURE_SURFACE_1" successive ratio1 $TANDEM_GRAD6a ratio2 $TANDEM_GRAD6b
intervals $TANDEM_INT6
    face mesh "PRESSURE_FACE" pave
    $i = OPERERR()
    if cond ($i .eq. 1)
        $TANDEM_INT6=$TANDEM_INT6 +1
        edge delete "PRESSURE_SURFACE_1" lowertopology onlymesh
    endif
enddo

$i=1
do para "$i" cond ($i .eq. 1) INCR 0
    edge mesh "SUCTION_SURFACE_1" successive ratio1 $TANDEM_GRAD4a ratio2 $TANDEM_GRAD4b
intervals $TANDEM_INT4
    face mesh "SUCTION_FACE" pave
    $i = OPERERR()
    if cond ($i .eq. 1)
        $TANDEM_INT4=$TANDEM_INT4 +1

```

```

        edge delete "SUCTION_SURFACE_1" lowertopology onlymesh
    endif
enddo

/ ***** BOUNDARY CONDITIONS *****

solver select "FLUENT 5/6"

/***** ZONES *****/

physics create "Fluid" ctype "FLUID" face "SUCTION_FACE" "PRESSURE_FACE"

/***** BOUNDARY *****/

physics create "velocity_inlet_pressure" btype "VELOCITY_INLET" edge "INLET_PRESSURE"
physics create "velocity_inlet_suction" btype "VELOCITY_INLET" edge "INLET_SUCTION"
physics create "suction_surface_1" btype "WALL" edge "SUCTION_SURFACE_1"
physics create "suction_surface_2" btype "WALL" edge "SUCTION_SURFACE_2"
physics create "pressure_surface_1" btype "WALL" edge "PRESSURE_SURFACE_1"
physics create "pressure_surface_2" btype "WALL" edge "PRESSURE_SURFACE_2"
physics create "interior_leading_edge" btype "INTERIOR" edge "H1"
physics create "interior_trailing_edge" btype "INTERIOR" edge "H2"
physics create "midline" btype "INTERIOR" edge "H3"
physics create "periodic_boundary" btype "PERIODIC" edge "PERIODIC1" "PERIODIC2"
physics create "pressure_outlet_pressure" btype "PRESSURE_OUTLET" edge "OUTLET_PRESSURE"
physics create "pressure_outlet_suction" btype "PRESSURE_OUTLET" edge "OUTLET_SUCTION"

/***** EXPORT MESH *****/

$MESH="/home/gcanon/tandem/" + $TANDEM + "/" + $TANDEM + ".msh"
export fluent5 $MESH nozval

```

case2.jou

```

/ ***** Mesh Variables *****

$TANDEM_INT5a=INT($TANDEM_INT5*($LENGHT2[2]/$LENGHT2[1]))*1
$TANDEM_INT5b=INT($TANDEM_INT5*($LENGHT2[3]/$LENGHT2[1]))*2

$TANDEM_INT6a=INT($TANDEM_INT6*($LENGHT1[2]/$LENGHT1[1]))
$TANDEM_INT6b=INT($TANDEM_INT6*($LENGHT1[3]/$LENGHT1[1]))*1.5

/***** L3 *****/
$intervals_L3=INT(20*$LENGHT2[4]/0.1)
$lastlength_ratio1_L3=0.006
$lastlength_ratio2_L3=0.006

/***** L4 *****/
$intervals_L4=INT(35*$LENGHT1[4]/0.15)
$lastlength_ratio1_L4=0.006
$lastlength_ratio2_L4=0.006

/***** MESH MODEL 2 *****/

/ ***** FACE CREATION *****/

face create "SUCTION_FACE" wireframe "INLET_SUCTION" "PERIODIC1" "OUTLET_SUCTION" "H2"
"SUCTION_SURFACE_2" "L3" "SUCTION_SURFACE_1" "H1" real
face create "PRESSURE_FACE" wireframe "INLET_PRESSURE" "PERIODIC2" "OUTLET_PRESSURE" "H2"
"PRESSURE_SURFACE_2" "L4" "PRESSURE_SURFACE_1" "H1" real
face create "INTERFERENCE_FACE" wireframe "L4" "INTERFERENCE_BLADE_2" "L3"
"INTERFERENCE_BLADE_1" real

/*****BOUNDARY LAYER *****/

blayer create "B_surface" first 0.0045 growth 1.1 rows 4 transition 1 trows 0
blayer attach "B_surface" face "SUCTION_FACE" "SUCTION_FACE" edge "SUCTION_SURFACE_1"
"SUCTION_SURFACE_2"
blayer create "B_presface" first 0.0045 growth 1.1 rows 4 transition 1 trows 0
blayer attach "B_presface" face "PRESSURE_FACE" "PRESSURE_FACE" edge "PRESSURE_SURFACE_1"
"PRESSURE_SURFACE_2"
blayer create "B_interface" first 0.0045 growth 1.1 rows 4 transition 1 trows 0
blayer attach "B_interface" face "INTERFERENCE_FACE" "INTERFERENCE_FACE" edge
"INTERFERENCE_BLADE_1" "INTERFERENCE_BLADE_2"

/ ***** MESH EDGES *****/

edge mesh "PERIODIC1" successive ratio1 $TANDEM_GRAD1a ratio2 $TANDEM_GRAD1b intervals $TANDEM_INT1
edge link "PERIODIC1" "PERIODIC2" direction 0 1 periodic
edge mesh "INLET_SUCTION" successive ratio1 $TANDEM_GRAD2 intervals $TANDEM_INT2
edge link "INLET_SUCTION" "INLET_PRESSURE" direction 0 1
edge mesh "OUTLET_SUCTION" successive ratio1 $TANDEM_GRAD3 intervals $TANDEM_INT3
edge link "OUTLET_SUCTION" "OUTLET_PRESSURE" direction 0 1
edge mesh "PRESSURE_SURFACE_1" successive ratio1 $TANDEM_GRAD6a ratio2 1 intervals $TANDEM_INT6a
edge mesh "INTERFERENCE_BLADE_1" successive ratio1 1 ratio2 $TANDEM_GRAD6b intervals $TANDEM_INT6b
edge mesh "SUCTION_SURFACE_2" successive ratio1 1 ratio2 $TANDEM_GRAD5b intervals $TANDEM_INT5a
edge mesh "H1" successive ratio1 $TANDEM_GRAD9 intervals $TANDEM_INT9
edge mesh "H2" successive ratio1 $TANDEM_GRAD8 intervals $TANDEM_INT8
edge mesh "L3" lastlength ratio1 $lastlength_ratio1_L3 ratio2 $lastlength_ratio2_L3 intervals $intervals_L3
edge mesh "L4" lastlength ratio1 $lastlength_ratio1_L4 ratio2 $lastlength_ratio2_L4 intervals $intervals_L4

/ ***** MESH FACES *****/

$i=1
do para "$i" cond ($i .eq. 1) INCR 0
    edge mesh "PRESSURE_SURFACE_2" successive ratio1 $TANDEM_GRAD7a ratio2 $TANDEM_GRAD7b
intervals $TANDEM_INT7
    face mesh "PRESSURE_FACE" pave
    $i = OPERERR()
    if cond ($i .eq. 1)

```

```

        $TANDEM_INT7=$TANDEM_INT7+1
        edge delete "PRESSURE_SURFACE_2" lowertopology onlymesh
    endif
enddo

$i=1
do para "$i" cond ($i .eq. 1) INCR 0
    edge mesh "SUCTION_SURFACE_1" successive ratio1 $TANDEM_GRAD4a ratio2 $TANDEM_GRAD4b
    intervals $TANDEM_INT4
    face mesh "SUCTION_FACE" pave
    $i = OPERERR()
    if cond ($i .eq. 1)
        $TANDEM_INT4=$TANDEM_INT4+1
        edge delete "SUCTION_SURFACE_1" lowertopology onlymesh
    endif
enddo

$i=1
do para "$i" cond ($i .eq. 1) INCR 0
    edge mesh "INTERFERENCE_BLADE_2" successive ratio1 $TANDEM_GRAD5a ratio2 1 intervals
    $TANDEM_INT5b
    face mesh "INTERFERENCE_FACE" pave
    $i = OPERERR()
    if cond ($i .eq. 1)
        $TANDEM_INT5b=$TANDEM_INT5b+1
        edge delete "INTERFERENCE_BLADE_2" lowertopology onlymesh
    endif
enddo

/ ***** BOUNDARY CONDITIONS *****

/*****SOLVER*****/

solver select "FLUENT 5/6"

/***** ZONES *****/

physics create "Fluid" ctype "FLUID" face "SUCTION_FACE" "PRESSURE_FACE" "INTERFERENCE_FACE"

/***** BOUNDARY *****/

physics create "velocity_inlet_pressure" btype "VELOCITY_INLET" edge "INLET_PRESSURE"
physics create "velocity_inlet_suction" btype "VELOCITY_INLET" edge "INLET_SUCTION"
physics create "suction_surface_1" btype "WALL" edge "SUCTION_SURFACE_1"
physics create "suction_surface_2" btype "WALL" edge "SUCTION_SURFACE_2" "INTERFERENCE_BLADE_2"
physics create "pressure_surface_1" btype "WALL" edge "PRESSURE_SURFACE_1" "INTERFERENCE_BLADE_1"
physics create "pressure_surface_2" btype "WALL" edge "PRESSURE_SURFACE_2"
physics create "interior_leading_edge" btype "INTERIOR" edge "H1"
physics create "interior_trailing_edge" btype "INTERIOR" edge "H2"
physics create "midline_1" btype "INTERIOR" edge "L3"
physics create "midline_2" btype "INTERIOR" edge "L4"
physics create "periodic_boundary" btype "PERIODIC" edge "PERIODIC1" "PERIODIC2"
physics create "pressure_outlet_pressure" btype "PRESSURE_OUTLET" edge "OUTLET_PRESSURE"
physics create "pressure_outlet_suction" btype "PRESSURE_OUTLET" edge "OUTLET_SUCTION"

/***** EXPORT MESH *****/

$MESH="/home/gcanon/tandem/" + $TANDEM + "/" + $TANDEM + ".msh"
export fluent5 $MESH nozval

```

NACA65010.jou

/Journal File for GAMBIT 2.1.2

/***** PROFILE GEOMETRY (Ref [1]) *****/

/*****Thickness Distribution *****/

declare \$NACA65010 [1:2,1:26]

/*****Station, x *****/

\$NACA65010 [1,1] = 0
 \$NACA65010 [1,2] = 0.005
 \$NACA65010 [1,3] = 0.0075
 \$NACA65010 [1,4] = 0.0125
 \$NACA65010 [1,5] = 0.025
 \$NACA65010 [1,6] = 0.05
 \$NACA65010 [1,7] = 0.075
 \$NACA65010 [1,8] = 0.10
 \$NACA65010 [1,9] = 0.15
 \$NACA65010 [1,10] = 0.20
 \$NACA65010 [1,11] = 0.25
 \$NACA65010 [1,12] = 0.30
 \$NACA65010 [1,13] = 0.35
 \$NACA65010 [1,14] = 0.40
 \$NACA65010 [1,15] = 0.45
 \$NACA65010 [1,16] = 0.50
 \$NACA65010 [1,17] = 0.55
 \$NACA65010 [1,18] = 0.60
 \$NACA65010 [1,19] = 0.65
 \$NACA65010 [1,20] = 0.70
 \$NACA65010 [1,21] = 0.75
 \$NACA65010 [1,22] = 0.80
 \$NACA65010 [1,23] = 0.85
 \$NACA65010 [1,24] = 0.90
 \$NACA65010 [1,25] = 0.95
 \$NACA65010 [1,26] = 1

/*****Thickness distribution ordinates, y_i *****/

\$NACA65010 [2,1] = 0
 \$NACA65010 [2,2] = 0.00772
 \$NACA65010 [2,3] = 0.00932
 \$NACA65010 [2,4] = 0.01169
 \$NACA65010 [2,5] = 0.01574
 \$NACA65010 [2,6] = 0.02177
 \$NACA65010 [2,7] = 0.02647
 \$NACA65010 [2,8] = 0.03040
 \$NACA65010 [2,9] = 0.03666
 \$NACA65010 [2,10] = 0.04143
 \$NACA65010 [2,11] = 0.04503
 \$NACA65010 [2,12] = 0.04760
 \$NACA65010 [2,13] = 0.04924
 \$NACA65010 [2,14] = 0.04996
 \$NACA65010 [2,15] = 0.04963
 \$NACA65010 [2,16] = 0.04812
 \$NACA65010 [2,17] = 0.04530
 \$NACA65010 [2,18] = 0.04146
 \$NACA65010 [2,19] = 0.03682
 \$NACA65010 [2,20] = 0.03156
 \$NACA65010 [2,21] = 0.02584
 \$NACA65010 [2,22] = 0.01987
 \$NACA65010 [2,23] = 0.01385
 \$NACA65010 [2,24] = 0.00810
 \$NACA65010 [2,25] = 0.00306
 \$NACA65010 [2,26] = 0

meanline_a1.jou

/Journal File for GAMBIT 2.1.2

/***** PROFILE GEOMETRY (Ref [1]) *****/

/***** Mean Line Coordinates a=1 *****/

declare \$meanline_a1 [1:3,1:26]

/***** Station, x *****/

\$NACA65010 [1,1] = 0
 \$NACA65010 [1,2] = 0.005
 \$NACA65010 [1,3] = 0.0075
 \$NACA65010 [1,4] = 0.0125
 \$NACA65010 [1,5] = 0.025
 \$NACA65010 [1,6] = 0.05
 \$NACA65010 [1,7] = 0.075
 \$NACA65010 [1,8] = 0.10
 \$NACA65010 [1,9] = 0.15
 \$NACA65010 [1,10] = 0.20
 \$NACA65010 [1,11] = 0.25
 \$NACA65010 [1,12] = 0.30
 \$NACA65010 [1,13] = 0.35
 \$NACA65010 [1,14] = 0.40
 \$NACA65010 [1,15] = 0.45
 \$NACA65010 [1,16] = 0.50
 \$NACA65010 [1,17] = 0.55
 \$NACA65010 [1,18] = 0.60
 \$NACA65010 [1,19] = 0.65
 \$NACA65010 [1,20] = 0.70
 \$NACA65010 [1,21] = 0.75
 \$NACA65010 [1,22] = 0.80
 \$NACA65010 [1,23] = 0.85
 \$NACA65010 [1,24] = 0.90
 \$NACA65010 [1,25] = 0.95
 \$NACA65010 [1,26] = 1

/***** Mean line ordinates, y_c *****/

\$meanline_a1 [2,1] = 0
 \$meanline_a1 [2,2] = 0.00250
 \$meanline_a1 [2,3] = 0.00350
 \$meanline_a1 [2,4] = 0.00535
 \$meanline_a1 [2,5] = 0.00930
 \$meanline_a1 [2,6] = 0.01580
 \$meanline_a1 [2,7] = 0.0212
 \$meanline_a1 [2,8] = 0.02585
 \$meanline_a1 [2,9] = 0.03365
 \$meanline_a1 [2,10] = 0.03980
 \$meanline_a1 [2,11] = 0.04475
 \$meanline_a1 [2,12] = 0.04860
 \$meanline_a1 [2,13] = 0.0515
 \$meanline_a1 [2,14] = 0.05355
 \$meanline_a1 [2,15] = 0.05475
 \$meanline_a1 [2,16] = 0.05515
 \$meanline_a1 [2,17] = 0.05475
 \$meanline_a1 [2,18] = 0.05355
 \$meanline_a1 [2,19] = 0.05150
 \$meanline_a1 [2,20] = 0.04860
 \$meanline_a1 [2,21] = 0.04475
 \$meanline_a1 [2,22] = 0.03980
 \$meanline_a1 [2,23] = 0.03365
 \$meanline_a1 [2,24] = 0.02585
 \$meanline_a1 [2,25] = 0.01580
 \$meanline_a1 [2,26] = 0

/******Mean line slope, dy_c/dx *****

```
$meanline_a1 [3,1] = 0
$meanline_a1 [3,2] = 0.4212
$meanline_a1 [3,3] = 0.38875
$meanline_a1 [3,4] = 0.34770
$meanline_a1 [3,5] = 0.29155
$meanline_a1 [3,6] = 0.2343
$meanline_a1 [3,7] = 0.19995
$meanline_a1 [3,8] = 0.17485
$meanline_a1 [3,9] = 0.13805
$meanline_a1 [3,10] = 0.11030
$meanline_a1 [3,11] = 0.08745
$meanline_a1 [3,12] = 0.06745
$meanline_a1 [3,13] = 0.04925
$meanline_a1 [3,14] = 0.03225
$meanline_a1 [3,15] = 0.01595
$meanline_a1 [3,16] = 0
$meanline_a1 [3,17] = -0.01595
$meanline_a1 [3,18] = -0.03225
$meanline_a1 [3,19] = -0.04925
$meanline_a1 [3,20] = -0.06745
$meanline_a1 [3,21] = -0.08745
$meanline_a1 [3,22] = -0.11030
$meanline_a1 [3,23] = -0.13805
$meanline_a1 [3,24] = -0.17485
$meanline_a1 [3,25] = -0.23430
$meanline_a1 [3,26] = 0
```


Bibliography

- [1] Abbot, I.H., Von Doenhoff, A.E., Theory of Wing Sections, 1959, Dover Publications, New York.
- [2] Bammert, K., Staude, R., Experimentelle Untersuchungen an ebenen verzögernden Tandemgittern, 1976, VDI-Berichte Nr. 264, Pg. 81 – 89, Hannover.
- [3] Bruun, H. H., Hot-wire Anemometry, 1995, Oxford University Press. United States of America.
- [4] Cumpsty, N. A., Compressor Aerodynamics, 1989, Longman Group, New York.
- [5] FLUENT, FLUENT 6 User's Manual, 1998, Fluent Inc.
- [6] GAMBIT User's Manual.
- [7] Emery, J.C., Herrig, L. J., Erwin, J. R., Felix, A.R., Systematic Two-Dimensional Cascade Test of NACA 65-Series Compressor Blades at Low Speeds, 1958, NACA Report 1368.
- [8] Horlock, J. H., Axial Flow Compressor, 1973, Kreiger Publishing Co., Melbourne, FL.
- [9] Hughes, W., Gaylord, W., Basic Equations of Engineering Science, 1964, Schaum's Outline Series, McGraw-Hill, New York.
- [10] Ihlenfeld, H., Strömungsvorgänge an geraden, stark verzögernden Spaltflügelgittern, 1965, Maschinenbautechnik 14 Heft 7, Pag 361- 365.
- [11] Lakshminarayana, B., Fluid Dynamics and Heat Transfer, 1996, Wiley-Interscience, United States of America.
- [12] Lieblein, S., Diffussion Factor for Estimating Losses and Limiting Blade Loadings in Axial Flow Compressor Blade Elements, 1953, NACA Research Memorandum RM E53D01.
- [13] Lieblein, S., Loss and Stall Analysis of Compressor Cascades, 1959, Journal of Basic Engineering, Pag. 387 –400.
- [14] Patankar, S.V., Numerical Heat Transfer and Fluid Flow, 1980, Hemisphere Publishing Corporation.
- [15] Roberts, D., Kacker, C., Numerical Investigation of Tandem-Impeller Designs for a Gas Turbine Compressor, 2002, Journal of Turbomachinery, Pag. 124.

- [16] Sachmann, J., Fottner, L., Highly Loaded Tandem Compressor Cascade with Variable Camber and Stagger, 1993, ASME paper number 93-GT-235.
- [17] Saha, A. K., Roy, B., Experimental Analysis of Controlled Diffusion Compressor Cascades with Single and Tandem Airfoils, 1995, ASME paper number 95-CTP-41.
- [18] Saha, A. K., Roy, B., Experimental Investigations on Tandem Compressor Cascade Performance at Low Speeds, 1997, Experimental Thermal and Fluid Science, Vol 14. pag. 263-276.
- [19] Sheets, E., Multiple Row Blades for Blowers, 1988, ASME paper number 88-GT-124.
- [20] Skoda, R., Numerische Simulation abgelöster und transistionaler Strömungen in Turbomaschinen, 2003, Technische Universität München, Germany
- [21] Tisch, G. Numerische Simulation in einen Tandemgitter, 1998, Internal Report, Vienna University of Technology, Austria.
- [22] Trenker, M., Berechnung der ebenen turbulenten Strömung in einem NACA 65 Verdichtergitter, 1997, Diploma thesis, Vienna University of Technology, Austria.
- [23] Turanskyi, L., Voss, H., Über die Entwicklungsarbeiten an Tandemgitterstufen für Industrie-Axialkompressoren, Thermische Strömungsmaschinen '85, 1985, Pag. 403 – 420, Bochum Germany.
- [24] Weber, A., Steinert, W., Design, Optimization, and Analysis of a High-Turning Transonic Tandem Compressor Cascade, 1997, ASME paper number 97-GT-412.
- [25] Wennerstrom, A. J., Highly Loaded Axial Flow Compressors: History and Current Developments, ASME J. of Turbomachinery 112, 1990, Vol. 112. Pag 567 – 578.
- [26] Wennerstrom, A. J., Low Aspect Ratio Axial Flow Compressors: Why and What It Means. ASME Journal of Turbomachinery 111, 1989, Pag 357 – 365.
- [27] Werdecker, F., Strömungswechselwirkung in einem Tandemgitter mit schwingender Vorleitschaufel, 2000, Technische Universität München, Germany.
- [28] Wilcox, D., Turbulence Modelling for CFD. 1993, DCW Industries, United States of America.
- [29] Willinger, R., Class Notes: Rechnergestützte Auslegung Thermischer Turbomaschinen und Thermischer Energienlagen, 2003, Vienna University of Technology, Austria.
- [30] Willinger, R., Haselbacher, H., Deviation and Profile Losses in a Turbine Cascade at Off-Design Incidences, Conference SYMKOM'99, October 1999, Poland.
- [31] Yang, C., Numerische Simulation der Strömungswechselwirkung in einem Tandemgitter mit schwingender Vorleitschaufel, 2001, Technische Universität München, Germany.

List of Figures

Figure 2-1: Tandem cascade nomenclature.....	3
Figure 2-2: Gap-nozzle area in a tandem blade.....	4
Figure 2-3: Tandem Blade. No gap nozzle area between the profiles	5
Figure 2-4: Pressure coefficient. Tandem cascade B tested by Bammert and Staude [2].....	7
Figure 2-5: Turning angle and total losses of cascade B.....	8
Figure 2-6: Turning angle and total losses relative to an equivalent single blade [2].....	8
Figure 2-7: Heavy-duty gas turbine with tandem compressor blades in the last stator row	9
Figure 2-8: Three-dimensional representation of tandem-impeller [15].....	10
Figure 3-1: Mellor diagram: NACA 651210 cascade with $\sigma=1.0$ [4]	12
Figure 3-2: Design angles of attack for NACA 65 series [8]	13
Figure 5-1. Control volume. (1) Two-dimensional grid. (2) Three-dimensional Grid	19
Figure 5-2: Subdivisions of the near-wall region [29]	26
Figure 5-3: Comparison between y^+ and y^*	29
Figure 5-4: Overview of the solution method	30
Figure 5-5: Residual plot. Convergence at the level of machine accuracy	32
Figure 6-1: Mellor diagram. NACA651510, $\sigma = 1$ [8].....	34
Figure 6-2: Finite – volume mesh. NACA651510	35
Figure 6-3: Mesh detail. NACA651510	35
Figure 6-4: y^* values NACA651510 simulation.....	36
Figure 6-5: Enlargement of the final mesh.....	36
Figure 6-6: Blade pressure distribution at design incidence	37
Figure 6-7: Profile pressure distribution at off design incidences	37
Figure 6-8: Total pressure loss coefficient	38
Figure 6-9: Pitchwise mass averaged flow angle versus inlet flow angle.....	38
Figure 6-10: Pitchwise mass averaged loss coefficient versus inlet flow angle	39
Figure 7-1: Finite – Volume mesh. Front blade NACA651210.....	42
Figure 7-2: Finite – Volume mesh. Rear blade NACA652110.....	43
Figure 7-3: y^* values. Initial tandem configuration	43
Figure 7-4: Pressure coefficient. Front blade of the tandem arrangement	44
Figure 7-5: Pressure coefficient. Rear blade of the tandem arrangement	45
Figure 7-6: Gap nozzle area discretization.....	47
Figure 7-7: Tandem mesh. Tandem blade with $a= -0.025$ and $t=-0.2$	48
Figure 7-8: First profile LE and second profile TE mesh detail.	49
Figure 7-9: Grid detail for a tandem blade with $a=-0.025$ and $t=-0.2$	49
Figure 7-10: Velocity field front blade. Tandem blade no gap nozzle effects.....	50
Figure 7-11: Pressure Coefficient tandem blade $a=0.2$, $t=-0.1$	51
Figure 7-12: Pressure Coefficient tandem blade $a=0.2$, $t=0$	51
Figure 7-13: Pressure Coefficient tandem blade $a=0.2$, $t=0.2$	52
Figure 7-14: Velocity contours. Tandem blade with $a=0.2$ and $t=0$	52
Figure 7-15: Velocity contours. Rear profile tandem blade with $a=0.2$ and $t=0.2$	53
Figure 7-16: Velocity Vectors. Rear profile tandem blade with $a=0.2$ and $t=0.2$	53
Figure 7-17: Mass average loss coefficient. Tandem blades (no gap nozzle effect)	54

Figure 7-18: Mass weighted deflection angle. Tandem blade (no gap nozzle effects)	55
Figure 7-19: Second blade axial displacements. Gap nozzle effects	56
Figure 7-20: Gap nozzle parameters. Tandem blade with $F1/F2=1.5$ and $a=-0.025$	57
Figure 7-21: Gap channel influence limit. Tandem blade with $F1/F2=1.5$ and $a=-0.025$	57
Figure 7-22: Pressure coefficient. Tandem blades $a=0$	59
Figure 7-23: Pressure coefficient. Tandem blades $a=-0.025$	60
Figure 7-24: Pressure coefficient. Tandem blades $a=-0.05$	61
Figure 7-25: Pressure coefficient. Tandem blades $a=-0.075$	62
Figure 7-26: Pressure coefficient front profile. Tandem blade $a=-0.025$	63
Figure 7-27: Convergent-divergent gap. Tandem blade $a=-0.075$, $F1/F2=1.5$	64
Figure 7-28: Path flow lines. Tandem blade with $a=-0.05$ and $F1/F2=1.5$	64
Figure 7-29: Path flow lines. Tandem blade with $a=-0.05$ and $F1/F2=3$	65
Figure 7-30: Pressure coefficient rear profile. Tandem blade $a=-0.025$	65
Figure 7-31: Contours of velocity magnitude. Tandem blade $a=-0.025$, $F1/F2=3$	66
Figure 7-32: Mass average loss coefficient vs. $F1/F2$ ratio	67
Figure 7-33: Mass average loss coefficient vs. tangential displacement	67
Figure 7-34: Contours of loss coefficient. Tandem blade with $a=-0.025$ and $F1/F2=1.5$	68
Figure 7-35: Contours of loss coefficient. Tandem blade with $a=-0.025$ and $F1/F2=2$	68
Figure 7-36: Mass average loss coefficient vs. tangential displacement	69
Figure A1-1: Blade geometry generation [1].	74
Figure A1-2: Final geometry of a NACA651510 profile	75
Figure A3 -1: Relative Position of the blades	79
Figure A3 -2: Model A: Rear blade relative far behind the front blade.	80
Figure A3 -3: model implemented when the angle ξ is lower than 45°	80
Figure A3 -4: Control Angles of the interference face	81
Figure A3 -5: Interval and Grading Pattern	81

List of Tables

Table 2-1: Location of the three tandem cascades tested by Bammert and Staude [2].....	6
Table 2-2: Characteristics of the three tandem cascades tested by Bammert and Staude [2]	7
Table 4-1: Closure coefficients of the standard $k-\varepsilon$ model	18
Table 5-1: Under relaxation factors used in the present work	24
Table 5-2: Normalization parameters.....	29
Table 5-3: Numerical Method Specifications	31
Table 6-1: Geometrical parameters NACA651510.....	33
Table 7-1: Tandem cascade blade geometry	42
Table 7-2: Numerical results. Front tandem blade	44
Table 7-3: Numerical results. Rear tandem blade	45
Table 7-4: Numerical results. Tandem blade $a = \infty$	46
Table 7-5: No gap nozzle effect. Representative tandem blades	50
Table 7-6: Final blade parameters. Gap nozzle effect tandem blades.....	58
Table A1-1: Thickness distribution for a NACA650010 and mean line data [1].	73
Table A1-2: Final data points for a NACA651510	75
Table A3 -1: Geometrical and Flow Parameters for a Tandem Blade	79
Table A3 -2: Interval and Grading Variables.....	82
Table A3 -3: Files Description	82